The Pennsylvania State University

The Graduate School

EXPERIMENTAL AND NUMERICAL ANALYSIS OF ELECTROPHORETIC CONTROL OF NANOWIRES

A Dissertation in

Mechanical Engineering

by

Scott M Davison

Submitted in Partial Fulfillment

of the Requirements

for the Degree of

Doctor of Philosophy

May 2010

The dissertation of Scott M Davison was reviewed and approved* by the following:

Kendra V. Sharp
Associate Professor of Mechanical Engineering
Dissertation Advisor, Chair of Committee

James Brasseur
Professor of Mechanical Engineering, Bioengineering, and Mathematics

M. Amanul Haque
Associate Professor of Mechanical Engineering

Theresa Mayer
Professor of Electrical Engineering

Darrell Velegol
Professor of Chemical Engineering

Karen A. Thole
Professor of Mechanical Engineering
Head of Mechanical Engineering

*Signatures are on file in the Graduate School.

Abstract

The work in this dissertation seeks to understand the electrokinetic motion of non-spherical particles, such as nanowires, in microfluidic channels. The goals are to understand how non-spherical particles move in the channels and to determine if means exist for control of the motion, position, or orientation of the particles. The results could aid in the use of nanowires, or other non-spherical particles, in areas such as electronic device manufacturing or analysis of biological particles.

Analysis of nanowire motion under electrokinetic forces was carried out using both experimental and numerical methods. From our initial experiments we determined the average velocities of populations of nanowires. The measured velocities were used to validate theoretical predictions of electrokinetic motion. Numerical studies were used to study the motion of individual nanowires, focusing on interactions with the channel walls. When the channel diameter was decreased uniformly around the particle, the velocity of the particle decreased. However, when the particle was close to one wall, the velocity of the particle increased due to an increase in electrical field between the particle and the wall. Nonsteady numerical studies and subsequent experiments demonstrated that an interaction with the channel walls caused the nanowires to oscillate in angle and position in the channel as they moved through the channel.

Control over the position or orientation of the particles was explored through active and passive means. A 90° corner was shown to be a passive aid in aligning the nanowires. As the nanowires traveled around the corner, the nonuniform electrical and flow fields caused the nanowires to align along the center of the channel. The initial numerical studies were verified by subsequent experimental studies. To actively control the position or orientation of non-spherical particles, induced-charge electroosmosis (ICEO) was explored. ICEO uses an AC electric field to induce

motion around conducting features in the channels. Numerical studies showed a wide range of control possibilities, while preliminary experiments demonstrated ICEO flows were present in the channel. Further refinement of experimental ICEO flows is ongoing through the work of Shahrzad Yazdi.

This research is consistent with previous theoretical predictions of electrokinetic motion of non-spherical particles and explores passive and active methods for motion control. The geometry of the channels was shown to passively aid in alignment of the particles. ICEO is a promising method of active positioning of the particles.

Table of Contents

List of Figures

List of Tables

List of Symbols

A	cross sectional area of channel
a	characteristic dimension of the particle or channel feature
AC	alternating current electric field
ALE	arbitrary Langrangian Eulerian
av	subscript denoting average value
b	radius of the cylindrical channel in 3D model, width of channel in 2D models
C_d	capacitance of the diffuse region of the EDL
C_s	capacitance of the stern layer of the EDL
D	diffusion constant of the ions that form the EDL
DC	direct current electric field
dep	subscript denoting dielectrophoresis
$D_{Brownian}$	translational Brownian diffusion coefficient
d_{bm}	displacement of a particle due to Brownian motion
$\mathbf{E}$	electric field vector
EDL	electrical double layer
E_x	electric field component in the x direction

e	elementary charge, $e = 1.602 \text{ x } 10^{-19}$ coulombs
eo	subscript denoting electroosmosis
ep	subscript denoting electrophoresis
$\mathbf{e}_x$	unit vector in the designated direction
$\mathbf{F}$	hydrodynamic force on a particle
$\mathbf{g}$	gravity vector
g_{av}	correction factor for the electrophoretic velocity of a randomly oriented cylinder
$g_{\parallel}$	correction factor for the electrophoretic velocity of a cylinder oriented parallel to the electric field
$g(\kappa a)$	correction factor for the electrophoretic velocity of a cylinder oriented perpendicular to the electric field
h	distance from the center of the particle to the closest wall
$\mathbf{I}$	identity tensor
I	moment of inertia of the particle
ICEO	induced-charge electroosmosis
KCl	potassium chloride salt
k	Boltzmann constant, $k = 1.38 \text{ x } 10^{-23}$ m^2 kg s^{-2} K^{-1}
L	length of the channel
l	length of the particle
MESNA	abbreviation for the chemical 2-mercaptoethanesulfonate
m	mass of the particle
$\mathbf{n}$	unit normal pointed into the fluid domain
n_i	concentration of species i in a specific region
$n_{i\infty}$	concentration of species i in the bulk

ODE	ordinary differential equation
PDMS	polydimethylsiloxane
Pe	Peclet number representing the ratio of electrophoretic motion to Brownian diffusion
PSL	polystyrene latex
p	pressure
q	total electric charge of a particle or region of space
Re	Reynolds number representing the ratio of inertial forces to viscous forces
$\mathbf{T}$	hydrodynamic torque acting on the particle
T	temperature, in Kelvin
TRITC	tetramethyl rhodamine iso-thiocyanate, type of microscope filter cube for fluorescent micsroscopy
t	time
t_{eo}	estimate of the time for electroosmotic flow to reach steady state
$\mathbf{U}_p$	particle velocity vector
U	fluid velocity in a designated direction
UV	ultra-violet light
U_{eo}	velocity of the electroosomotic flow
U_{ep}	velocity of the electrophoretic motion
U_{Keh}	electrophoretic velocity of a sphere from Keh and Anderson (6)
U_{obs}	observed velocity of particles undergoing motion combining electroosmosis, electrophoresis, pressure, and Brownian motion
$U_{pressure}$	velocity resulting from pressure
U_∞	electrophoretic velocity of a particle in unbounded flow
$\mathbf{u}$	fluid velocity vector

V	volume of fluid passing through the channel
x, y, z	axes of the coordinate system
$\mathbf{X}_p$	position vector of the center of the particle
$\mathbf{x}_p$	position vector on the particle surface
Y_0	initial vertical position of the particle in the channel
z_i	charge number of species i
Γ_w, Γ_p, Γ_{in}, Γ_{out}	boundaries of the computational domain
γ	ratio of channel wall zeta potential to particle zeta potential
δ	ratio of capacitances of the EDL, $\delta = C_d$ / C_s
ε	permittivity of the fluid, $\varepsilon = \varepsilon_r\ \varepsilon_0$
ε_r	relative permittivity of the specific fluid
ε_0	permittivity of free space, $\varepsilon_0 = 8.854$ x 10^{-12} F m^{-1}
ζ	zeta potential
ζ_p	zeta potential of the particle surface
ζ_w	zeta potential of the channel wall
θ	angle of the particle with respect to the horizontal
θ_0	initial angle of the particle with respect to the horizontal
θ_f	final angle of the particle with respect to the horizontal
θ'	absolute value of the angle the particle makes with respect to the vertical direction
κ	inverse of the physical thickness of the EDL
λ_D	measurement of the physical thickness of the EDL
μ	dynamic viscosity of the fluid
ν	kinematic viscosity of the fluid

π	mathematical constant, $\pi = 3.14$
ρ	fluid density
ρ_e	charge density of ions
σ	stress tensor on the particle surface
τ	charging time of the EDLs
ϕ	electrical potential of a region of interest
ϕ_0	applied electric potential
ψ	nondimensional electric potential
ψ_s	electrical potential at the surface of a channel or particle
Ω	fluid domain outside the EDLs
ω	frequency of the applied AC electric field
ω_p	rotational velocity of the particle

Acknowledgments

I would like to express my sincerest gratitude to my advisor, Dr. Kendra Sharp. This dissertation would not have been possible without her guidance, support, and flexibility. I also gratefully acknowledge the support of my committee members: Dr. James Brasseur and Dr. M. Amanul Haque of the Mechanical and Nuclear Engineering Department, Dr. Theresa Mayer of the Electrical Engineering Department, and Dr. Darrell Velegol of the Chemical Engineering Department. The breadth of their expertise was invaluable to moving the dissertation to completion.

I would also like to thank the other members of the Microscale Flow Laboratory. Darren, Eric, Andrew, Shahrzad, and Preyank thanks for making the lab a great place to work and providing assistance of the professional and not so professional variety.

I acknowledge the support of the Penn State Nanofabrication Laboratory and the research group of Dr. Christine Dolan Keating for their assistance in development of particles and devices for the experiments.

Material in this dissertation is based upon work supported by the National Science Foundation under Grant No. 0348149. I gratefully acknowledge the financial support provided.

I would like to give thanks to my parents and my brother for their support in this journey. Finally and most importantly I would like to profusely thank my wonderful wife, Megan. Without her love, support, and encouragement I would not have been able to get through the dissertation process. Thank you for putting up with me during these difficult times, I love you!

Frontispiece

A sense of accomplishment?

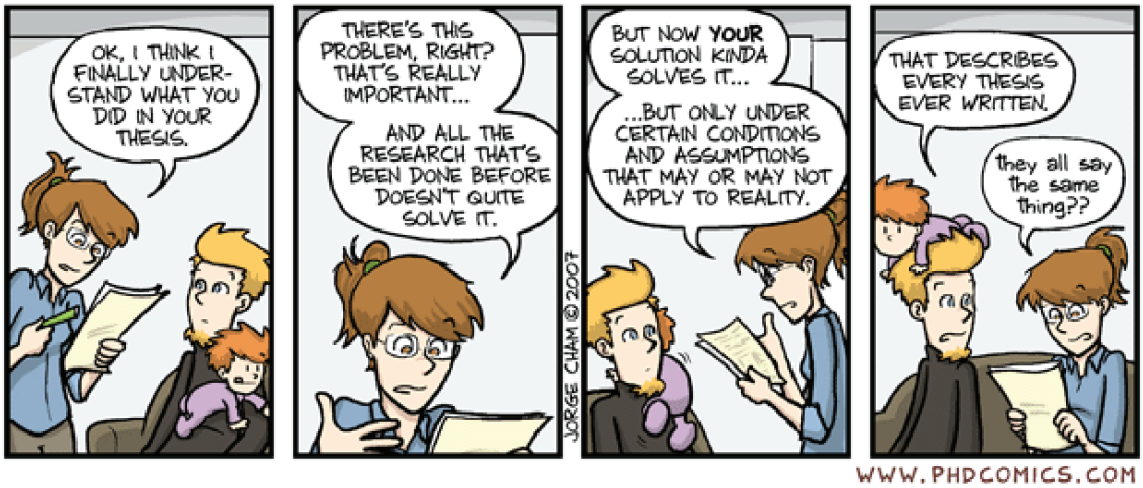

"Piled Higher and Deeper" by Jorge Cham
www.phdcomics.com

Chapter 1

Introduction

Nanotechnology is a promising field of science that deals with developing new materials or devices on a small scale, generally on the order of 100 nm or less. The area of nanotechnology, as related to this dissertation, is in the development of new nanoscale devices. Traditional manufacturing of small devices, such as electronic chips, has started with a large object to which material is added or removed for the creation of transistors or other features. This concept is often referred to as a top down approach to manufacturing. A bottom up approach would involve building a device from a collection of small components and should enable the construction of devices on a scale smaller than is possible with traditional manufacturing. The research in this dissertation examines the use of electrokinetically driven fluid flows in microchannels as one possible means of manipulating the position, orientation, and movement of mico- and nano-particles, as a step in the process of building objects in a bottom up fashion.

Electrokinetics is the motion of fluid and particles under the action of an electric field. The electrokinetic phenomena of interest in this dissertation are electroosmo-

sis and electrophoresis, both initiated by an applied DC or AC electric field. The electrically-driven movement of fluid is electroosmosis, and electrophoresis is the corresponding motion of suspended charged particles. A more detailed description of these electrokinetic phenomena follows in Chapter 2.

The motion of the particles in the microfluidic channels is of primary focus in this investigation, therefore much of the focus is on their electrophoretic motion. Electrophoresis is a frequently used electrokinetic phenomenon, with important applications in colloidal, biological, and electronic / sensing sciences. It can be used to separate colloidal particles and to propel particles through microfluidic channels. Extensive study of the motion of spherical particles in unbounded electrophoresis exists, and mathematical models can be found in classical texts such as Hunter (8). However, the focus of this dissertation is on the electrophoresis of particles with non-spherical shapes, primarily cylindrical particles, such as nanowires.

Nanowires with, nanometer-scale diameters and lengths of several microns up to tens of microns, have recently garnered significant attention given their potential applications within the fields of electronics (9; 10), sensing (11; 12), and photonics (13; 14; 15). Nanowires can be fabricated from a diverse set of materials, including metals and semiconductors, and functionalized or tailored for a range of applications (e.g. detection of specific biological or chemical species (16; 17)). Typically, for such particles to be useful in a micro or nanoscale system, their orientation and position must be precisely controlled. In some cases, it is possible to manufacture the wires arranged in a desired pattern (18), however, such a method is not possible in many cases due to limited materials selection in the manufacturing process.

A microfluidic system based on standard electrophoresis is examined as a means of exerting control on non-spherical particles. An additional aspect of studying non-spherical particles is that they are a reasonable analogue to many biological particles. There are few spherical cells or organisms in nature, therefore, studying the motion of nanowires could contribute to the development of biological or medical detection or treatment devices where isolating or positioning specific cells is of importance.

1.1 Objectives of the Study

In order to explore the motion of non-spherical particles in a microfluidic channel, a series of objectives was proposed to analyze the movement of particles and develop a means to predict and control their motions. The first objective was to experimentally quantify the bulk electrophoretic motion of non-spherical particles through experimental observations. These observations were compared to theoretical predictions to determine their validity. Additionally, various physical properties in the experiment were altered to determine their effect on the velocity of the particles; the surface charge of the particles being the primary property of interest.

The second objective was to quantify the influence of the channel boundaries on the motion of the particles, since miniaturization of the system makes the particles and channels nearly the same size scale. The channel boundary was expected to affect the velocity and orientation of non-spherical particles. Two types of boundary conditions were explored. The first bounadry condition occurred when the particle was equally affected by the boundaries on all sides (concentrically

located), the case where the channel size was reduced to nearly the size of the particle. The second boundary condition was the situation where the particle interacts preferentially with one boundary (eccentrically located), generally the case when the suspended particle was of a different density than the suspending medium.

The final objective was to explore means to exert control over the motion, orientation, or positioning of the non-spherical particles. The means of control explored were both passive, elements of channel geometry, and active, additional electric or fluid flow fields.

1.2 Outline of Dissertation

In order to accomplish the objectives of this study both experiments and numerical simulation were utilized. The chapters of this dissertation are laid out in research order, as previous findings provided direction for each successive investigation. Chapter 2 contains a brief overview of the theory of electrokinetics along with the applicable literature review. Similarly, the following chapters contain a literature review appropriate to the subject matter.

An initial set of gold nanowire electrophoresis experiments were conducted. The bulk average velocity measurements of the wires from all locations across the channel and over a range of orientations were compared to theoretical predictions. Additionally, the experiments examined the effect of altering the surface charge on the nanowires. The velocities of the nanowires in a microfluidic channel exhibited a dependence on surface charge, demonstrating a method for control or separation of wires with varying surface properties. The details of the experiments and the

results are given in Chapter 3.

The initial experiments demonstrated that conditions did exist for the electrophoretic motion to deviate from predicted bulk theory. Numerical simulations of the system provided a means to examine specific cases of boundary interaction in more detail than was available in the initial experiments. Chapter 4 describes the initial numerical simulations of the forces and torques acting on the nanowires in the two boundary conditions of interest; the particle located concentrically or eccentrically in the channel. It was found that the two types of boundary conditions each affected the motion of the particle in a way that deviated from bulk, unbounded motion, but that there were differences in the effects of the two boundary conditions. These numerical simulations focused on steady-state results and identifying situations where the particles would not translate in a steady state manner under electrophoresis.

The identification of boundary conditions that led to nonsteady particle motion necessitated the development of the nonsteady numerical models described in Chapter 5. The nonsteady models demonstrated the nanowires will rotate due to asymmetries created by the boundaries, as well as translate in the direction perpendicular to the electrophoretic motion. Extended nonsteady models were used to investigate the development of a steady motion over a long period of time. The extended models demonstrated that within a channel longer than would be practical in a microfluidic device the motion in either boundary case does not approach steady state. This result removes the possibility of using extended microfluidic channels for reducing the uncertainty of the nanowire positioning through knowledge of a known steady-state motion.

The development of working nonsteady models enabled the study of the motion of nanowires through a variety of channel geometries. A 90° corner geometry provided a positive orientation affect on the motion of nanowires through the corner. Numerical testing of a wide variety of nanowire trajectories through the corner region demonstrated a reduction in the variability of the angle of the nanowires. The model setup and results of the study illustrating a passive method for reducing uncertainty in the nanowire orientation are located in Chapter 6.

Extensive investigation into the details of the boundary interactions with the nanowires raised the question of where the nanowires are located in relation to the boundaries in the experimental conditions. Metallic nanowires used for the preliminary experiments in Chapter 3 are of greater density than the aqueous fluid in which they are suspended. It is readily observed that the nanowires sink toward the bottom wall of the channel, but the electrophoretic motion of the nanowires demonstrates that they are suspended some distance above the surface of the channel wall. The nanowires are separated from the channel wall by a certain distance due to electrostatic repulsion arising from the negative surface charges on both the wall and particle. A series of confocal microscopy images were taken of a nanowire adhered to the channel surface and one freely suspended above it. A statistical analysis of a series of measurements between the wires established the separation of a nanowire from the channel surface under the desired experimental conditions. The details of the measurements and the analysis are included in Chapter 7.

In Chapter 8 we describe a revised set of experimental observations meant to improve upon the preliminary experiments, and we examine the numerical pre-

dictions. The method of manufacturing the microchannel was revised to allow creation of smaller channels for boundary studies and various channel geometries to explore the effect of a 90° corner. Additional changes helped reduce the previous uncertainties in the electric field strength and surface properties of the channel and nanowires. The improved experimental setup enabled a more exacting study of the relation to electrophoretic theory, as well as, a more detailed comparison to results of the numerical studies.

An active means of nanowire manipulation is explored in Chapter 9. Induced-Charge Electroosmosis (ICEO) is an electrokinetic phenomenon that produces fluid flow fields around conducting objects in the presence of an AC electric field. The applied AC field has little effect on the electrophoretic motion of the particles, but through strategic placement of the conducting objects in the channel the additional fluid flow field can positively impact the trajectory of the nanowires. The potential applications of ICEO flow are explored in numerical simulations and preliminarily demonstrated in experiments. The dissertation concludes with a summary and discussion in Chapter 10.

Chapter 2

Electrokinetic Preliminaries

Under the conditions of interest in the present work, the motion of the particles, as well as, the suspending fluid is governed by the principles of electrokinetics. The motion arises due to the movement of ions in the fluid when an electric field is applied. A key feature of electrokinetic motion is that it is boundary driven by the ion motion in the electric double layer (EDL) that forms at the surface of channel walls or particles. An overview of the formation and structure of EDLs is presented below followed by basic descriptions of electroosmosis, the motion of the fluid, and electrophoresis, the motion of the particles. This chapter concludes with a brief discussion of how these various motions combine in a realistic system.

2.1 Electrical Double Layer

The origin of the electrical double layer lies in the surface charge present in the channel walls, or the particle surface, when exposed to an aqueous solution. The surface charges can develop from dissociation of surface groups or ion adsorption and are inherent in the surface; the surface charges are immobile. The EDL arises

when the surface charges repel ions of like charge and attract ions of opposite charge from the bulk solution. This region, near the surface and with an excess of counterions, is the EDL. A schematic of the structure of the EDL and the distribution of potential within it are included in Fig. 2.1.

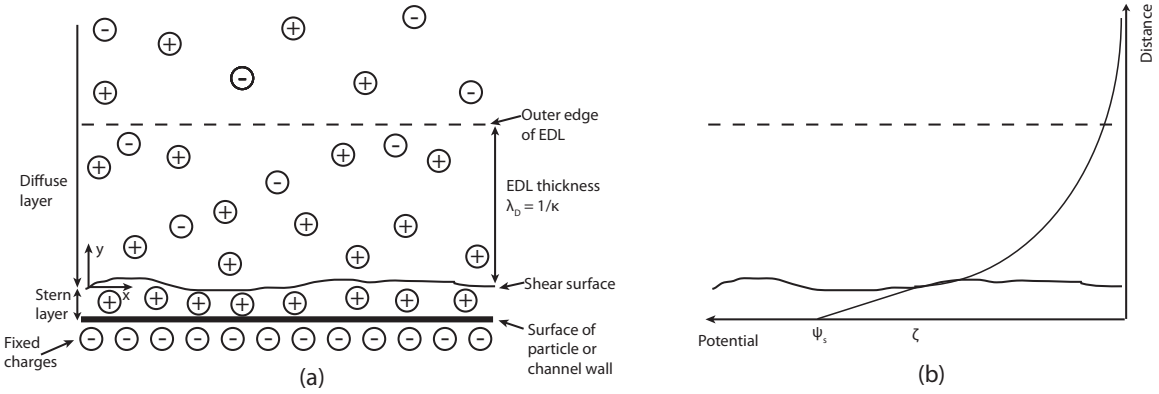

Figure 2.1: Schematic diagram of the structure and potential distribution of the electrical double layer (EDL) at the surface of a particle or channel wall. (a) Distribution of the ions that form the EDL. Specific regions of interest are labeled. (b) Distribution of the potential within the EDL. Locations of important potentials indicated, potential at the surface, ψ_s, and zeta potential, ζ. Diagrams adapted from Probstein (1) and Shaw (2).

The finite size of the attracted ions limits their distribution near the surface. The ions can only approach the surface to a minimum distance equal to their hydrated radius. The layer of ions attracted nearest to the surface is termed the Stern layer. Due to their close proximity to the surface charges, the ions within the Stern layer are held largely immobile. The ions outside the Stern Layer, termed the diffuse layer, are attracted less strongly and can become mobile when an electric field is present. The movement of ions within the diffuse layer gives rise to electroosmosis and electrophoresis. The shear surface is the plane where the mobile ions in the diffuse layer are moving past the charged surface and ions fixed

within the Stern layer. The surface potential that is not shielded by the ions in the Stern layer is the potential at the shear surface and is termed the zeta potential, ζ (8). The zeta potential is an important electrokinetic parameter as it determines the relative strength of the mobile diffuse layer; thereby, influencing the velocity of electrokinetic phenomenon. The outer edge of the EDL is designated as the point where the potential that results from the surface charges is reduced by attracted ions to equal the random thermal energy of the ions. The thickness of the EDL is indicated in Fig. 2.1b on the diagram of the distribution of potential in the EDL.

To estimate the thickness of the EDL, it is necessary to develop an expression for the distribution of the electrical potential that arises from the surface charges. The surface charge does not vary in time so the Poisson equation of electrostatics is used to model the electric field of interest

$$\nabla^2\phi = -\frac{\rho_e}{\varepsilon}. \tag{2.1}$$

In this Poisson equation, the electric potential is ϕ, the charge density of the distributed ions is ρ_e, and ε is the permittivity of the solution. The charge density is determined by a simplified version of the Boltzmann equation, which is used in statistical mechanics to describe the distribution of a particle in a fluid (19),

$$n_i = n_{i\infty} exp(\frac{-z_i e\phi}{kT}), \tag{2.2}$$

where n_i and $n_{i\infty}$ are the concentration and bulk concentration of species i, z_i is the charge number of species i, e is the elementary charge, k is the Boltzmann constant, and T is the temperature. The Boltzmann equation is used to determine

the charge density needed in the Poisson equation.

$$\rho_e = \sum_{i=1}^{M} n_i e z_i. \tag{2.3}$$

With the assumption that the suspending solution contains a symmetric electrolyte, which means M=2 and $|z_1| = |z_2| = Z$, the combined Poisson-Boltzmann equation can be simplified to

$$\nabla^2 \psi = \kappa^2 \sinh \psi, \tag{2.4}$$

where $\psi = \frac{Ze\phi}{kT}$ is a nondimensional electric potential and $\kappa^2 = \frac{2n_\infty Z^2 e^2}{\varepsilon kT}$. The thickness of the EDL is termed the Debye length (1) and given by

$$\lambda_D = \frac{1}{\kappa} = (\frac{\varepsilon kT}{2n_\infty Z^2 e^2})^{1/2}. \tag{2.5}$$

In practice, the Debye length is usually small compared to the channel size. For a 100 mM electrolyte solution, the Debye length is 1 nm. Over the range of experimental conditions included herein the Debye length can be as large as 175 nm, due to the low concentration of ions in the suspending fluid.

2.2 Electroosmosis

Electroosmosis is the motion of fluid along channels with charged walls caused by the motion of ions in the diffuse layer of the EDL at the channel surfaces. If the surface charge of the channel walls is negative, the diffuse layer will be populated with an excess of positive ions. A uniform electric field applied along the axis of

the channel will cause the positive ions in the EDL to move toward the negative electrode. Through viscous drag, the motion along the boundaries drives fluid flow across the entire channel. Figure 2.2 is a schematic of electroosmotic flow in a channel.

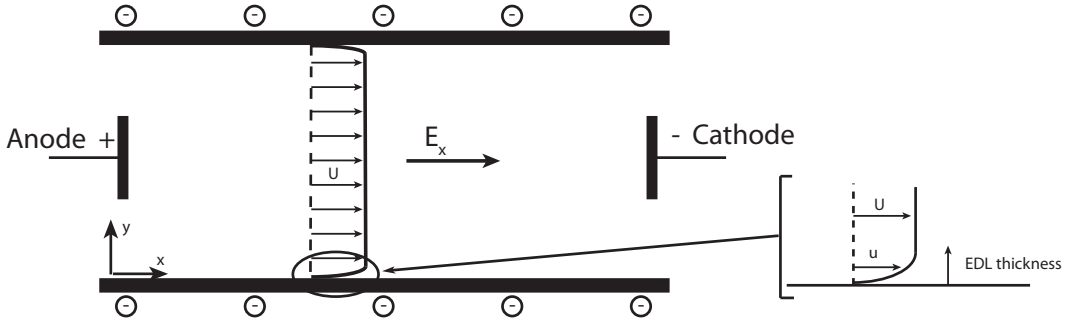

Figure 2.2: Schematic of electroosmotic flow field in a channel with uniformly negatively charged walls. A zoomed schematic of the flow field within the EDL is included.

To determine the electroosmotic velocity in a channel, the fluid momentum equations are solved within the EDL where the velocity at the outer edge of the EDL is the velocity of the flow. The momentum equation, with an electric body force term,

$$\rho\frac{D\mathbf{u}}{Dt} = \mu\nabla^2\mathbf{u} - \nabla p + \rho\mathbf{g} + \rho_e\mathbf{E} \tag{2.6}$$

is simplified by scaling to the Stokes equations

$$0 = \mu\nabla^2\mathbf{u} - \nabla p + \rho\mathbf{g} + \rho_e\mathbf{E} \tag{2.7}$$

due to the small Reynolds number (Re) of the system. The Reynolds number is a nondimensional number that gives the ratio of inertial to viscous forces in a fluid flow. The small velocities and channel sizes in electroosmotic experiments yield a typical Reynolds number of $Re \approx 10^{-5}$, which allows use of the Stokes equations

(Eqn. 2.7).

The equations are further simplified by assuming there are no gravitational body forces or pressure gradients in the channel. Pressure gradients are assumed to be zero because the channel system is open within the time scales used in the experiments. Further examination of this assumption is made in Chaps. 3 and 8. The problem then reduces to a balance of electric and viscous forces,

$$\mu\nabla^2\mathbf{u} = -\rho_e\mathbf{E}. \tag{2.8}$$

Using the coordinates in Fig. 2.2 and assuming a long channel with a uniform electric field, the velocity will not vary in the x-direction, but only in the y-direction across the width of the EDL. Similarly, if the Debye length, $1/\kappa$, is small relative to the radius of the channel, the electrical force is approximately one-dimensional. Since y, the EDL thickness variable, is a much smaller scale than x, the distance along the channel, $\frac{\partial^2\phi}{\partial^2 y} \gg \frac{\partial^2\phi}{\partial^2 x}$, so that $\nabla^2\phi \approx \frac{\partial^2\phi}{\partial^2 y}$. The simplified equation is

$$\mu\frac{\partial^2 u}{\partial^2 y} = \varepsilon\frac{\partial^2\phi}{\partial^2 y}E_x \tag{2.9}$$

where Poisson's equation was used to substitute for ρ_e. Integrating Eqn. 2.9 leaves $\mu\frac{\partial u}{\partial y} = \varepsilon\frac{\partial\phi}{\partial y}E_x$ since at the edge of the EDL the derivatives of velocity and potential go to zero. Using the boundary conditions that are known from the structure of the EDL, $\phi = \zeta$ and $u = 0$ at $y = 0$ (the shear surface) plus $u = U$ and $\phi = 0$ at $y = \infty$ (the outer edge of the EDL), and integrating the flow velocity yields

$$U_{eo} = -\frac{\varepsilon\zeta_w E_x}{\mu}. \tag{2.10}$$

Formula 2.10 is known as the Helmholtz-Smoluchowski equation (1). It gives the electroosmotic fluid velocity, U_{eo}, in a system given the permittivity, ε, and viscosity of the fluid,μ, zeta potential of the channel walls, ζ_w, and the applied electric field strength, E_x. The negative sign comes from the fact that a negative zeta potential drives a flow in the positive direction of the electric field.

The electroosmotic velocity formula gives the velocity of the plug flow once the flow reaches steady state. However, it takes time for the viscous drag to diffuse to the center of the channel from the walls. Minor et al. (20) provides an estimate of the time for the fluid momentum to diffuse to the center of the channel by using the size of the channel, $2b$, and the kinematic viscosity of the fluid, ν,

$$t_{eo} = \frac{(2b)^2}{\nu}. \tag{2.11}$$

Using physical parameters from the experimental work in this dissertation, this time estimate is on the order of milliseconds. The transient development of electroosmotic flow is disregarded in this work as it is not possible to experimentally observe the few milliseconds of transient flow present.

2.3 Electrophoresis

Electrophoresis is the motion of charged particles due to application of an electric field. For simplicity consider the case of a negatively charged sphere suspended in an electrolytic solution subject to a uniform electric field. Two extreme cases can be considered, first, the case where the EDL surrounding the particle is much bigger than the sphere's radius, a ($\kappa a \rightarrow 0$, since $1/\kappa$ = EDL thickness). As in

electroosmotic flow, the problem of finding the particle velocity reduces to a balance between the electric force and the fluid force. With a large EDL surrounding a small particle, the electrical force reduces to one acting on a point charge in an unperturbed electric field, qE_x, and the fluid exerts a frictional force that reduces to Stokes drag on a sphere, $6\pi\mu Ua$. The particle charge, q, is balanced by an opposite charge, $-q$, distributed throughout the EDL due to charge conservation. The zeta potential can be approximated as the potential that exists between two concentric spheres of charge q, at the particle surface with a radius of a, and $-q$, at the edge of the EDL at a radius of $(a + 1/\kappa)$. The expression for ζ is (1)

$$\zeta = \frac{q}{4\pi\varepsilon a} - \frac{q}{4\pi\varepsilon(a + \frac{1}{\kappa})} \tag{2.12}$$

$$\zeta = \frac{q}{4\pi\varepsilon a(1 + \kappa a)}. \tag{2.13}$$

Substituting this expression into the force balance for the motion of the sphere yields

$$6\pi\mu Ua = qE_x \tag{2.14}$$

$$6\pi\mu Ua = 4\pi\varepsilon\zeta a(1 + \kappa a)E_x \tag{2.15}$$

$$U = \frac{2}{3}\frac{\varepsilon\zeta(1 + \kappa a)}{\mu}E_x \tag{2.16}$$

This velocity expression is valid in the limit $\kappa a \to 0$ leaving

$$U_{ep} = \frac{2}{3}\frac{\varepsilon\zeta E_x}{\mu} \tag{2.17}$$

to describe the electrophoretic velocity of a small sphere with an large EDL (8). This expression is known as the Hückel equation.

The second case to be considered is when the EDL thickness is small compared to the radius of the spherical particle ($\kappa a \rightarrow \infty$). Here the EDL is thin so that the curvature of the sphere can be neglected, and the surface below the EDL is locally plane. The electric field can be considered to be parallel to the surface at all points due to this assumption. In this case, the derivation conducted for electroosmosis in a channel applies to the surface of the particle . Here, the particle motion is of interest instead of the fluid so the integration yields a particle velocity of opposite sign than in electroosmosis,(Sec. 2.2, Eqn. 2.10)

$$U_{ep} = \frac{\varepsilon \zeta E_x}{\mu}. \tag{2.18}$$

Electrophoretic velocities are thus bounded by a factor of 1 for a thin EDL and 2/3 for a thick EDL.

Physical systems of interest rarely fall into either of the theoretical limits. Additional effects need to be taken into account and they are termed electrophoretic retardation, surface conduction, and relaxation. Electrophoretic retardation arises when the ions in a finite thickness EDL are acted on by the electric field and move electroosmotically opposite to the direction of the particle (21). Surface conduction occurs because the region of the EDL near the surface contains a higher concentration of counter ions than the bulk solution. This region of higher concentration has higher conductivity and, therefore, a lower electric field, reducing the electrophoretic velocity (22; 23). As noted, the ions in a finite thickness EDL move oppositely to the particle which cause the EDL itself to distort. The EDL

is no longer symmetric about the spherical particle with a thinner region in front of the particle and a thicker region at its rear (1). Accounting for these three effects requires numerical solution, since the symmetry of the problem is broken. Solutions for the electrophoretic velocity have been computed and are useful for predicting experimental observations (24; 25).

2.4 Superposition of Effects

In addition to the electroosmotic and electrophoretic motions, the particles and fluid in the channel may be subjected to pressure-driven motion. A pressure difference between the ends of the channel serves to inhibit the motion in one direction and enhance it in the other. The governing equations for the electrokinetic and pressure flows are linear under the conditions of low Reynolds number and constant and uniform material properties, so the contributions from all of them can be superposed (26; 27):

$$U_{obs} = U_{eo} + U_{ep} + U_{\text{pressure}} + \frac{d_{bm}}{\Delta t}. \tag{2.19}$$

The total observed particle velocity, U_{obs}, is the sum of the electroosmotic, U_{eo}, electrophoretic, U_{ep}, and pressure, U_{pressure}, velocities, as well as, the displacement due to Brownian motion divided by the time separation, $\frac{d_{bm}}{\Delta t}$.

Chapter 3

Average Bulk Electrophoresis Experiments

3.1 Introduction

The current chapter seeks to address the behavior of electrokinetically-controlled nanowire movement in microfluidic channels, specifically emphasizing the effects of coatings and their associated changes in nanowire surface charge. Both functionalization and addition of a surfactant, while satisfying specific application needs and minimizing aggregation respectively, alter the nanowires' surface charge. The velocity of the nanowires in a microfluidic channel exhibits a dependence on surface charge, emphasizing the importance of establishing a fundamental understanding of the effects of particle characteristics and accompanying flow behavior in order to achieve accurate electrokinetic control of the nanowires.

3.2 Electrophoretic Theory of Non-Spherical particles

The use of cylinders alters the electrophoretic theory (Sec. 2.2, 2.3) because the motion of the cylinder depends on the orientation with respect to the electric field (1). Stigter (28) conducted an analysis of cylinder velocities and found that the equation for average electrophoretic velocity could be modified as follows:

$$U_{ep} = \frac{2}{3}\frac{\varepsilon\zeta_p}{\mu}E_x g_{av}. \tag{3.1}$$

The function g_{av}, representing the average correction factor for a randomly oriented cylinder, in Eqn. 3.1 accounts for the relaxation effect and depends on both the size of the double layer and the zeta potential of the particle. The function g_{av} also accounts for orientational dependence, i.e. that a cylinder oriented parallel to the electric field has a different electrophoretic velocity than a cylinder oriented perpendicular to the electric field.

The equation for g_{av} given by Stigter (28) is:

$$g_{av} = \frac{g_{\|} + 2g(\kappa a)}{3}. \tag{3.2}$$

The term $g_{\|}$ represents the factor for a cylinder aligned parallel to the electric field and is equal to 1.5 for all κa. The function $g(\kappa a)$ represents the correction factor for a cylinder oriented perpendicular to the electric field (28). Values of g_{av} are tabulated for various values of κa as a function of the zeta potential of the particle.

3.3 Experimental Setup

In this experiment, the motion of multiple populations of cylindrical nanowires suspended in an aqueous solution was observed. The gold nanowires used in the experiment were made by electrochemical deposition of metal into a template (29) and have diameters of 300–350 nm. The lengths of the wires can be precisely controlled by the time of the deposition. The wires used in the experiment were made to lengths of 5, 8, and 11 μm long, for aspect ratios of 16.67, 26.67, and 36.67 respectively. Each set of wires of a specified length were split into two populations with half of the wires left uncoated so they had negligible surface charge, and half of the wires coated with sodium 2-mercaptoethanesulfonate (MESNA) in a self assembled monolayer to provide a negative surface charge. All sets of wires were suspended in deionized (DI) water. Figure 3.1 shows suspensions of two different lengths of gold nanowires in the microfluidic channel.

The surface charge present on the coated and uncoated wires was determined using a ZetaPALS instrument (Brookhaven Instruments Corporation, Holtsville, NY). These measurements confirmed that the uncoated wires had a negligible zeta potential, and indicated that the coated wires had a zeta potential of ζ_p = -27 mV.

The experiments were carried out inside of square borosilicate glass channels from VitroCom (Mountain Lakes, NJ). The inside dimension of the square channel was 80 μm, and based upon the literature (30; 31), the zeta potential of the channel walls used in all further calculations is taken as $\zeta_w = -60$ mV. Sanders (30) and Gu (31) used different methods to determine the zeta potential of glass in contact with water but both lead to the estimation of $\zeta_w = -60$ mV under the current experimental conditions.

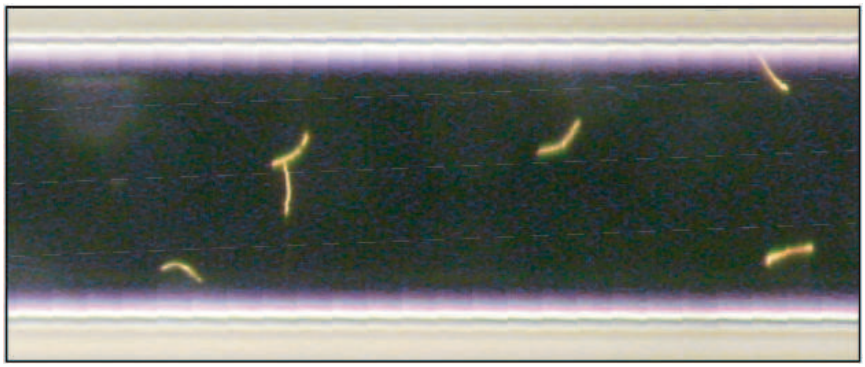

(a)

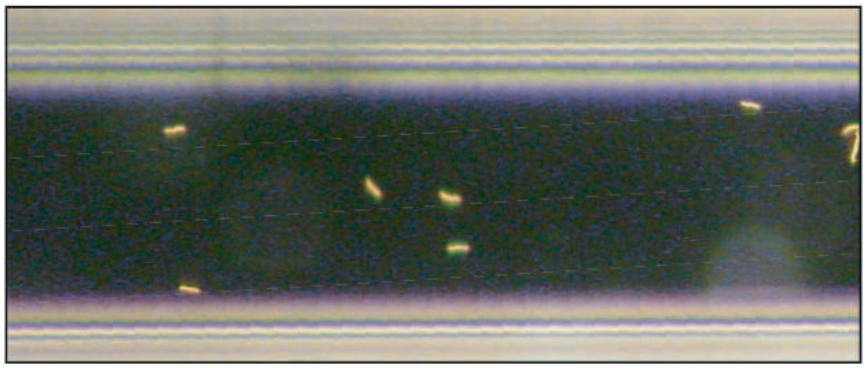

(b)

Figure 3.1: Darkfield-illuminated gold nanowires suspended in deionized water in an 80 μm glass microchannel. (a) Wire Length = 11 μm, Wire Diameter $\approx$ 300 nm (b) Wire Length = 5 μm, Wire Diameter $\approx$ 300 nm. Note: wires in (a) are showing bends due to the manufacturing process.

The velocity measurement experiment was set up using two microscope slides as a base. The two slides were placed onto the microscope stage with a small separation between them. A 0.5 mm diameter platinum wire was affixed to each slide to introduce the electrical field. A 20 μL drop of gold nanowires suspended in deionized water was placed over the platinum wire on each slide. A section of glass microchannel was then placed between the slides, and capillary forces drew

suspension from each of the drops at the ends into the channel until the drops met and fully filled the channel. The use of equal sized drops of nanowire solution helped to alleviate pressure differences between the two ends of the channel. The behavior of the gold nanowires in the channel was observed and recorded by a standard video microscopy apparatus. A function generator was used to introduce a 0.2 Hz square wave at 5.0 Vpp, thereby applying a low-frequency alternating electrical field. An alternating field was used to limit the volume of fluid that moves from one drop to the other during a test. Minimizing the fluid transfer minimizes the pressure difference that would build up if the fluid flowed only in one direction, thereby increasing the size of one drop and reducing the other. The experimental results demonstrate no identifiable return pressure flows, therefore the system is assumed to be open. In a closed system, the fluid that flows has no where to go so pressure builds that results in flow down the center of the channel in the opposite direction of the electrokinetic flow. Figure 3.2 shows a typical experimental setup.

A second experimental setup was employed for an additional test in order to address the variability in positioning of the glass slides. The two glass slides containing the platinum electrodes were not fixed with respect to one another and so the distance between electrodes could vary from test to test. A slight change in the distance between electrodes would have a large effect on the value of the applied electric field and on the velocity of the nanowires. Figure 3.3 shows the revised experimental setup. Here gold electrodes were deposited onto one glass slide so that the distance between them was fixed. As before, a drop of suspended nanowires was placed over each electrode and a section of glass microchannel connected the

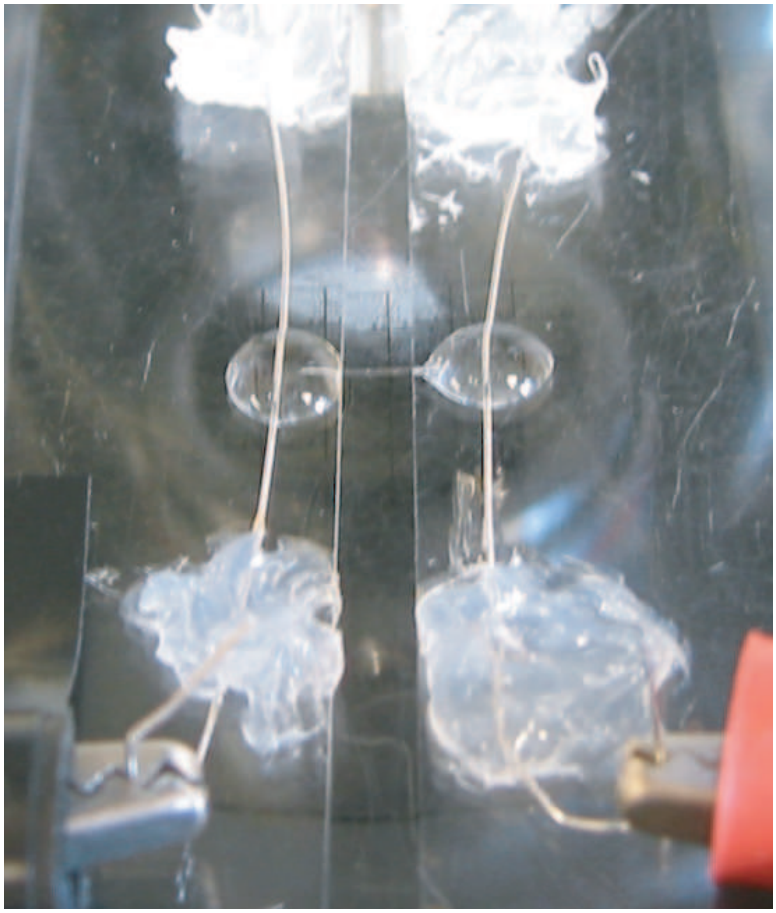

Figure 3.2: Typical initial experimental setup for the measurement of electroosmotic and electrophoretic motion of gold nanowires. Two drops of suspension are placed over the platinum wires, and the microfluidic channel (relatively difficult to discern in the photo) is placed between these drops.

drops.

Data were acquired in five separate sets of experiments on the initial setup and one additional set on the revised electrodes, where each "set" included the acquisition of digital video clips of the motion of both uncoated and coated wires under the applied electric field and any background pressure-driven flow component with the electric field off. The velocities of both coated and uncoated wires are computed by manual particle tracking in the captured images. The time be-

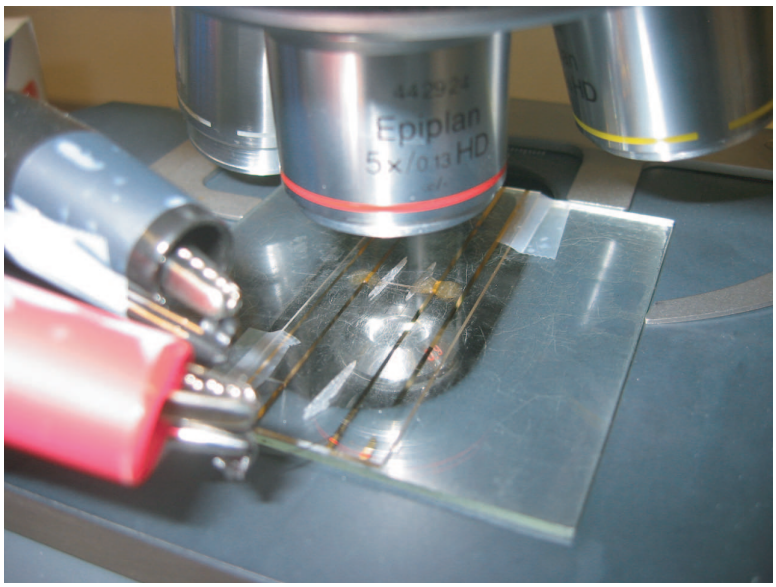

Figure 3.3: Revised experimental setup for the measurement of electroosmotic and electrophoretic motion of gold nanowires. Two drops of suspension are placed over the gold electrode, and the microfluidic channel (relatively difficult to discern in the photo) is placed between these drops.

tween frames was at least an order of magnitude greater than the time for either electroosmosis or electrophoresis to reach steady-state, ensuring that any transient velocities were not affecting the results.

The uncoated wires were used to determine the electroosmotic velocity of the fluid in the channel since the uncoated wires have negligible zeta potential and correspondingly negligible electrophoretic velocity. The measured velocity data from the experiments with MESNA-coated wires represents the observed velocity, U_{obs}, term in Eqn. 2.19. The pressure flow was measured in each test and the velocity terms recorded are corrected for the pressure so the U_{pressure} term drops out of Eqn. 2.19. The maximum contribution to the particle motion from Brownian motion is predicted to be less than 5% of the measured quantities. However any contribution from the directionally-random Brownian motion would be averaged

out over the ensemble of captured images, thus $d_{bm}/\Delta t$, is not retained in the equation for observed velocity of coated wires:

$$U_{obs} = U_{eo} + U_{ep}. \tag{3.3}$$

Equation 3.3 can be used with the measured quantities of U_{eo} (uncoated wires) and U_{obs} (coated wires) to find the electrophoretic velocity, U_{ep}.

3.4 Results and Discussion

Based upon the predicted and measured values of the zeta potential for the glass channel and gold particle (-60 and -27 mV respectively) the electroosmotic velocity is expected to dominate the wire motion. Indeed, the dominance of the electroosmotic motion was directly observed in the experiments. Theoretically, uncoated wires are dragged along by the fluid (moving with U_{eo}) in the direction of the applied electric field. The coated wires were also observed to translate in the direction of the applied electric field, but at a lower velocity, a result of the fact that the wires' electrophoretic velocity is in the opposite direction of the electroosmotic velocity of the fluid.

The experimental results from all six data sets are presented in Table 3.1. The theoretical predictions, using a value of $g_{av} = 1.184$ from (8), are $U_{eo}/E_x = 0.048$ and U_{ep}/E_x = -0.017. The results are presented normalized by the applied electric field, E_x, in order to account for the change in electric field between experiments.

The experimental results from data set 6 agree closely with theoretical predictions. This emphasizes the need for accurate electrode placement in order to

Table 3.1: Experimental Results. Data sets 1 - 5 from initial experiment setup, set 6 from revised experiment setup.

Data Set	Wire Length (μm)	U_{eo}/E_x	U_{ep}/E_x
1	8	0.061	-0.035
2	5	0.086	-0.036
3	11	0.097	-0.050
4	5	0.064	-0.020
5	11	0.076	-0.041
6	6	0.048	-0.016

precisely know the applied electric field.

Additionally, a brief study, with a similar experimental setup, examined the possibility of using electric fields to rotate the nanowires. Details of this study are included in Appendix A.

3.5 Uncertainty Analysis

The following elements of uncertainty within the current experiments are expected to contribute to the difference in theoretical and average experimental values of U_{ep} and U_{eo}: estimates of zeta potential for the gold particle and the glass channel, particle tracking techniques, and possible non-uniformity of applied electric field.

The value of zeta potential used for the glass channel was found in two separate papers (30; 31), in which two different methods were used to experimentally determine the zeta potential. The independent yet consistent measurements of zeta potential of glass in contact with aqueous solution of specified pH give confidence to the value of -60 mV. The measured value of the zeta potential for the gold wires contains inherent uncertainty because of the cylindrical shape of the wires. The

ZetaPALS instrument allows selection of the Hückel or Smoluchowski equations to calculate the zeta potential, both of which were derived based on the assumption of spherical particles. Using an instrument constructed with hardware and software to test spheres may yield significant, yet currently unquantified, measurement errors when the sample contains cylindrical particles.

The reported nanowire velocities were determined using manual particle tracking techniques. The error in the measurement of the distance moved by each wire in a specified time interval was estimated as ±4%.

While the strength of the electrical field applied does not appear directly in the reported results for U_{ep} and U_{eo}, any possible non-uniformity of applied electric field could bias the movement of the individual nanowires. For the direct measurement of the magnitudes of U_{ep} and U_{eo}, however, any error introduced by the measurement of electric field has a correspondingly direct impact. Uncertainty in the measurement of the electric field is introduced by both uncertainty in the distance between the electrodes and uncertainty in the magnitude of the voltage across the electrodes. The distance between the electrodes is a measured quantity in experiment sets 1 to 5, and so contains a reasonable error of ±6%. The voltage applied to the electrodes is a constant 5 Vpp, but there is a small voltage drop across the electrode - water interface resulting in a lower electric field. The voltage across the drops of suspension is measured and found to fluctuate within a small range giving an error of ±5%.

3.6 Summary

In this work, it has been shown experimentally that gold nanowires can be transported through microfluidic channels both by inducing electroosmotic motion within the suspended fluid, and through electrophoretic motion of the nanowires themselves, depending upon conditions. It is clear that the electrophoretic effects can be used to alter the velocity of the nanowires and that the electrophoretic effect can be controlled by the application of surface coatings to the nanowires. The measured values of electrophoretic and electroosmotic velocity agree with theoretical values when the electrode separation is exact.

The more exact nature of the electroosmotic and electrophoretic velocities can also be explored. Currently, the electrophoretic velocities are reported as averages of wires in a variety of orientations, however, the current data and new data may be used to validate the theoretical predictions of an orientational dependence in the velocity.

Chapter 4

Steady-State Numerical Models

4.1 Introduction

A particle undergoing electrophoresis can be affected by the boundary in two ways. In the first case, the characteristic dimension of the channel conveying the particle is of the same order of magnitude as the particle, and the particle is concentrically-located (on the channel centerline). In this first case, the gap width, defined as the distance between the particle and the wall, is symmetric and establishes a symmetric boundary condition with respect to the lengthwise axis of the cylinder. In the second case, an asymmetric boundary condition is established because the particle is nearer to one wall than the others (eccentrically positioned). In this second case, the gap width is defined as the distance between the particle center and the nearest wall. This second case can easily occur if there is a density difference between the particle and suspending fluid. The purpose of this chapter is to examine cylindrical particles in symmetrically and asymmetrically bounded situations and to determine the effects of these boundaries on velocity and orientation.

Current research into bounded electrophoresis can be classified based on the size of the electrical double layer. Typically, the double layer is defined as thick or thin based on the ratio of the particle characteristic length, a, to the double layer thickness, $1/\kappa$. Much of the work with thick double layers ($\kappa a << 1$) dealt with spherical particles (32; 33; 34; 35). Some work has been done with spheroids (36) and with cylinders (37; 38). However, in many practical electrophoresis applications, the ionic concentrations are high enough for the double layers to be thin ($\kappa a >> 1$).

Studies examining the motion of a sphere have focused on both the concentrically positioned case (6) and the eccentrically positioned case (39; 40; 3). Studies have also focused on the bounded electrophoresis of cylinders positioned concentrically (4) and eccentrically (5). Figure 4.1 illustrates the particles and orientations studied in the previously cited works. These studies have found that the translational velocity of the particle is reduced in the concentrically positioned case, while the velocity can be increased in the eccentrically positioned case. As a particle approaches a wall, the electric field strength in the gap region increases faster than the increase in viscous retardation, and the particle is made to move with a higher velocity. Little information has been published on the rotation of cylindrical particles or on the effects of cylinder orientation on the electrophoretic motion. The studies of spherical particles in asymmetrically bounded flows (eccentric position) have demonstrated that the particle will rotate (39; 3). A brief discussion of the rotation of an eccentrically-positioned cylindrical particle exists in (5), but this is for a closed electrophoretic cell as opposed to the open system modeled herein. The purpose of this chapter is to examine cylindrical particles in concentric and

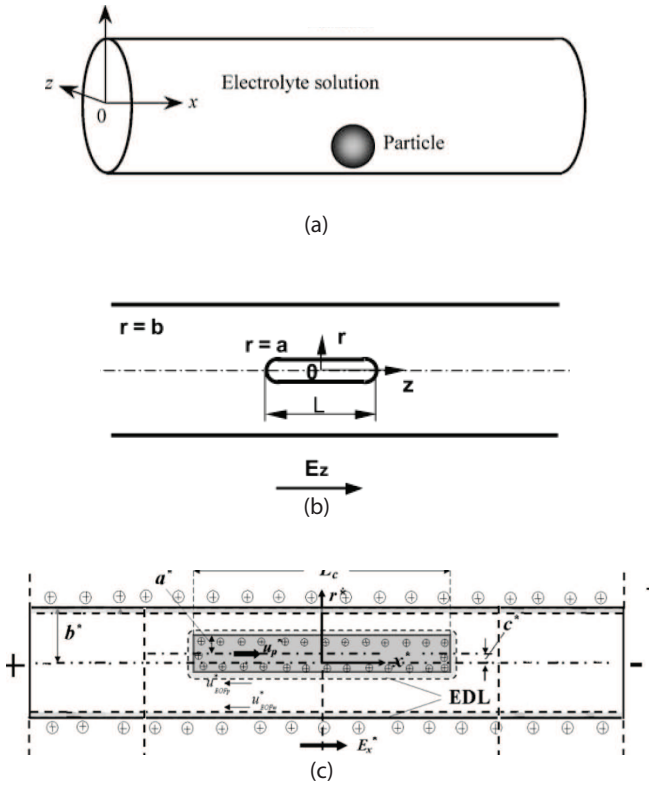

Figure 4.1: Comparison of previous studies of particles undergoing electrophoresis. (a) Diagram of an eccentrically positioned sphere in a microchannel. (3) (b) Diagram of a concentrically positioned cylinder in a microchannel. (4) (c) Diagram of an eccentrically positioned cylinder in a microchannel. (5)

eccentric situations and to determine the effects of these boundaries on velocity and orientation. The current research is viewed as a step toward a complete study of the orientational effects of cylinders under electrophoresis.

4.2 Problem Definition

The electrophoretic motion of cylindrical particles in aqueous fluid-filled circular cylindrical channels is examined. Bounded flow occurs when the channel size is reduced or when the particle reaches equilibrium at an eccentric position in the

channel. In either case, the particle and the fluid will move in the horizontal direction under the action of an applied electric field. A schematic diagram of the particle and channel for each boundary case is shown in Fig. 4.2. The channels are positioned horizontally, with each end leading to a reservoir containing an electrode. The electric field is applied along the x-direction. Gravity acts in the z-direction, the particles are assumed to remain in a constant z-plane during the simulation. The simulations are assumed to start after the particle has come to an equilibrium height due to a balance of gravity and electrostatic repulsion from the channel wall. The reservoirs are open to the atmosphere, so there is no pressure gradient along the channel. Figure 4.2 contains dimensional descriptors for the study. The cylindrical particles are capped by hemispherical ends of radius, a.

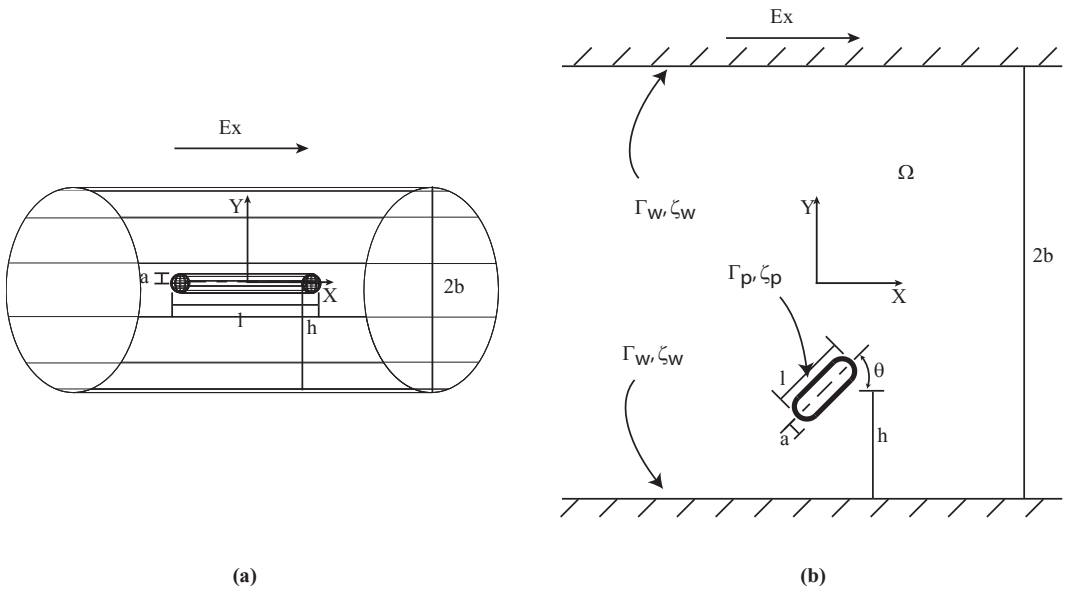

Figure 4.2: Diagram of bounded cases with relevant dimensions. (a) 3-D image showing the cylindrical geometry. (b) Schematic of bounded particle. Gap width (h) defined as distance between particle center and nearest wall. Concentric cases have cylinder center at vertical center of channel. When the particle center is not coincident with the channel center, it is an eccentric case.

The total length of the cylinder is l, giving a particle aspect ratio of l/a. The gap width, h, is defined as the distance from the center of the cylindrical particle to the bounding wall. The diameter of the cylindrical channel is $2b$. The analysis is performed using the following assumptions: the channel walls and particle surfaces are rigid and insulating; the walls and particle surface carry uniform negative zeta potentials, ζ_w and ζ_p respectively; the aqueous solution is an incompressible, Newtonian fluid; the fluid motion is governed by Stokes flow ($Re \approx 10^{-5}$); the electrical double layers are thin ($\kappa a >> 1$); and the particle size is large enough for the Brownian motion effects to be negligible.

4.3 Theoretical Model

4.3.1 Equation Set and Non-Dimensionalization

Two domains exist within the fluid region. The first is within the electrical double layers surrounding the particle and adjacent to the channel walls. The remainder of the fluid constitutes the second region (the fluid domain is denoted by Ω). With the thin double layer assumption, the flow within the double layer is described by electroosmotic flow (6). Since the width of the double layer is much smaller than a characteristic length of the domain ($\kappa a >> 1$), the electroosmotic flow of the double layer creates a slip velocity boundary condition on the channel and particle surfaces. The boundaries are denoted by Γ_w for the channel walls, Γ_p for the particle surface, Γ_{in} for the inlet, and Γ_{out} for the outlet. The governing equations for the solution of the motion of the cylindrical particle are presented below.

Outside of the electrical double layer, the fluid has no net charge density and

so the electrical potential, ϕ, is governed by

$$\nabla^2\phi = 0 \text{ in } \Omega \tag{4.1}$$

with the boundary conditions

$$\mathbf{n}\cdot\nabla\phi = 0 \text{ on } \Gamma_w \text{ and } \Gamma_p \tag{4.2}$$

$$\phi = \phi_0 \text{ on } \Gamma_{in},\ \phi = 0 \text{ on } \Gamma_{out} \tag{4.3}$$

where ϕ_0 is the applied electric potential and $\mathbf{n}$ is the unit normal pointed into the fluid domain.

The fluid domain is governed by the standard hydrodynamic equations for Stokes flow because there is no net charge density to be acted on by the electric field. The equations governing the fluid flow are

$$\nabla\cdot\mathbf{u} = 0 \text{ in } \Omega \tag{4.4}$$

$$\mu\nabla^2\mathbf{u} + \nabla p = 0 \text{ in } \Omega \tag{4.5}$$

where $\mathbf{u}$ is the liquid flow velocity, μ is the fluid viscosity, and p is the pressure in the fluid domain. As mentioned, the boundary conditions for the fluid on the walls and particle surfaces are slip velocities caused by the electroosmotic flow in the thin electrical double layers. Since the walls are fixed, the fluid boundary condition is a slip velocity

$$\mathbf{u} = \frac{\varepsilon\zeta_w}{\mu}(\mathbf{I} - \mathbf{nn})\cdot\nabla\phi \text{ on } \Gamma_w. \tag{4.6}$$

The applied electric field will cause an electroosmotic fluid velocity in the double

layer surrounding the particle, but will also cause the particle to translate. Thus, the boundary condition for the fluid on the particle surface is the sum of the electroosmotic velocity of the fluid at the particle surface and the velocity of the particle

$$\mathbf{u} = U_p \mathbf{e}_x + \frac{\varepsilon \zeta_p}{\mu}(\mathbf{I} - \mathbf{nn}) \cdot \nabla \phi \text{ on } \Gamma_p. \tag{4.7}$$

The constants in the boundary conditions are the permittivity of the electrolyte solution, ε, the identity tensor, $\mathbf{I}$, and the unit vector in the x-direction, $\mathbf{e}_x$. Also present is U_p, the translational velocity of the particle in the x-direction. The quantity $(\mathbf{I} - \mathbf{nn}) \cdot \nabla \phi$ defines the electric field tangential to the surface.

When the particle is moving with a steady-state velocity, the net force exerted by the fluid flow on the particle is zero. The hydrodynamic force on the particle is given by

$$\mathbf{F} = \int \bar{\bar{\sigma}} \cdot \mathbf{n} d\Gamma_p = 0 \tag{4.8}$$

where $\bar{\bar{\sigma}}$ is the stress tensor given by

$$\bar{\bar{\sigma}} = -p\mathbf{I} + \mu[\nabla \mathbf{u} + (\nabla \mathbf{u})^T]. \tag{4.9}$$

The system of equations is non-dimensionalized using the following parameters: length a, where a is the particle radius; applied electric voltage, ϕ_0; and a velocity defined as $U_\infty = \frac{\varepsilon \zeta_p}{\mu} \frac{\phi_0}{a}$, which is the electrophoretic velocity of the particle in an unbounded flow. Using these characteristic dimensions and letting $\mathbf{x} = a\mathbf{x}^*$, $\mathbf{u} = U_\infty \mathbf{u}^*$, $p = \frac{\mu U_\infty}{a} p^*$, and $\phi = \phi_0 \phi^*$, the non-dimensionalized form of the

governing equations is

$$\nabla^{*2}\phi^* = 0 \text{ in } \Omega \tag{4.10}$$

$$\nabla^* \cdot \mathbf{u}^* = 0 \text{ in } \Omega \tag{4.11}$$

$$\nabla^{*2}\mathbf{u}^* + \nabla^* p^* = 0 \text{ in } \Omega. \tag{4.12}$$

The boundary conditions become

$$\mathbf{n} \cdot \nabla^* \phi^* = 0 \text{ on } \Gamma_w \text{ and } \Gamma_p \tag{4.13}$$

$$\phi^* = 1 \text{ on } \Gamma_{in},\ \phi^* = 0 \text{ on } \Gamma_{out} \tag{4.14}$$

$$\mathbf{u}^* = \gamma(\mathbf{I} - \mathbf{nn}) \cdot \nabla^* \phi^* \text{ on } \Gamma_w \tag{4.15}$$

$$\mathbf{u}^* = U_p^* \mathbf{e}_x + (\mathbf{I} - \mathbf{nn}) \cdot \nabla^* \phi^* \text{ on } \Gamma_p \tag{4.16}$$

where γ is the ratio of zeta potential of the channel walls to that of the particle surface ($\gamma = \zeta_w/\zeta_p$). The hydrodynamic force on the particle is non-dimensionalized as $F = \mu U_\infty a F^*$, which gives

$$\mathbf{F}^* = \int \overline{\overline{\sigma}}^* \cdot \mathbf{n} d\Gamma_p{}^* = 0. \tag{4.17}$$

All of the starred variables represent non-dimensional quantities.

4.3.2 Solution Approach

Two different methods are available to solve the problem, superposition and iteration. The superposition method, described in (5; 38), breaks the velocity and pressure fields into two components in order to solve for $U_p{}^*$. The decomposed

equations are

$$\mathbf{u}^* = \mathbf{u}_1^* + U_p^* \mathbf{u}_2^* \tag{4.18}$$

$$p^* = p_1^* + U_p^* p_2^*. \tag{4.19}$$

The fluid boundary conditions in the problem of $\mathbf{u}_1^*$ are $\mathbf{u}_1^* = \gamma(\mathbf{I} - \mathbf{nn}) \cdot \nabla^* \phi^*$ on the channel walls, $\mathbf{u}_1^* = (\mathbf{I} - \mathbf{nn}) \cdot \nabla^* \phi^*$ on the particle surface, and no applied pressure gradient. This defines the electrokinetic problem where the particle is not translating. The solution to this problem yields a net force in the x-direction on the particle, F_1^*. The fluid boundary conditions for the second problem of $\mathbf{u}_2^*$ and p_2^* are $\mathbf{u}_2^* = 0$ on the channel walls, $\mathbf{u}_2^* = 1$ on the particle surface, and no applied pressure gradient. These conditions define the hydrodynamic problem of the particle translating through still fluid. The solution to this problem yields a net force in the x-direction on the particle, F_2^*. The total net force on the particle in the x-direction in the complete problem must sum to zero, allowing the value of U_p^* to be found by solving

$$F_1^* + U_p^* F_2^* = 0 \tag{4.20}$$

$$U_p^* = -\frac{F_1^*}{F_2^*}. \tag{4.21}$$

The iterative approach is described in (4). The general velocity boundary condition on the particle surface contains both the particle velocity, U_p^* and the electroosmotic slip velocity. In the iterative method, the value of U_p^* is estimated and the complete problem solved to determine the sum of the forces. In steady state, the sum of the forces on the particle in the x-direction must be zero, so

the value of U_p^* is iteratively varied and a new solution is found until the sum of the x-direction forces approaches zero. Both the superposition and iterative methods were tested and found to yield identical results. The iterative solver is more computationally intensive, but it is the method of choice for the analyses in this paper. The iterative solver has the advantage that the force and torque components of primary interest are inherent in this method, rather than split over two solution components. This eases determination of the validity of the steady-state assumption and the transition to nonsteady modeling.

4.4 Numerical Method

The above set of equations defines the electrophoretic problem to be solved. In order to readily solve this problem, a coordinate transformation is performed. The particle is fixed and its translational velocity, U_p^*, is transferred to the channel walls. This creates the following boundary conditions for the fluid motion on the walls and the particle surface:

$$\mathbf{u}^* = U_p^* \mathbf{e}_x + \gamma(\mathbf{I} - \mathbf{nn}) \cdot \nabla^* \phi^* \text{ on } \Gamma_w \tag{4.22}$$

$$\mathbf{u}^* = (\mathbf{I} - \mathbf{nn}) \cdot \nabla^* \phi^* \text{ on } \Gamma_p. \tag{4.23}$$

A commercial finite element package, Comsol Multiphysics (Comsol, Inc; Burlington, MA), was used to solve the above set of equations. A mesh was created from unstructured triangular elements with fine elements on the particle surface and growth to coarser elements in the bulk flow. The fluid velocity, $\mathbf{u}$, is not a specified quantity on the inlet and outlet surfaces (Γ_{in} and Γ_{out}). Rather, the fluid

velocity, $\mathbf{u}$, on Γ_{in} and Γ_{out} is solved using the coupled Navier-Stokes and electrical governing equations with fluid velocity boundary conditions on Γ_w and Γ_p. Following the iterative solution method, the value of U_p^* is varied until the sum of the hydrodynamic forces in the x-direction F^* approaches zero. After testing the solution method, it was found that the relationship between U_p^* and F^* is linear, therefore the final value of particle velocity can be found by interpolating two trial values. An example of the numerical code used is included in Appendix B.

4.4.1 Solution Geometry

The electrophoretic problem can be addressed in one of three geometries: two dimensional, axisymmetric, and three dimensional. In two dimensions, a planar slice taken through the axis of the channel and the center of the particle is used as the solution geometry. This is advantageous because it is possible to take this slice regardless of where the particle is situated in the channel. However, a two-dimensional slice is the geometry with the least resemblance to the physical situation. The assumption of planar two dimensionality precludes the proper study of the cylindrical geometry that is present, since the two-dimensional slice would model a slit. One way of addressing this shortcoming is to use a two dimensional slice with axisymmetric assumption for the out-of-plane space. This method correctly addresses the geometry but is limited to cases where the particle is located on the centerline of the channel and aligned along it. Finally, it is possible to model the correct geometry with the particle at an arbitrary location with a three-dimensional model, but at the cost of greatly increased computational time.

4.4.2 Comparisons

In order to test the validity of the solution geometries and ensure the numerical results are reasonable, comparisons were made between our solutions from the three solution geometries and previously published results of bounded electrophoretic flow. The first comparisons were made between our results and the results of (6) for a sphere translating in a circular, cylindrical channel. Keh and Anderson (6) used a method of reflections to derive an expression for the velocity of the sphere in terms of the sphere radius, a, and the channel radius, b. Non-dimensionalized by U_∞, their expression is

$$U_{Keh}{}^* = [1 - 1.28987(\frac{a}{b})^3 + 1.89632(\frac{a}{b})^5 - 1.02780(\frac{a}{b})^6 + O((\frac{a}{b})^8)](1-\gamma). \quad (4.24)$$

The difference between our numerical results and those of (6) is 0.1% to 6.0% for the two dimensional geometry and 0.04% to 0.6% for both the axisymmetric and the three-dimensional geometry over the range of a/b from 1/35 to 1/2. A graphical comparison of these results is included in Fig. 4.3. Similarly, a comparison was made between our results and the results of (4) for the symmetrically-bounded flow of a cylindrical particle in a circular cylindrical channel. Comparison to their results indicates an agreement to within 1.5% to 3.6% for the two-dimensional geometry and 0.3% to 3.3% for both the axisymmetric and the three-dimensional geometry for values of a/b from 1/8 to 2/5. The axisymmetric and three-dimensional geometries produce results in better agreement with published studies. These comparisons reinforce the notion that the two-dimensional geometry provides the least accurate description of the physical situation. Since the axisymmetric geometry

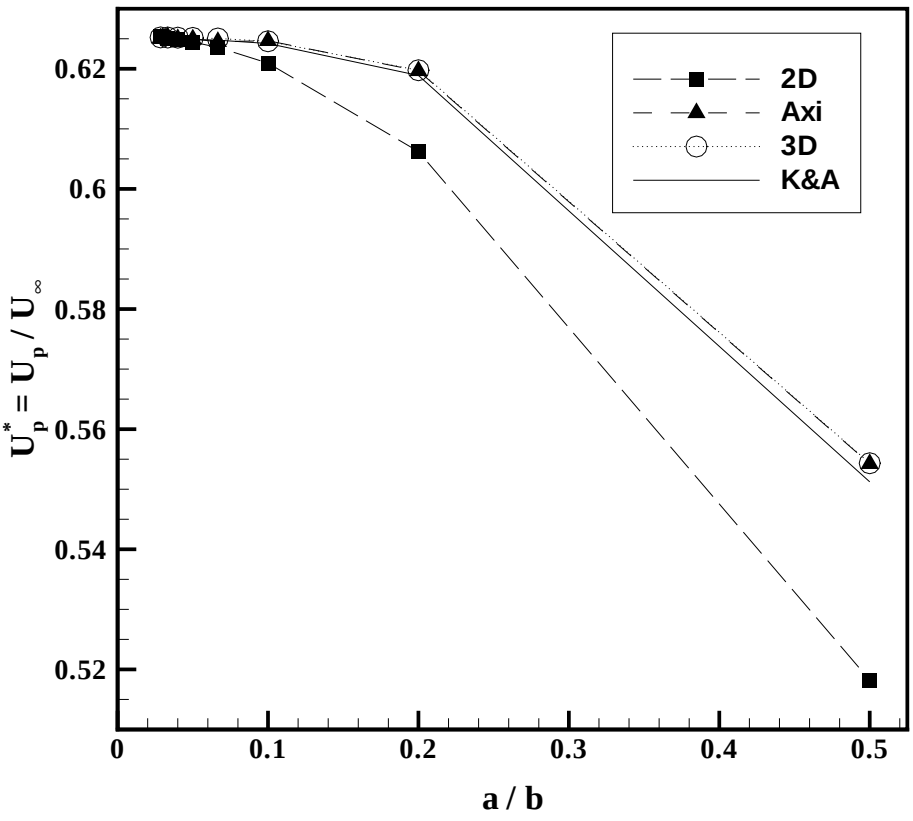

Figure 4.3: Comparison of particle velocity versus ratio of particle cap radius to channel half-width (a/b) predicted using three different solution geometries (2D, 3D, axisymmetric) and analytical solution from (6).

can not be used to model all the cases of interest, the remainder of the steady-state results presented herein have been calculated using a three-dimensional geometry.

4.5 Results and Discussion

Although results are presented nondimensionally, the values used have been selected to model a physical situation with a particle radius $a = 1.5$ μm, with an

applied electric field of 500 V/m, and with density, ρ, and viscosity, μ, representing an aqueous solution. The electrophoretic motion of a cylindrical particle was studied for symmetrically-bounded (concentrically-located) and asymmetrically-bounded (eccentrically-located particle) flows over a range of particle aspect ratios, zeta potential ratios (γ), and particle angle to the horizontal (θ). In each case, the nondimensional particle velocity, ${U_p}^*$, is found for concentric and eccentric cases over a range of nondimensional gap widths, h^*. The current numerical model limits the minimum gap width to h^*=1.5 in the concentric case. In the eccentric case, the gap width can be reduced to h^*=1.1. The channel radius is held constant at b^*= 35 for all the eccentric cases presented below. In the results that follow, the theoretical value of ${U_p}^*$ is $1-\gamma$ (1) for electrophoretic motion with opposing electroosmotic flow and no boundary effects. As can be inferred from this result, the particle will not translate if the zeta potentials of the channel walls and particle surface are equal ($\gamma = 1$). All of the results presented in Sec. 4.5.1 are found assuming the cylindrical particle remains at a fixed position. This can provide valuable insight into the motion of the particle, but it is important to note that there are situations where the position of the particle may change. These situations are examined using nonsteady solutions in Sec. 4.5.2.

4.5.1 Effect of Parameter Variations on Particle Velocity over a Range of Gap Widths

4.5.1.1 Effect of Aspect Ratio

To capture the effect of the particle aspect ratio, cases with four aspect ratios were run: l/a = 2 (sphere), 6, 12, and 24. For these cases, the particles were aligned

with the horizontal ($\theta = 0$) and had $\gamma = 0.375$. These results are presented in Fig. 4.4. In the concentric case, Fig. 4.4a shows that reducing the channel size

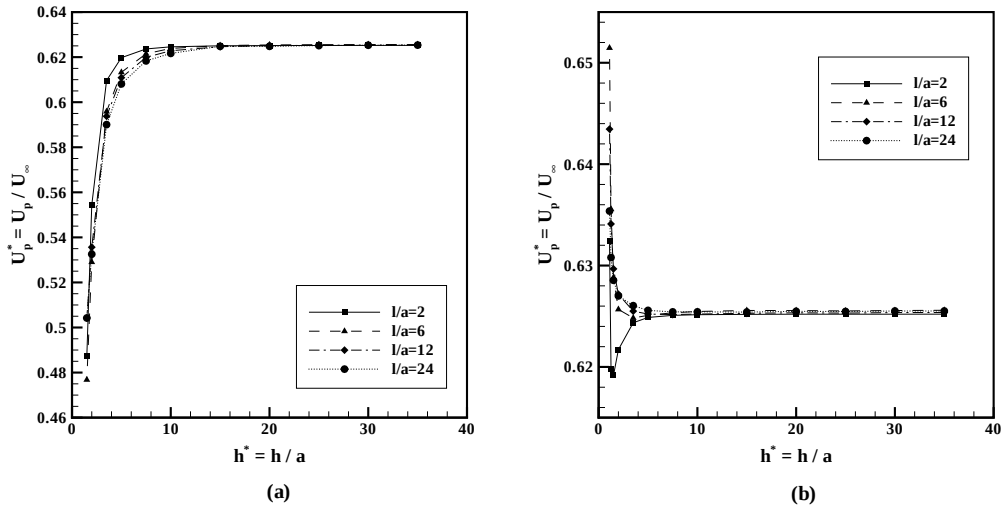

Figure 4.4: Effect of particle aspect ratio (l/a) on particle velocity as a function of gap width. The theoretical value of $U_p{}^*$ for flow without boundary interactions is $1-\gamma = 0.625$. (a) Concentric case with varying channel radius. (b) Eccentric case with constant channel diameter (b^*=35). Data from 3D numerical models.

causes a reduction in the velocity of the particle, and that the larger the aspect ratio of the particle the greater the effect for gap widths of 2 or larger. At a gap width of five, the velocity of the sphere is reduced by 1%, compared to 2%, 2.3%, and 2.8% for $l/a = 6$, 12, and 24 respectively. The reduction in velocity is much larger at a gap of two, 11% for the sphere and 15% for the other aspect ratios. At the final gap width of 1.5, the velocity reduction has reached 20% for the aspect ratios considered. As the cylindrical particle approaches the wall the electric field is increased due to constriction of the field between the particle and the wall. The velocity of the particle decreases as the gap width decreases because the increased viscous retardation from the constricted fluid has a larger effect than the increase

in electric field.

The effect of the boundary walls for an eccentrically-located particle (Fig. 4.4b) is only significant at the smallest gap widths (h^* <2) and varies depending on the aspect ratio of the particle. The velocity of the sphere is reduced by up to 1% as the gap is reduced to h^*=1.25, but the velocity is increased by over 1% (relative to the sphere velocity in unbounded flow) at h^*=1.1. The velocity of the cylinders tested does not decrease at any gap width, but increases monotonically. The cylinders increase in velocity between 2% and 4% at h^*=1.1, with l/a=6 being the fastest. The behavior of the velocity changes can be explained by the competing effects of increased electric field and the increased viscous retardation as the wall is approached. As opposed to the concentric case, the wall is only approached in one direction which means the viscous retardation is reduced, but so is the electric field. The velocity of the sphere is reduced initially because the viscous retardation dominates until h^*=1.1 where the electric field is sufficiently increased to overcome the viscous retardation. In the case of the cylinders, the greater surface area increases the effect of the electric field causing the viscous retardation to be overcome at greater gap widths than the sphere. These results can be compared to those of (3), which found that the translational velocity of a sphere at an eccentric location was greatly enhanced ($\sim$ 20%) by the presence of the wall. In Ye, Xuan, and Li's study (3), the gap width was reduced to a smaller value than possible is the current numerical model, explaining the notable difference in maximum velocity change between the previous study (3) and the results presented here. The behavior of the velocity at larger gap widths is similar, both studies show a slight decrease in velocity followed by a rapid increase as the

gap width is reduced.

4.5.1.2 Effect of Zeta Potential Ratio

The zeta potential of the walls was varied in order to produce cases with γ = 0.375, 0.75, 1.5, and -0.375. The particles were aligned with the horizontal ($\theta = 0$) and had $l/a = 6$. The results for the concentric and eccentric cases are shown in Fig. 4.5. Evident in either case is that the primary effect of altering γ is to change

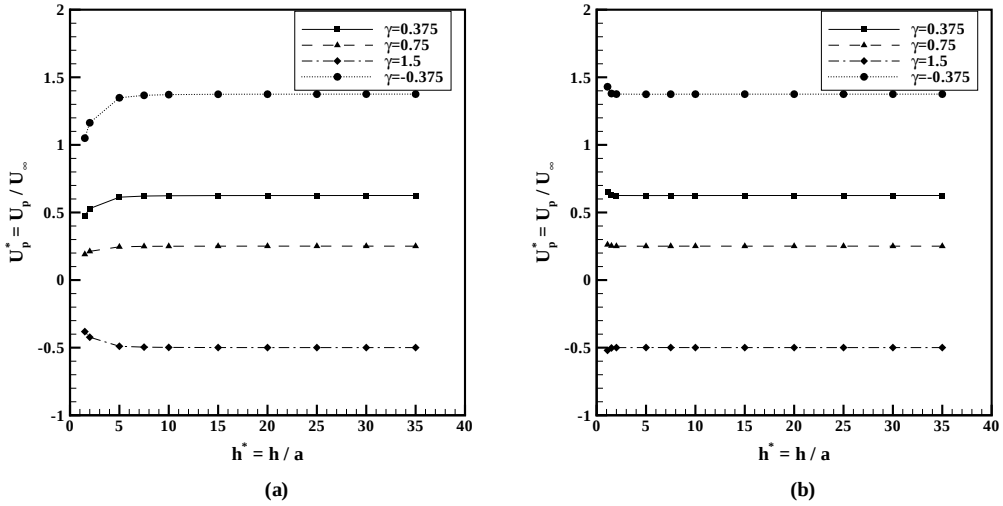

Figure 4.5: Effect of zeta potential ratio (ζ_w/ζ_p) on particle velocity as a function of gap width. The theoretical value of $U_p{}^*$ for flow without boundary interactions is $1-\gamma$. (a) Concentric case with varying channel radius. (b) Eccentric case with constant channel diameter (b^*=35). Data from 3D numerical models.

the translational velocity of the particle, since the theoretical unbounded velocity is $U_p{}^* = 1 - \gamma$. The values for all cases are in agreement with predictions for unbounded flow. For all values of γ in the concentric case, the velocity is reduced by 15% at a gap width of two and 24% at a gap width of 1.5 (Fig. 4.5a).

In the eccentric case (Fig. 4.5b), the velocity is unchanged at h^*=2, increased by 0.6% at h^*=1.5, and increased by 4% at h^*=1.1 for all values of γ. These

results demonstrate that altering γ does not change the effect of the boundaries on the particle velocity. The effect of changing γ merely serves to redistribute the electroosmotic velocity between the particle surface and the channel walls. The magnitude of the particle velocity changes proportionally to the magnitude of the zeta potential ratio, thus in and of itself a change in the zeta potential ratio neither increases nor decreases the significance of the boundary effect.

4.5.1.3 Effect of Particle Angle

The angle (θ) of the particle was varied from zero to 90° to assess the impact of initial orientation on the particle velocity. In these simulations, the particles had $l/a = 6$, $\gamma = 0.375$, and a range of gap widths from $h^* = 35$ to h^*=5. The use of smaller gap widths was not possible since the particle would be in contact with the walls at larger angles. The results presented in Fig. 4.6 show that the effect of the angle is similar in both boundary configurations: as the angle of the particle is increased, the velocity is reduced. However, the effect is more significant in the concentric case, with velocity reductions of 2.0% to 3.6% as the angle goes from zero to ninety. (It is noted that, strictly speaking, the particle is not concentric with the cylindrical channel since the particle is at an angle to the axial direction. However, the term 'concentric' is used in this paper to denote the case for which the particle center is located on the cylindrical channel center.) In contrast, for an eccentrically-located particle, the velocity is reduced by an order of magnitude less, namely 0.08% to 0.3%. Angling the particle reduces the effective gap width at the end angled toward the wall. This increases the viscous retardation caused by the wall, and reduces the concentration of the electric field to a very small area.

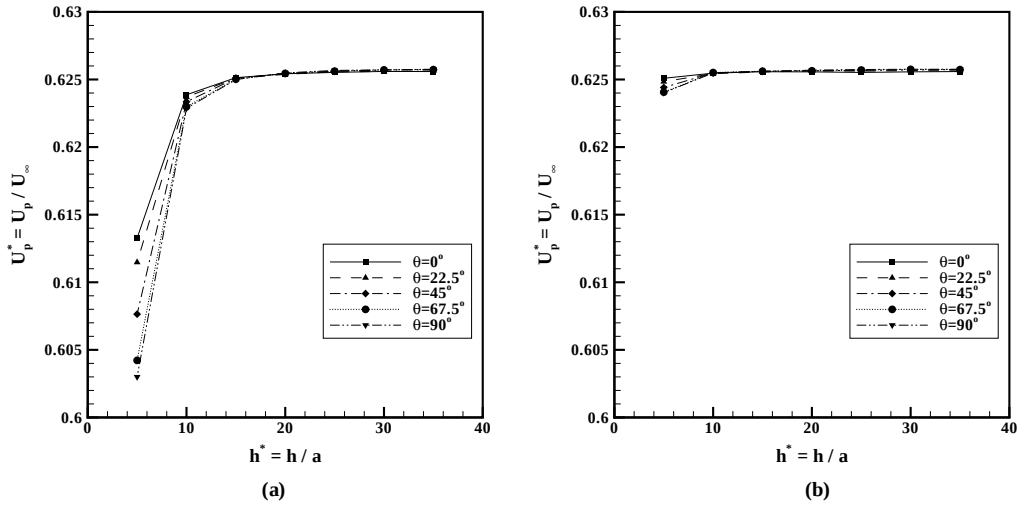

Figure 4.6: Effect of initial particle orientation (θ) on particle velocity as a function of gap width. These results are from a steady-state simulation. The theoretical value of $U_p{}^*$ for flow without boundary interactions is 0.625. (a) Concentric case with varying channel radius. (b) Eccentric case with constant channel diameter (b^*=35). Data from 3D numerical models.

Both of these effects reduce the velocity of the particle.

4.5.1.4 Effect of Channel Diameter on Eccentrically-located Particle

The effect of channel diameter was calculated while holding a particle with $l/a = 6$, $\theta = 0°$, and $\gamma = 0.375$ at an eccentric location with a fixed gap width. Effectively, this geometry incorporates the independently discussed effects of narrowing the channel and placing the particle near a wall. Figure 4.7 includes the results for non-dimensional gap widths (h^*) of 10, five, and two. When the particle is closest to the wall ($h^* = 2$), the small gap width dominates and no change in velocity is observed for a reduction in channel diameter from 35 to 10. At positions slightly further from the wall ($h^* = 5$ and $h^* = 10$), the effect of narrowing the channel is more pronounced, causing a reduction in particle velocity ($U_p{}^* = U_p/U_\infty$) at a

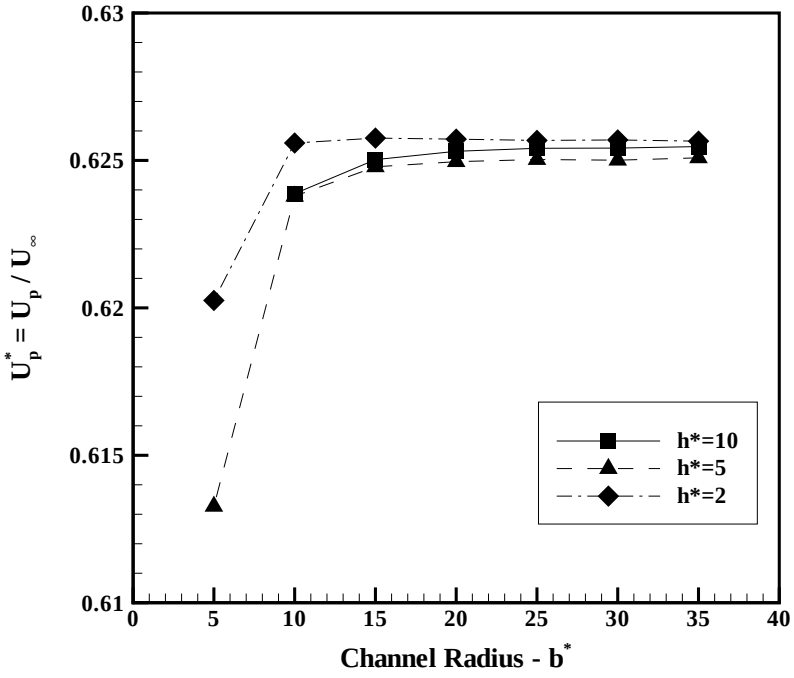

Figure 4.7: Effect of channel diameter on particle velocity for fixed gap width. This is effectively the combined case of an eccentrically-positioned particle and a relatively narrow channel. Nondimensional channel diameters (b^*) of 5 and greater, with nondimensional gap widths (h^*) of 10, 5, and 2. Data from 3D numerical models.

non-dimensional channel radius (b^*) as large as 15.

The results in Fig. 4.7 represent the competing effects of viscous retardation from the walls (most noticeably observed in the narrowest of channels) and the concentration of the electric field between a wall and a very nearby particle. At a non-dimensional gap width ($h^* = h/a$) of two, the electric field is concentrated enough in the space between the particle and the wall to overcome the increase in retardation from the wall, thereby, overall, an increase in the particle velocity is observed. But at a non-dimensional gap width ($h^* = h/a$) of five, the electric

field is not concentrated enough in the space between the particle and the wall to overcome the effect of viscous retardation, and a decrease in particle velocity is observed. And at a non-dimensional gap width ($h^* = h/a$) of 10, the particle is far enough away from the wall that the electric field is nearly symmetric about the particle (i.e. very little concentration between the wall and the particle), and also far enough from the wall that the viscous retardation is minimal.

4.5.2 Steady State Assumption

The steady-state results presented above were found by solving for the translational velocities that give a sum of hydrodynamic forces on the particle of zero. Situations can arise where the forces sum to zero but a torque exists on the particle. The existence of a torque on the particle is a violation of the steady-state approximation, suggesting that while steady-state solutions are often used and can provide general insight into the behavior of the particle, care must be exercised when interpreting the results. In such cases, nonsteady models are appropriate to more accurately represent the (nonsteady) particle motion.

The development of torque on the particle occurs in situations with strong asymmetry, either with a particle close to the wall (eccentric position) or with one angled with respect to the horizontal ($\theta \neq 0°$). Two such conditions are shown in Fig. 4.8. Both the cylinder surfaces and channel walls are insulating, creating an asymmetric electric field around the particle. The fields would be uniform in the absence of the particle. The boundary conditions dictate the field remains parallel to the surfaces of the particle and channel. The presence of the particle causes the field to distort creating asymmetries that necessitate nonsteady study. Figure 4.8a

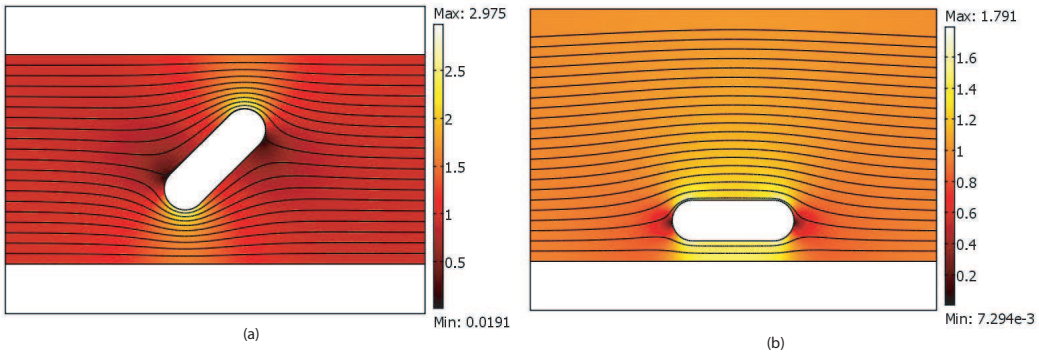

Figure 4.8: Asymmetric distribution of electric field with velocity streamlines. The particle has $l/a = 6$ and $\gamma = 0.375$. Contours represent levels of $\nabla^*\phi^*$. (a) Particle center located at center of channel, $\theta = 45°$ and nondimensional gap width of five. (b) Eccentrically-positioned particle, particle aligned with horizontal and nondimensional gap width of two.

shows the asymmetric electric field around an angled particle ($\theta = 45°$) in a narrow channel. The higher velocities through the small gaps at the ends of the particle create a torque on the particle. Similarly, the asymmetric electric field around the particle with a gap width of five can be seen in Fig. 4.8b. Here the colors represent the strength of the electric field, the whites the strongest and the darkest reds the weakest, while the streamlines show the fluid velocity around the particle. This figure shows that the electric field is stronger in the region between the particle and the wall than on the unbounded side. The velocities of the flow and particle are directly related to the strength of the electric field, so by increasing the strength of the electric field, the velocities are increased, explaining the increase in particle velocity at smaller gap widths. Higher velocities along the bounded side of the particle give rise to a torque about the center of the particle. Nonsteady numerical models will be explored in Chapter 5 to address these situations.

4.6 Summary

This chapter considers the bounded electrophoretic motion of cylindrical particles in circular cylindrical microchannels. The particle is positioned so that the channels walls either symmetrically or asymmetrically bound the particle, *i.e.* the particle is concentrically-located (symmetric) or highly eccentrically-located in a channel (asymmetric). The velocity of the cylinder was calculated using a steady-state model for a variety of gap widths between the particle and the boundaries, and for various particle aspect ratios, zeta potential ratios, and particle angles. Selected nonsteady simulations were also performed.

Concentric Case:

Based on the steady-state simulations, the velocity of the particle is decreased as the particle gets nearer to the wall (smaller gap width) in a relatively narrow channel. Increasing the particle aspect ratio and the particle angle to the horizontal reduced the particle velocity in a narrow channel, while the percentage of velocity reduction was constant for all zeta potential ratios.

Eccentric Case:

Again, based on steady-state simulations, the velocity of an eccentrically-located particle increases as the particle gets nearer to the wall (smaller gap width). As the particle's aspect ratio increases, so does the particle velocity. But, as particle angle increases, the particle velocity decreases. The magnitude of the particle velocity changes proportionally to the magnitude of the zeta potential ratio, thus in and

of itself a change in the zeta potential ratio neither increases nor decreases the significance of the boundary effect.

Chapter 5

Nonsteady Numerical Results

5.1 Introduction

A method for controlling the positioning of individual suspended particles may be to design a microfluidic system based on standard electrophoresis, either on its own or in conjunction with dielectrophoresis. In order to make efficient use of electrophoretic devices, it is desirable to minimize the device size. Thus, an understanding of the behavior of cylindrical particles undergoing electrophoresis in relatively narrow channels has the potential to enable further uses of such non-spherical particles as critical device elements. The current chapter begins to describe the transport of cylindrical particles undergoing (DC) electrophoresis in microfluidic channels, and focuses on specific conditions that cause their positions and orientations to be nonsteady in nature.

The broadest delineation of previous work on electrophoresis of particles centers on the thickness of the electrical double layer surrounding the particle. The double layer thickness is inversely defined by the Debye length, $1/\kappa$, and is usu-

ally compared to a characteristic particle dimension, a, to form a nondimensional descriptor of double layer thickness, κa. Thick double layers are defined as $\kappa a \ll 1$ and thin double layers as $\kappa a \gg 1$. The ionic concentration of the suspending fluid determines the double layer thickness, greater ion concentration yields thinner double layers. For the purposes of this chapter, and many practical electrophoresis applications, the double layers are assumed to be thin in comparison to the particle dimension ($\kappa a \gg 1$). The motion of spheres (6; 39; 40; 3) and cylinders (4; 5) has been studied for thin double layers and bounded channels. However, few have addressed the orientation of non-spherical particles or even briefly studied the motion over time (5). A study by Ye and Li (41) looked at the motion of a spherical particle as it traveled around a corner in a T-junction. As part of a larger work, Liu et al. (5) briefly examined the translation and rotation of an eccentrically-positioned cylindrical particle. However, Liu et al. (5) studied the motion in a closed electrophoretic system as opposed to the open system under current consideration. The work in 4.5 focused mainly on steady-state simulations (particle held fixed) of cylindrical particles at multiple orientations. The purpose of this chapter is to study the nonsteady motion of cylindrical particles through narrow channels, specifically to determine the effect of the initial orientation.

5.2 Problem Definition

A diagram of the system under investigation is shown in Fig. 5.1. The cylindrical particle translates through the aqueous fluid filled channel under the action of electrophoresis. The system modeled has fluid reservoirs open to the atmosphere so that no pressure gradient exists along the length of the channel. In the absence

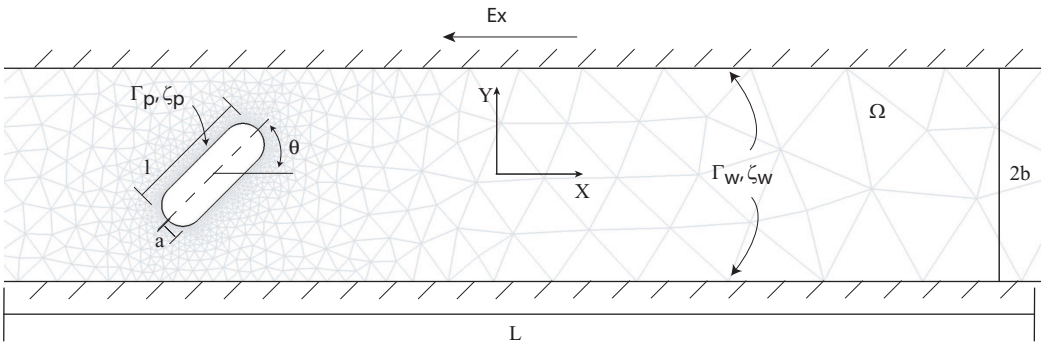

Figure 5.1: Diagram of cylindrical particle at initial position in channel with relevant dimensions and variables. Unstructured triangular mesh of computational domain included to illustrate increase in mesh density around the particle.

of a pressure gradient, the fluid motion is plug flow in the direction of the electric field. The particle is modeled as having a zeta potential greater than that of the channel walls which results in motion opposite to the fluid direction, in the positive x-direction. As in Chapter 4, gravity acts in the z-direction and the particles maintain a constant z-location. The geometrical descriptors of the system are included in Fig. 5.1. The particle has a length, l, and is capped by hemispherical ends with radius, a. The angle made by the particle to the horizontal is tracked by θ. The channel that the particle is moving through has a length of L and a radius of b. The fluid domain is denoted by Ω with boundaries Γ_w and Γ_p on the channel walls and particle surface respectively. With fluid motion in the direction of the electric field the right boundary is the inlet and the left boundary is the outlet denoted by Γ_{in} and Γ_{out}. The particle and channel walls are assumed to be rigid as well as insulating and carry constant and uniform negative zeta potentials, ζ_p and ζ_w respectively. The aqueous fluid is incompressible and Newtonian with sufficient ionic concentration for the electrical double layers to be thin ($\kappa a \gg 1$). The motion of the fluid is governed by Stokes flow (Re $\approx 10^{-5}$) and the particle

dimensions are large enough that Brownian motion is negligible.

5.3 Equation Set and Non-Dimensionalization

The computational domain, denoted by Ω, consists of the fluid in the channel outside of the electrical double layers on the particle and the walls. Under the thin double layer assumption, the fluid motion within the double layer can be reduced to a velocity boundary condition on the surface, which is defined as the electroosmotic velocity of the fluid in the double layer (6). The equations governing the motion of the cylindrical particle are summarized below.

The fluid domain under consideration, Ω, has zero net charge density so the electric potential, ϕ, is described by

$$\nabla^2\phi = 0 \text{ in } \Omega \tag{5.1}$$

with a specified potential, ϕ_0, applied across the inlet and outlet and insulting surfaces on the channel walls and particle

$$\phi = \phi_0 \text{ on } \Gamma_{in},\ \phi = 0 \text{ on } \Gamma_{out} \tag{5.2}$$

$$\mathbf{n} \cdot \nabla\phi = 0 \text{ on } \Gamma_w \text{ and } \Gamma_p. \tag{5.3}$$

The vector, $\mathbf{n}$, is a unit normal that points from the solid surfaces into the fluid domain.

The fluid velocity, $\mathbf{u}$, is described by the Stokes flow equations due to the low

Reynolds number and lack of net charge density,

$$\nabla \cdot \mathbf{u} = 0 \text{ in } \Omega \tag{5.4}$$

$$\mu \nabla^2 \mathbf{u} + \nabla p = 0 \text{ in } \Omega. \tag{5.5}$$

The pressure in the channel is p and the fluid viscosity is μ. The fluid boundary condition on the channel walls is a slip velocity defined by the electroosmotic flow in the electric double layer

$$\mathbf{u} = \frac{\varepsilon \zeta_w}{\mu} (\mathbf{I} - \mathbf{nn}) \cdot \nabla \phi \text{ on } \Gamma_w. \tag{5.6}$$

The boundary condition on the particle surface contains the electroosmotic slip velocity from the fluid but also must account for the translation and rotation of the particle,

$$\mathbf{u} = \mathbf{U}_p + \bar{\omega_p} \times (\mathbf{x}_p - \mathbf{X}_p) + \frac{\varepsilon \zeta_p}{\mu} (\mathbf{I} - \mathbf{nn}) \cdot \nabla \phi \text{ on } \Gamma_p. \tag{5.7}$$

The boundary conditions contain the permittivity of the electrolyte solution, ε, the identity tensor, $\mathbf{I}$, the translational velocity of the particle, $\mathbf{U}_p$, the rotational velocity, $\bar{\omega_p}$, the position vector of the particle surface, $\mathbf{x}_p$, and the position vector of the center of the particle, $\mathbf{X}_p$. The quantity $(\mathbf{I} - \mathbf{nn}) \cdot \nabla \phi$ defines the electric field tangential to the surface.

The translational and rotational velocities are determined by the forces and torques exerted on the particle by the fluid. The stress tensor, $\bar{\bar{\sigma}}$, describes the

surface stress exerted on the particle by the fluid

$$\bar{\bar{\sigma}} = -p\mathbf{I} + \mu[\nabla\mathbf{u} + (\nabla\mathbf{u})^T]. \tag{5.8}$$

The stress tensor is used to define the force and torque acting on the particle

$$\mathbf{F} = \int \bar{\bar{\sigma}} \cdot \mathbf{n} d\Gamma_p \tag{5.9}$$

$$\mathbf{T} = \int (\mathbf{x}_p - \mathbf{X}_p) \times (\bar{\bar{\sigma}} \cdot \mathbf{n}) d\Gamma_p. \tag{5.10}$$

Newton's second law, along with the particle mass, m, and the moment of inertia, I, are used to find the translational and rotational components of the particle's velocity

$$\mathbf{F} = m\frac{d\mathbf{U}_p}{dt} \tag{5.11}$$

$$\mathbf{T} = I\frac{d\bar{\omega_p}}{dt}. \tag{5.12}$$

The equations and boundary conditions can be nondimensionalized by letting $\mathbf{x} = a\mathbf{x}^*$, $\mathbf{u} = U_\infty \mathbf{u}^*$, $p = \frac{\mu U_\infty}{a} p^*$, and $\phi = \phi_0 \phi^*$, where the characteristic dimensions of length, voltage, and velocity are a the cylinder radius, ϕ_0 the applied electric voltage, and $U_\infty = \frac{\varepsilon \zeta_p}{\mu} \frac{\phi_0}{a}$ the electrophoretic velocity of the particle in an unbounded flow, respectively. These substitutions create the following governing equations for the fluid domain

$$\nabla^{*2}\phi^* = 0 \text{ in } \Omega \tag{5.13}$$

$$\nabla^* \cdot \mathbf{u}^* = 0 \text{ in } \Omega \tag{5.14}$$

$$\nabla^{*2}\mathbf{u}^* + \nabla^* p^* = 0 \text{ in } \Omega. \tag{5.15}$$

and boundary conditions

$$\phi^* = 1 \text{ on } \Gamma_{in},\ \phi^* = 0 \text{ on } \Gamma_{out} \tag{5.16}$$

$$\mathbf{n} \cdot \nabla^* \phi^* = 0 \text{ on } \Gamma_w \text{ and } \Gamma_p \tag{5.17}$$

$$\mathbf{u}^* = \gamma(\mathbf{I} - \mathbf{nn}) \cdot \nabla^* \phi^* \text{ on } \Gamma_w \tag{5.18}$$

$$\mathbf{u}^* = \mathbf{U}_p^* + \bar{\omega_p^*} \times (\mathbf{x}_p^* - \mathbf{X}_p^*) + (\mathbf{I} - \mathbf{nn}) \cdot \nabla^* \phi^* \text{ on } \Gamma_p \tag{5.19}$$

where γ is the ratio of zeta potential ratios of the channels wall and particle surface ($\gamma = \zeta_w/\zeta_p$). Similarly, nondimensionalizing the stress tensor, $\bar{\bar{\sigma}} = \frac{\mu U_\infty}{a}\bar{\bar{\sigma}}^*$, force, $\mathbf{F} = \mu U_\infty a \mathbf{F}^*$, and torque, $\mathbf{T} = \mu U_\infty a^2 \mathbf{T}^*$ yields the nondimensional equations of particle motion

$$\mathbf{F}^* = \int \bar{\bar{\sigma}}^* \cdot \mathbf{n} d\Gamma_p^* = m^* \frac{d\mathbf{U}_p^*}{dt^*} \tag{5.20}$$

$$\mathbf{T}^* = \int (\mathbf{x}_p^* - \mathbf{X}_p^*) \times (\bar{\bar{\sigma}}^* \cdot \mathbf{n}) d\Gamma_p^* = I^* \frac{d\omega_p^*}{dt^*} \tag{5.21}$$

where mass is nondimensionalized by $m = \frac{\mu a^2}{U_\infty} m^*$ and moment of inertia by $I = \frac{\mu a^4}{U_\infty} I^*$. Time is nondimensionalized as $t = \frac{a}{U_\infty} t^*$. All starred quantities are nondimensional.

5.4 Numerical Method

A commercial finite element package, Comsol Multiphysics (Comsol, Inc.; Burlington, MA) was used to solve the above set of nondimensional set of equations for

the fluid and particle motion. The computational domain is meshed with unstructured triangular elements, as shown in Fig. 5.1. The electric field and fluid motion are most complicated near the particle so the mesh is dense in the vicinity of the particle and grows less dense away from the particle. A direct solver is used to solve the system of equations at each time step. The ordinary differential equations (ODE's) for the particle motion, $\mathbf{F}^* = m^* \frac{d\mathbf{U}_p^*}{dt^*}$ and $\mathbf{T}^* = I^* \frac{d\bar{\omega}_p^*}{dt^*}$, are solved iteratively. It is possible to solve for the components of the stress tensor directly by differentiating the velocity solution. However to ensure greater accuracy, additional second order constraint equations are incorporated into the solution method. The additional constraints solve for the relevant boundary flux on the surface of the particle, which in a Navier Stokes problem are the stress tensor components. The flux is accurately calculated by finding the Lagrange multipliers for the constraint equation along with the general solution. The resulting values for the stress tensor components are second order accurate as opposed to the first order accuracy that would result from differentiating the velocity solution. The motion of the particle is monitored through an arbitrary Lagrangian-Eulerian (ALE) deformable mesh. As the particle translates and rotates the mesh deforms until the mesh quality degrades to a designated level at which point the motion is stopped. The deformed mesh is used to create new geometry and an undeformed mesh so the process can begin again. This method of remeshing allows for the motion of the particle to be monitored over a long period of time. Appendix C contains an example of the numerical code used to model the nanowire motion.

The solution method was compared to the results of (3) to determine the validity of the numerical model. In the study by Ye et al. (3), the translational and

rotational velocities were numerically computed for a sphere located at an eccentric position in a channel for a variety of gap widths (the distance between the particle and the nearest wall). The numerical model used in (3) solved for the steady-state horizontal and rotational velocities of the sphere for each gap width, assuming the vertical location was fixed (which would occur if a density difference existed between the particle and fluid). The nonsteady model described in Sec. 5.3 was run for an eccentrically-located sphere at the same gap widths as explored in (3). The vertical velocity was held at zero for all time and the motion of the sphere monitored until steady horizontal and rotational velocities were found. The results from the present nonsteady method are compared to the steady-state results of (3) in Fig. 5.2. The present nonsteady results properly capture the trend of the velocities

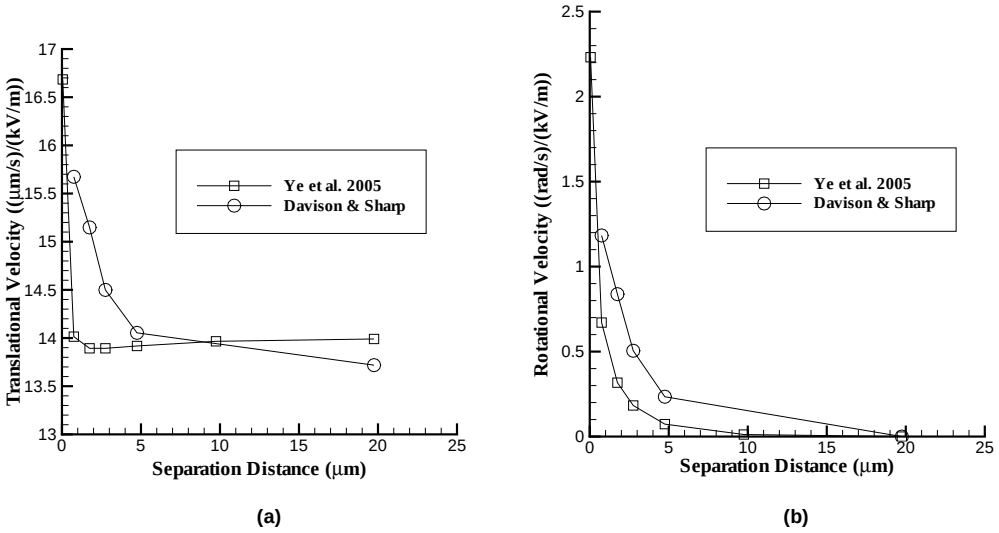

Figure 5.2: Comparison to (3) for eccentrically-positioned sphere in capillary channel. (a) Translational velocity versus separation distance. (b) Rotational velocity versus separation distance. Note: the velocity results have been normalized by electric field strength, but remain dimensional as indicated.

calculated in (3), but the method appears to overpredict the increase in transla-

tional and rotational velocity caused by the channel wall. Due to computational limitations, the nonsteady solution method used herein can only be run in two dimensions. Based on previous steady-state comparisons shown in 4.5, solving the steady-state equations in a three-dimensional geometry provided a better match in translational velocity to previously published results from other groups (6; 4) than by solving the steady-state equations in a two-dimensional geometry (0.5% for 3D versus 5% for 2D). The 2D steady-state results appeared to overpredict the effect of the channel walls 4.3. Here, the nonsteady results presented in Fig. 5.2 show that the translational velocity is overpredicted by 2% to 11% as compared to (3) over the range of gap widths investigated. If computational limitations were removed, it is expected that a 3D nonsteady solution method would improve the match of the results in the same way as for the steady-state results. Thus, the current 2D nonsteady results are expected to be valid for determining the motion of the particle in channels to within 10%.

5.5 Results and Discussion

The previous results from the steady-state simulations 4.5 (where the particle is held fixed) can provide insight into the translation and rotation of the particles seen in the current nonsteady simulations. Two primary trends were observed. First, the translational velocity of the particle is reduced as the angle, θ, of the particle is increased. This trend held whether the particle was located on the centerline of the channel or at an eccentric position (nearer one wall than the other). As the angle, θ, is increased, more of the particle surface is presented to the bulk fluid flow resulting in greater drag and a lower velocity. The second trend observed was that

when in an eccentric position, the velocity of the cylindrical particle is increased as the gap width is reduced. The velocity is increased because the electric field is concentrated by the particle's proximity to the channel wall, and the magnitude of the electric field is proportional to the velocity of the particle. When the particle is in an eccentric position, the increased viscous retardation from fluid drag in the small space is overcome by the increased electric field resulting in a greater velocity.

In the present study, nonsteady models were run for a cylindrical particle with a variety of starting angles (θ_0) through a long channel. The aspect ratio of the cylindrical particle and zeta potential ratio were held fixed at $l/a = 6$ and $\gamma = 0.375$ respectively. The radius of the channel was held fixed at $b^* = 5$. The particle was started from initial angles (θ_0) of 0°, 22.5°, 45°, 67.5°, and 90°. In all cases, the particle was started with the particle center located on the channel centerline. The horizontal (X-direction), vertical (Y-direction), and rotational (about the Z-axis) velocities were tracked as the particle moved through the channel.

The cases with the particle aligned ($\theta_0 = 0°$) or perpendicular ($\theta_0 = 90°$) to the channel axis demonstrated that these are stable orientations. The particles translated with constant horizontal velocity and zero vertical and rotational velocity. In order to conserve computational resources these models were run for only 20 nondimensional time units, during which it was clearly shown the motion was steady and unchanging. The results for these two cases are included in Figs. 5.4, 5.5, and 5.6 for motion in the horizontal, vertical, and rotational directions respectively. It is expected that $\theta_0 = 90°$ is a marginally stable state and would be susceptible to small perturbations, absent in a numerical simulation, that

would result in non-steady behavior.

Particles with other initial angles ($\theta_0 = 22.5°$, $45°$, and $67.5°$) translated horizontally through the channel while also translating vertically and rotating. In order to more fully describe the motion of these cases, the models were run for at least 300 nondimensional time units. Over this time period, the cylindrical particle translated through a channel that had a length of $L^* = 210$ and a radius, $b^* = 5$. A sequence of images of the motion for these three cases is presented in Fig. 5.3. Each image of the position of the particle is separated by 20 nondimensional time

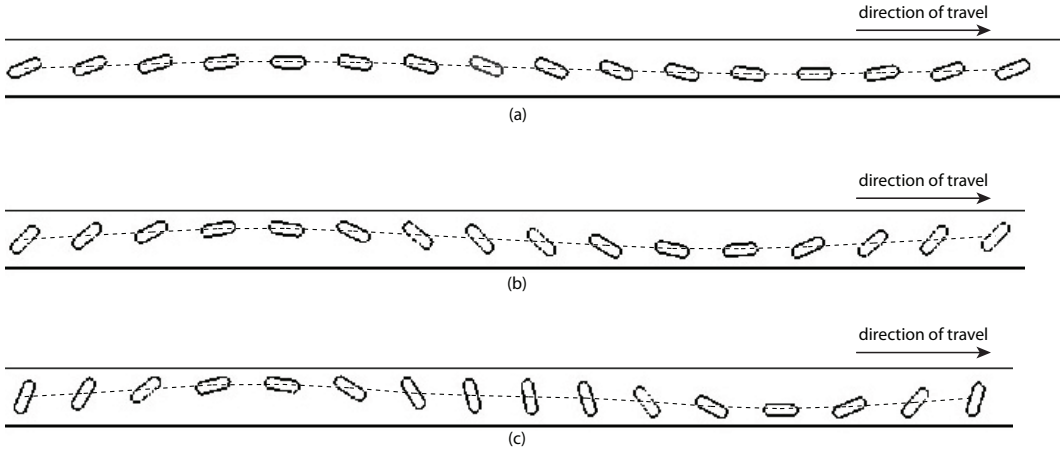

Figure 5.3: Sequence of images of rotation and translation of angled cylinder in channel with radius, b^*, of five. Images presented every 20 nondimensional time units over 300 nondimensional time units. Particle trajectory illustrated by dashed lines through particle center. (a) Particle initially at $\theta_0 = 22.5°$. (b) Particle initially at $\theta_0 = 45°$. (c) Particle initially at $\theta_0 = 67.5°$. Data from 2D numerical models.

units.

Over the course of the observed motion (limited by the length of the channel selected and computational resources), the cylindrical particles translate horizontally while experiencing oscillatory behavior in vertical and rotational velocity. Each particle moves through one period during the motion observed. The parti-

cle, initially in the center of channel, translates upward while rotating towards an aligned ($\theta_0 = 0°$) orientation which it reaches at the end of its upward motion. The particle then translates downward while rotating away from the wall. It again reaches an aligned orientation when it is nearest to the lower wall. The particle then rotates and translates away from the lower wall and reaches, roughly, the center of the channel, completing one period, when the particle reaches the end of the channel.

5.5.1 X-Direction Motion

The details of the particle motion in the X-direction are shown in Fig. 5.4. The

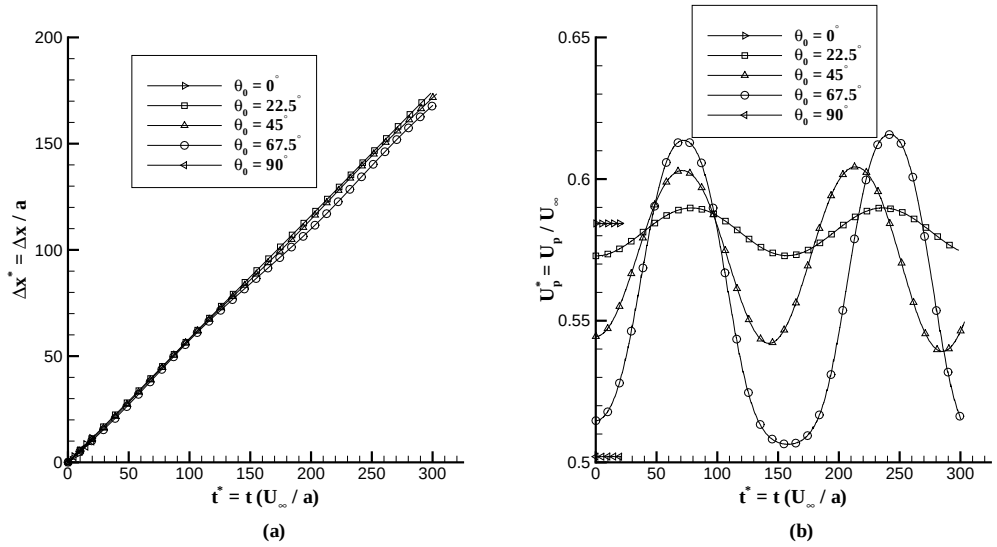

Figure 5.4: Description of cylindrical particle motion in the X-direction (horizontal) for particles started at $\theta_0 = 0°$, $22.5°$, $45°$, $67.5°$, and $90°$. (a) Displacement, Δx^*, versus time, t^*. (b) Translational velocity, ${U_p}^*$, versus time, t^*. All starred quantities are non-dimensional. For clarity, only every 100^{th} data point for $\theta_0 = 22.5°$, $45°$, and $67.5°$ and every 50^{th} data point for $\theta_0 = 0°$ and $90°$ has been indicated. Data from 2D numerical models.

displacements in Fig. 5.4a demonstrate that the motion of the particle is largely

the same regardless of the starting angle. At large times it is possible to see slight separations between the curves for the non-equilibrium orientations. The particle that begins at $\theta_0 = 22.5°$ translates the farthest, over the time range studied, followed by $\theta_0 = 45°$, and then $\theta_0 = 67.5°$.

Fig. 5.4b shows the horizontal velocity for all the initial angles. The curves for $\theta_0 = 0°$ and $90°$ indicate that their motion is steady. The curves for the other three cases clearly demonstrate oscillatory behavior. For all cases, the particle begins in the center of the channel where it has the greatest angle with respect to the channel centerline. The particle at a larger angle will translate more slowly explaining why the particles have the slowest velocity when their centers are located at the centerline of the channel. As the particles move away from the center of the channel, they reduce in angle and approach the channel wall, both conditions that cause an increase in the velocity of the particle. Hence, the maximum velocity occurs when the particle is aligned with the channel centerline and near the wall. The differences present in the three curves are the result of the initial particle angle. When θ_0 begins at $22.5°$, the low angle results in a larger initial horizontal velocity but this particle does not have to translate as far vertically before it rotates to an aligned position. Since it does not get as near to the wall as other cases, its maximum horizontal velocity is lower. The opposite situation occurs for $\theta = 67.5°$ where the larger initial angle results in a lower initial velocity. But since the particle is closer to the wall when it reaches the aligned state, this case demonstrates the largest horizontal velocity.

5.5.2 Y-Direction Motion

Figs. 5.5a and b detail the Y-direction (vertical) displacement and velocity of a particle for multiple initial angles. The velocities and displacements for $\theta_0 = 0°$

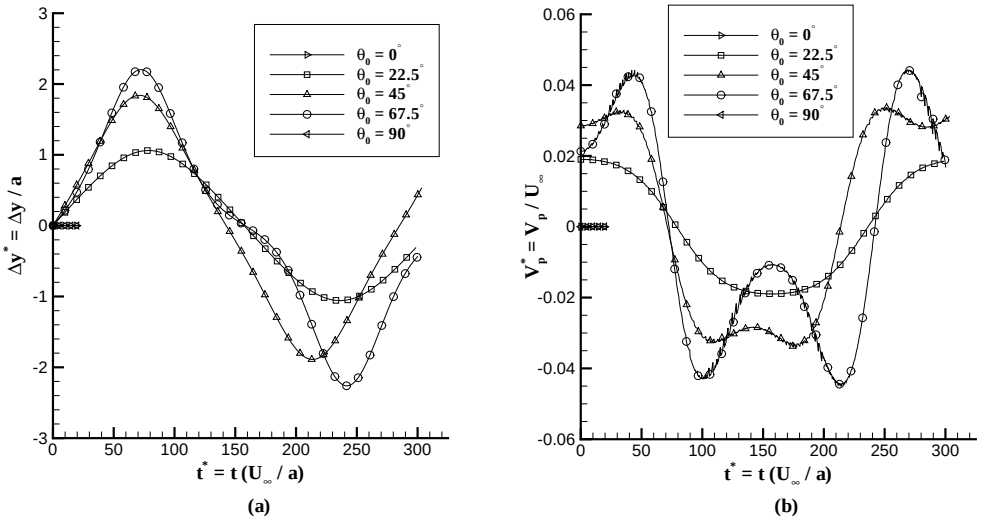

Figure 5.5: Description of cylindrical particle motion in the Y-direction (vertical) for particles started at $\theta_0 = 0°$, $22.5°$, $45°$, $67.5°$, and $90°$. (a) Displacement, Δy^*, versus time, t^*. (b) Translational velocity, $V_p{}^*$, versus time, t^*. All starred quantities are non-dimensional. For clarity, only every 100^{th} data point for $\theta_0 = 22.5°$, $45°$, and $67.5°$ and every 50^{th} data point for $\theta_0 = 0°$ and $90°$ has been indicated. Data from 2D numerical models.

and 90° are zero for all times considered. Both plots demonstrate the oscillatory behavior of the other three cases. Fig. 5.5a shows that the larger the starting angle, the closer the particle gets to the wall, resulting in the larger horizontal velocity noted above. The velocities in Fig. 5.5b indicate that the larger the angle, the larger the vertical velocity. For $\theta_0 = 22.5°$, the smooth curve reveals that the particle translates vertically the fastest when at the channel centerline. However, the curves for $\theta_0 = 45°$ and 67.5° show that for greater initial angles there are other effects that increase the vertical velocity resulting in the "saddle" shape seen in

the velocity curves. From the previous steady-state results 4.5, it is known that, for a particle held fixed at the centerline, the maximum vertical force occurs when the particle is at $\theta = 45°$. The points on the velocity curve for $\theta_0 = 67.5°$ where the vertical velocity is a maximum correspond to times when the particle is rotating through $\theta = 45°$. This explanation can not fully explain the curve's shape, as the case for $\theta_0 = 45°$ demonstrates the same "saddle" shape, but maximum vertical velocity occurs when the particle is at $\theta < 45°$. This indicates that the vertical velocity is enhanced at angles larger than 22.5° at vertical locations slightly above or below the channel centerline. It is suggested that the small "saddle" behavior seen in the $\theta_0 = 45°$ case is the result of the particle being offset vertically from the centerline and this effect combines with the velocity increase at $\theta = 45°$ to produce the large "saddle" curve seen for $\theta_0 = 67.5°$.

5.5.3 Rotational Motion

The angle of each particle over time and rotational velocity are included in Fig. 5.6. Once again the constant curves in angular position and rotational velocity demonstrate that the particles at $\theta_0 = 0°$ and 90° are at equilibrium and do not rotate. The angular position plot in Fig. 5.6a simply shows that the particles undergo one period of rotation over the time period of interest. The rotational velocities in Fig. 5.6b demonstrate similar behavior to that seen in the vertical velocity plot. The curve for $\theta_0 = 22.5°$ is smooth and demonstrates a maxima when the particle is nearest to the wall. The curve for $\theta_0 = 45°$ shows a broadening of the maxima, while the curve of $\theta_0 = 67.5°$ displays a "saddle" at the point of nearest approach to the wall. For the case of $\theta_0 = 22.5°$, the particle is the furthest from the wall at

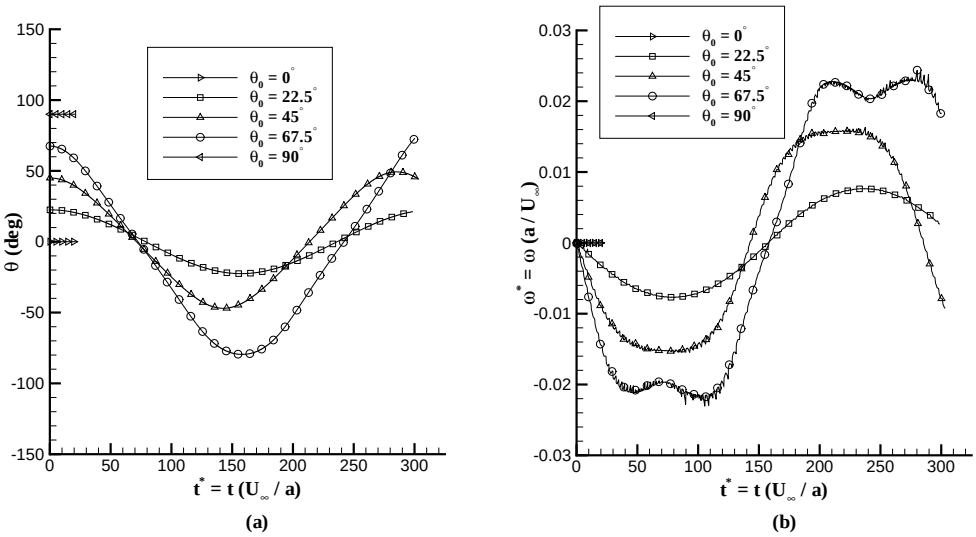

Figure 5.6: Description of cylindrical particle motion in the angular direction for particles started at $\theta_0 = 0°$, $22.5°$, $45°$, $67.5°$, and $90°$. (a) Particle angle, θ, versus time, t^*. (b) Rotational velocity, ${\omega_p}^*$, versus time, t^*. All starred quantities are non-dimensional. For clarity, only every 100^{th} data point for $\theta_0 = 22.5°$, $45°$, and $67.5°$ and every 50^{th} data point for $\theta_0 = 0°$ and $90°$ has been indicated. Data from 2D numerical models.

its aligned position and so the asymmetry is greatest at this point resulting in the maximum rotational velocity. When the particle approaches the wall more closely, $\theta_0 = 67.5°$, the asymmetry from the small particle angle contributes to the torque on the particle resulting in a greater rotational velocity just before and after the aligned position, creating the "saddle" shape in the curve.

5.6 Summary

This chapter considers the nonsteady translation and rotation of cylindrical particles through a narrow channel to determine the effect of initial particle orientation with the goal of ascertaining position and orientation for device integration. The

motion of the particles was modeled with a nonsteady numerical method using a deformable mesh to track the particle position. The velocities and displacements of the particles were tracked for initial orientations of $\theta_0 = 0°$, 22.5°, 45°, 67.5°, and 90°. For the cases where the particle begins in an aligned ($\theta_0 = 0°$) or perpendicular ($\theta_0 = 90°$) position with respect to the channel axis, the particle translates horizontally in a steady-state condition with no vertical or rotational velocity. In the cases of $\theta_0 = 22.5°$, 45°, and 67.5° the particles move in an oscillatory manner. The particles initially translate vertically upward and reduce their angle to the channel centerline before reaching $\theta = 0°$ at their nearest approach to the wall. The particles then rotate and translate away from the wall and approach the opposite wall in the same way. Over the course of the current numerical models the particles complete one period of motion. The larger the initial angle, the greater the difference between minimum and maximum translational or rotational velocity and the larger the vertical displacement. It is evident that the period of the particle with $\theta_0 = 22.5°$ or 67.5° is longer than that of $\theta_0 = 45°$ and that the angle the particle makes with the centerline decreases for $\theta_0 = 22.5°$ and increases for $\theta_0 = 67.5°$. With infinite computational time and power a study of many periods of motion could discern whether or not these cases are trending toward a steady, equilibrium motion. However, the practicality of these results would be negligible. The channel lengths in the current investigation are longer than physically practical in a microfluidic system.

The general trends observed here corroborate earlier conclusions drawn from a steady-state model 4.5 (particle held fixed). Namely, a nearby boundary serves to increase or decrease a particle's electrophoretic velocity in response to the (often

competing) effects of viscous retardation and electrical field concentration in the gap. While the current nonsteady simulations have considered only the effect of initial orientation, such models may be useful in the future for considering how individual particles with different properties (e.g. zeta potential, aspect ratio, etc.) in a dilute suspension would respond under the same applied electric field. Furthermore, the present results show that, under certain conditions, the particle does not quickly approach a state of equilibrium. Thus, additional measures may be appropriate in order to most effectively control the trajectory of individual particles for use in practical microfluidic systems.

Chapter 6

Nonsteady Numerical Models through a 90° Corner

6.1 Introduction

Given the commonplace nature of geometric features such as corners and turns in microfluidic systems, the two goals of the present chapter are: 1) to determine the fundamental effect of a 90° corner on the motion of an individual cylindrical particle under standard DC electrophoresis, and 2) to determine whether or not a geometric feature, in this case a corner, within a microfluidic system may be used as a passive control element as part of a larger system.

In an electrophoretic system, the ionic concentration of the suspending medium has a large effect on the properties of the system since it controls the thickness of the electrical double layer. A system with thin electrical double layers would be represented by a value of $\kappa a \gg 1$ as is the case in this chapter due to the prevalence of practical situations that meet this criteria. Previous work with corners and

junctions in microfluidic systems have largely focused on fluid-only systems (42; 43). Thamida and Chang (44) examined the aggregation of small ($< 1\%$ of the channel width) colloidal particles at the corner of a microfluidic junction. More pertinently, Ye and Li (41) studied the motion of a large spherical particle (40% of the channel width) as it moved electrophoretically through a 90° corner as part of a T-junction. However, since the particle was a sphere, no emphasis was placed on the rotation of the particle as it passed through the corner region. For the motion of a cylindrical particle, both the trajectory of the particle center and the angle of the particle are critical to describing the electrophoretic motion. The effect of various system parameters on these two motion components is categorized as having minimal or significant impact and is detailed herein.

6.2 Problem Definition

The current investigation seeks to determine the trajectory of a cylindrical particle as it moves through a 90° corner under the influence of electrophoresis. Figure 6.1a shows the modeled two-dimensional system in a typical initial position as well as geometrical descriptors of the problem. The channel consists of two sections with a length of L and width b joined into a 90° corner, with the inlet, Γ_{in}, and outlet, Γ_{out}, leading to reservoirs open to the atmosphere (no pressure gradient through the channel). A small radius ($a/2$) is applied to the corners where the channel sections meet in order to eliminate the numerical singularity that would exist at a sharp corner. The channel, outside of the particle and thin electrical double layers on the surfaces, is filled with an incompressible, Newtonian fluid which makes up the computational domain, Ω. The particle has a total length of l, with

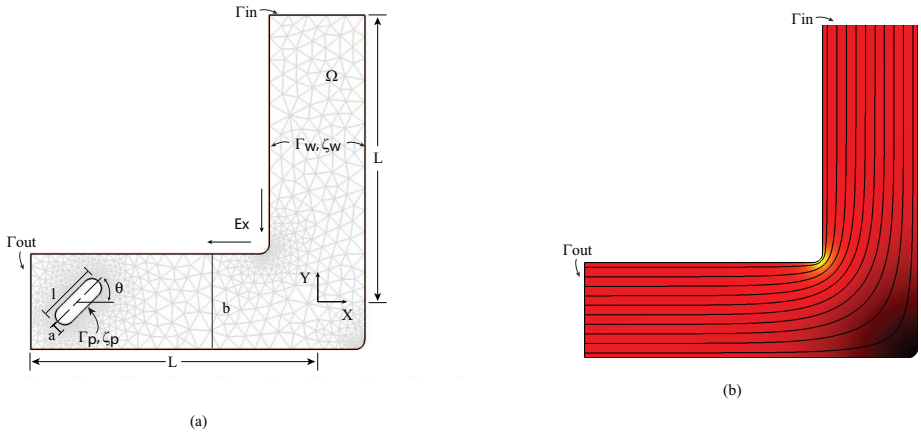

Figure 6.1: (a) Diagram of cylindrical particle at initial position in channel with relevant dimensions and variables. The origin of the coordinate system used lies at the intersection of the channel centerlines and is indicated by the X, Y axes in the figure. Unstructured triangular mesh of computational domain included to illustrate increase in mesh density around the particle. (b) Diagram of the distribution of electric field, with electric field lines, present in the channel without a particle present. Shading indicates strength of the electric field, with lighter colors (e.g. at the inner corner) designating a stronger field.

hemispherical ends of radius a. The boundary of the particle and electrical double layer is designated by Γ_p, while the boundary of the channel walls is denoted by Γ_w. The electrical field, E_x, is applied from the inlet to the outlet causing the fluid flow to proceed in the same direction due to the uniform and negative zeta potential, ζ_w, of the channel walls. The distribution of electric field in the channel, without the presence of a particle, is shown in Fig. 6.1b.

The Reynolds number of the system can be calculated based on the particle motion and length scale yielding a value of 4×10^{-5} or the fluid velocity and channel width which gives 2×10^{-4}. The Stokes equations are used to model the fluid motion due to the low Reynolds number of the modeled system. Since the particle has a uniform zeta potential, ζ_p, that is greater in magnitude than the channel

walls ($\zeta_w/\zeta_p < 1$) the particle will move from Γ_{out} to Γ_{in}. The importance of Brownian motion can be estimated by a Peclet number defined as the ratio between the electrophoretic velocity and the translational Brownian diffusion, $Pe = \frac{aU_{ep}}{D_{Brownian}}$ (1; 45), where a is the particle radius. For simplicity in calculating the Peclet number, the cylindrical particle is replaced by a sphere with an equivalent volume which yields a Peclet number of Pe = 460. This indicates that Brownian translation is much less significant than the electrophoretic motion and so Brownian motion is neglected in the following analysis. Within the current system, various parameters are theorized to have an effect on the motion of the cylindrical particle. The zeta potential ratio (γ), channel width (b), particle aspect ratio (l/a), initial particle angle (θ_0), and initial vertical position in the channel (Y_0) will be varied to determine the effect on the electrophoretic motion of the cylindrical particle.

6.3 Governing Equations and Numerical Method

The trajectory of the cylindrical particle is determined by simultaneously solving the equations for the electrical field, fluid flow, and particle motion. The equations presented are formulated and nondimensionalized as in Sec. ref4eqns.

The system of equations is solved using a commercial finite element package, Comsol Multiphysics (Comsol, Inc.; Burlington, MA). The current results are based upon two dimensional models, representing the central plane of either a cylindrical or square channel, due to limitations of computer resources. A previous comparison between two and three dimensional results showed that the three dimensional results were more accurate (0.5% vs. 4%) in comparison to other published results (Sec. 4.4.2). However the two dimensional results demonstrated

the same trends in the motion of the particle and so are used herein with confidence that the behavior seen is a good representation of what would be expected in three dimensions. The computational domain, Ω, is meshed with unstructured triangles. As seen in Fig. 6.1a, the mesh density is increased around the particle due to the more complicated motion in that region. The particle is initially at rest, though the electric field and subsequent motion are established instantaneously once the model begins. At each time step, the system of equations for the electric field and fluid motion is solved directly. An iteration scheme is used to solve the ordinary differential equations for the particle motion, the forces and torques present at the particle surface. Additional 2^{nd} order elements are added to the variable set and used to solve for the particle surface stress tensor. These additional variables are used instead of differentiating the velocity components of the solution in order to increase the accuracy of the solution. Once the particle motion has been solved for, the particle is moved by deforming the mesh according to an arbitrary Langrangian-Eulerian (ALE) scheme. After the mesh deforms to a designated point of decreased quality, a new geometry is created on which a new mesh is applied and the process repeated to model large particle motions.

6.4 Results and Discussion

As indicated earlier, the equation system is nondimensionalized and as such the results are presented nondimensionally. The constants are chosen to model a system whose dimensions are based upon a particle radius, $a = 1.5$ μm and aqueous fluid properties. The base particle has an aspect ratio of $l/a = 6$ and moves through a channel with a width of $b/a = 10$ and horizontal and vertical segments of L/a

= 25. To determine the effect of the corner on the electrophoretic motion of the particle, nonsteady simulations were run exploring the effect of varying the zeta potential ratio, channel width, particle aspect ratio, initial angle of the particle, and initial vertical position of the particle on the motion of the particle. Typical results include a trajectory plot of the position of the center of the particle graphed against nondimesional X^* and Y* coordinates ($X^* = X/a$, $Y^* = Y/a$). The angle of the particle is presented against the nondimensional time elapsed. The angle is given in degrees for ease of interpretation, but is calculated in nondimensional radians. The results obtained are assembled based on the impact of the parameter on the particle motion.

6.4.1 Parameters with Minimal Impact on Particle Motion

6.4.1.1 Effect of Zeta Potential Ratio

The zeta potential of the channel walls was varied to produce cases with $\gamma = 0.375$ and 0.75. The aspect ratio of the particle was held at $l/a = 6$, the channel width was $b = 10$, and the initial angle of the particle was $\theta_0 = 0°$. The results of these tests are presented in Fig. 6.2. The trajectories for the two cases are presented in Fig. 6.2a, and indicate the cylindrical particle travels an identical path for the zeta potential ratios tested. Likewise, Fig. 6.2b includes the angle of the two particles against time and demonstrates the two cases have the same angular behavior to within $\pm 1°$, but over two different time scales. This behavior is also clear in the trajectories plot (Fig. 6.2a), because each successive data symbol is given for five nondimensional time units of motion. Changing the zeta potential ratio (γ) of the system changes the ratio of the fluid and particle velocities, which are in opposite

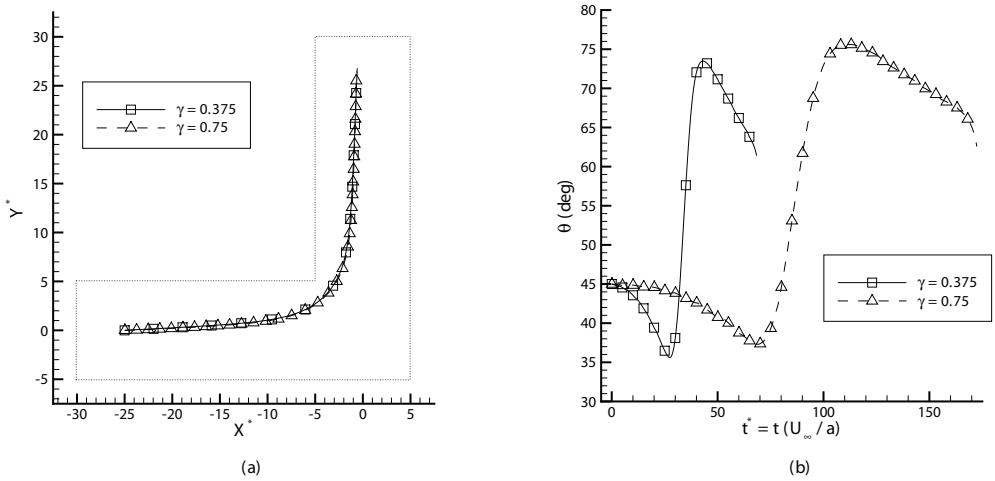

Figure 6.2: Effect of the zeta potential ratio, γ, on the motion of a cylindrical particle with $l/a = 6$, $b = 10$, and $\theta_0 = 45°$. (a) Trajectories of the particles with zeta potential ratios of $\gamma = 0.375$ and 0.75. The channel boundaries are included for reference. Data symbols are given for every 5 nondimensional units of time. (b) Change in the angle (degrees) of the particle as a function of time. Data from 2D numerical models.

directions for $0 < \gamma < 1$. By increasing γ, the fluid velocity was increased in the direction opposite to the particle motion resulting in a lower particle velocity. The change in γ did not alter the effect of the corner geometry on the cylindrical particle as the only differentiating characteristic is the time scale of the motion.

6.4.1.2 Effect of Channel Width

A particle with an aspect ratio of $l/a = 6$, zeta potential ratio of $\gamma = 0.375$, and initial angle of $\theta_0 = 0°$ was modeled in channels with widths of $b = 6$, 10, and 15. Figure 6.3 contains the trajectories and angular time histories of these cases. The particles are shown, in Fig. 6.3a, to travel the same path in the horizontal and vertical sections of the channels, with the only variations in trajectories in the corner region. The physical shape of the channel leads to this result, as the channel

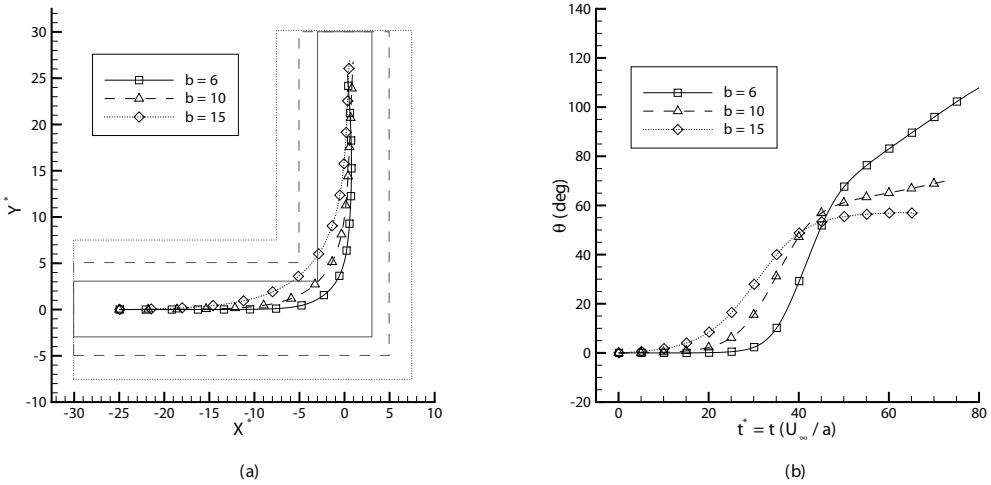

Figure 6.3: Effect of the channel width on the motion of a cylindrical particle with $l/a = 6$, $\gamma = 0.375$, and $\theta_0 = 0°$. (a) Trajectories of the particles for channels with widths of b = 6, 10, and 15 units. The channel boundaries corresponding to each data curve are included in the matching line type. Data symbols are given for every 5 nondimensional units of time. (b) Change in the angle (degrees) of the particle as a function of time. Data from 2D numerical models.

geometries sketched in Fig. 6.3a indicate the larger the channel width the larger the radius of the trajectory in the corner. Another result present in the trajectory plot is that the particle translates slower in a channel with smaller width.

The influence of boundaries on the translation of particles is a balance of two competing effects, one which increases the particle and fluid velocities and the other which decreases particle velocity. Specifically, for smaller separations the electric field is increased between an insulating particle and insulating walls resulting in increased particle and fluid velocities, and the hydrodynamic drag caused by the wall on the particle is also increased which decreases particle velocity. In this case, the increase in drag is dominant resulting in slower translation of the particle as the channel width is decreased. This change in translational velocity is indicated

by the symbols in the trajectory plot which are five nondimensional time units apart, and Fig. 6.3b where the particle angle is plotted against nondimensional time. As expected, the angle of the particle increases substantially as the particle passes through the corner region, this increase occurs earlier the larger the channel width. Essentially, as is shown in Fig. 6.3a, the particle cuts across the corner (and rotates) sooner because the corner occurs at a more negative value of X^* in a larger channel. Within the system modeled, the angle of the particle reaches a larger value as the channel width is decreased. As the particle exits the corner, its angle is around 50° to 60°, and the ends of the cylinder interact with the wall in differing amounts depending on the channel width. As the channel width is reduced, the interaction is increased leading to greater hydrodynamic drag on the ends which yields a greater torque on the particle. This trend is evident in Fig. 6.3b where the particles in smaller channels rotate to angles closer to 90° (vertical) than the larger channels.

6.4.1.3 Effect of Aspect Ratio

To determine the effect of the particle aspect ratio, the length (l) of the particle was varied to produce aspect ratios of $l/a = 2$ (sphere), 4, 6, and 8. These particles moved through a channel with a width of $b = 10$, a zeta potential ratio of $\gamma = 0.375$, and initial angle of $\theta_0 = 0°$. The trajectories and angular motion are presented in Fig. 6.4. The trajectories show that the particles travel nearly the same path through the channel. In the vertical section, there is some differentiation among the paths with longer particles trending toward the right hand wall ($+X^*$ direction), but the change in position is small, less than two particle radii. The trajectory plot

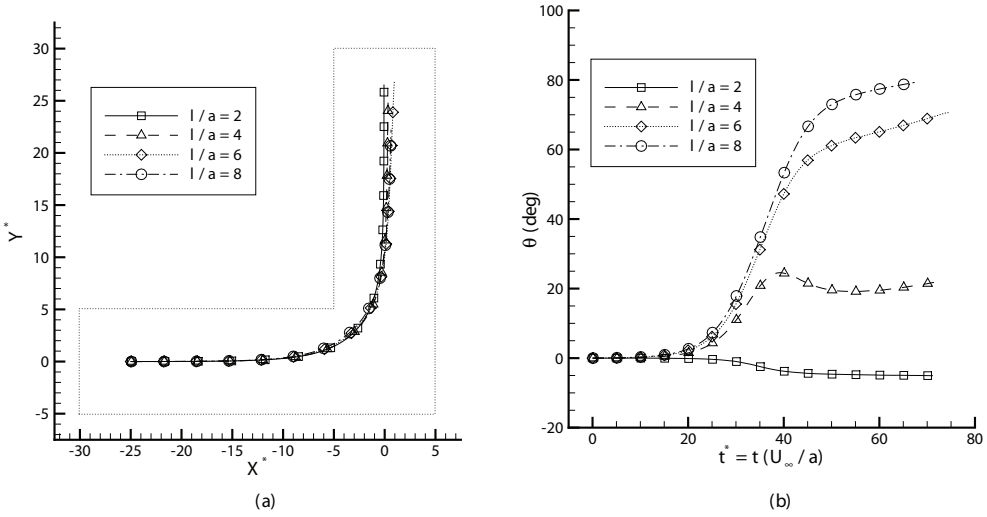

Figure 6.4: Effect of the aspect ratio of a cylindrical particle with $b = 10$, $\gamma = 0.375$, and $\theta_0 = 0°$. (a) Trajectories of particles with aspect ratios of $l/a = 2$ (sphere), 4, 6, and 8. The channel boundaries are included for reference. Data symbols are given for every 5 nondimensional units of time. (b) Change in the angle (degrees) of the particle as a function of time. Data from 2D numerical models.

also indicates that longer particles translate at a reduced velocity, due to increased fluid drag along their larger surface areas. The motion of the spherical case ($l/a = 2$) is substantially similar to the trajectory of a sphere in a T-junction under an equivalent electric field presented in Ye (41). In the angle plot, Fig. 6.4b, the spherical particle only experiences torque, and therefore a change in angle, in the corner region where the electric and fluid fields are not uniform around the sphere. For the remainder of the cases, the ends of longer particles are closer to the channel walls which leads to increased torque on the particle and leads to the larger angles indicated.

6.4.2 Parameters of Significant Impact on Particle Motion

6.4.2.1 Effect of Initial Angle

The initial angle (to the horizontal) of the particle was varied from $\theta_0 = 90°$ to -75°, which covers the complete range of angles since $\theta = 90° = -90°$, while holding the particle aspect ratio of $l/a = 6$, channel width of $b = 10$, and zeta potential ratio of $\gamma = 0.375$ fixed. For clarity, the results of selected values of initial angle are presented in Fig. 6.5. The trajectory plot in Fig. 6.5a demonstrates

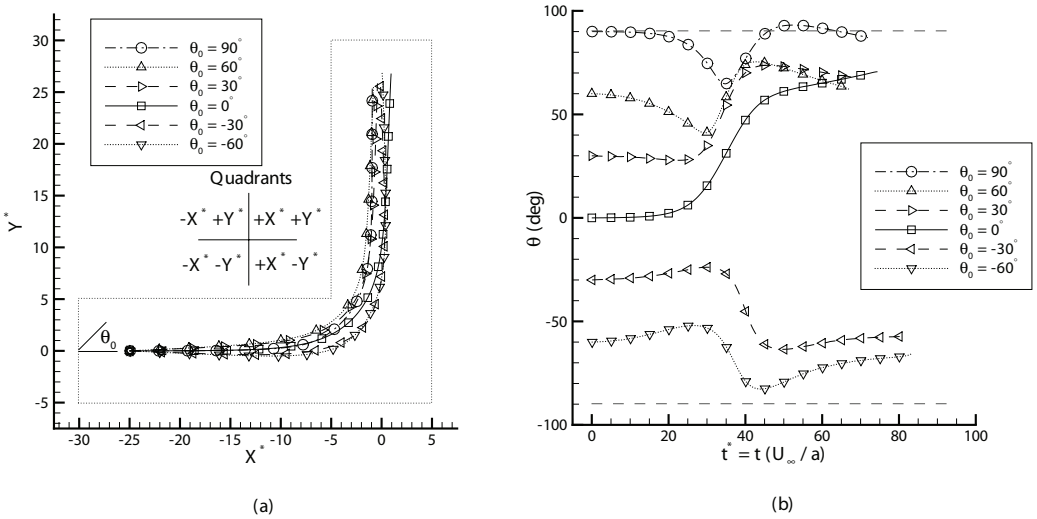

Figure 6.5: Effect of the initial angle of a cylindrical particle with $l/a = 6$, $b = 10$, and $\gamma = 0.375$. (a) Trajectories of particles with initial angles of $\theta_0 = 90°$, 60°, 30°, 0°, -30°, and -60°. The channel boundaries are included for reference. Data symbols are given for every 5 nondimensional units of time. (b) Change in the angle (degrees) of the particle as a function of time. Dashed lines indicate $\theta = 90°$ and -90° which is when a particle would be aligned with the vertical centerline. Data from 2D numerical models.

that there is a difference in trajectory as a function of initial angle. The cases for $\theta_0 = 0°$ and 90° translate down the center of the horizontal section of the channel, which follows from symmetry of the electric and fluid fields. The cases

with positive initial angles translate upwards in the Y^* direction, while the negative initial angle cases translate downwards in the -Y^* direction. This correlates to earlier work on translation in a straight channel in which the flow around an angled particle causes it to translate in the direction its leading edge is translating (Sec. 5.5). This previous observation also explains the trajectory of the particles in the vertical section. The two cases with negative initial angle move from right to left (-X^* direction) across the vertical section. After the corner, the leading edge of these particles is oriented toward the -X^* +Y^* quadrant, leading to an observed translation in the -X^* +Y^* direction. Similarly, the positive initial angle particles are oriented toward the +X^* +Y^* quadrant (after the corner), but at an angle closer to vertical so the motion in the +X^* direction is not as pronounced. The trajectory plot also indicates that the particle moves slower as its angle is increased as a result of the increased drag from a larger area exposed to the flow (Sec. 4.5.1.3, 5.5).

The angular motion of the particle is shown in Fig. 6.5b. It is clear that there exist two distinct rotational motions through the corner region. With an initial angle of $\theta_0 = 0^\circ$ to 60° the particle rotates toward a larger value of θ as the particle moves through the corner, and all the cases end at a value of θ around 70°. The cases of θ_0 = -30° and -60° pass through the corner while rotating to a more negative value of θ and finish around -60°. The corner is influencing all the cases to trend toward an alignment with the vertical channel, an angle of 90° or -90°.

To clarify, the absolute value of the angle the particle makes to the vertical direction, θ' is plotted in Fig. 6.6a. The value of θ' is found by defining $\theta' = 90^\circ - |\theta|$. The plot of θ' demonstrates that the initial angle to the vertical is reduced by

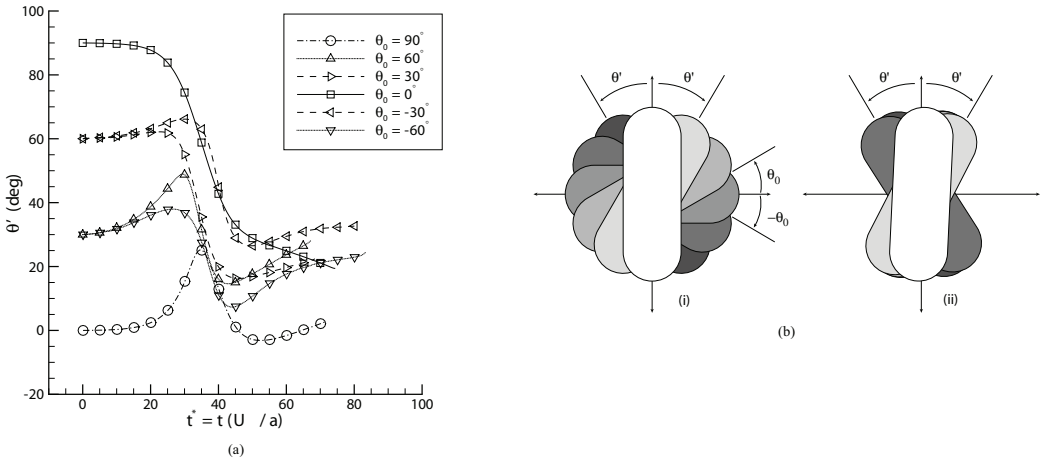

Figure 6.6: Description of the change in angle of cylindrical particles after passing through a 90° corner. (a) Change in absolute value of angle (degrees) with respect to the vertical direction, θ' = 90 - $|\theta|$. (b) Diagrams of the initial and final angular positions of the cylindrical particles. The shading designates a specific particle's initial and final angular positions. Data from 2D numerical models.

passing the particles around the corner. The initial spread of 90° is reduced to 29.9° at the end of the current computational domain. The change in θ' is presented visually in Fig. 6.6b, where the initial angular positions of the particle cases are shown in diagram (i) and the final positions in diagram (ii). Each particle retains its shading from (i) to (ii) in Fig. 6.6b. The reduction in angle is very promising as it demonstrates a corner geometry could be a possible means to passively exert control over the particle orientation. However, this positive control element comes with restrictions. The angle reduction neither continues to improve nor remains constant if the motion is allowed to continue in a straight channel. The previous chapter has shown that an angled cylindrical particle moving electrophoretically through a straight channel will oscillate in angle and position perpendicular to the channel axis. This restricts the positive aspects of this control element to near

the channel lengths investigated herein, namely around 25 particle radii from the corner.

6.4.2.2 Characteristic Motion through Corner

In Fig. 6.5b, there seems to be two distinct classes of motion through the corner among the *selected* cases for that plot. When *all cases* are examined, it is clear that there are actually three distinct classes of angular motion through the corner, the two classes noted from Fig. 6.5b and a third borderline class. Figure 6.7a shows the angular motion of every case of initial angle modeled, and the division into the three classes of motion. The motion designated as Class I consists of particles with initial angles from θ_0 = -10° to 90° which tend to increase in angle by moving through the corner. These particles have final angles of θ_f = 60° to 90° (to the horizontal) at the end of the modeled motion. In Fig 6.7b, the Class I motion is demonstrated by a series of images from the motion of the θ_0 = 45° case. Class II consists of particles with initial angles from θ_0 = -20° to -75° that tend toward more negative angles through the corner. Final angles of θ_f = -40° to -80° are seen in these cases. A series of images from the θ_0 = -45° case illustrate this motion in Fig. 6.7b. Finally, the θ_0 = -15° motion is the borderline case labeled as Class III and depicted in the final series of images in Fig. 6.7b.

The behavior seen is a result of the electric field present in the corner of the channel. The curve of the electric field lines around the corner causes a region of higher electric field near the inner corner, with a corresponding drop in electric field near the outer corner, as shown in Fig. 6.1b. In electrokinetic flow, the magnitude of the electric field determines the magnitude of the velocity. As a

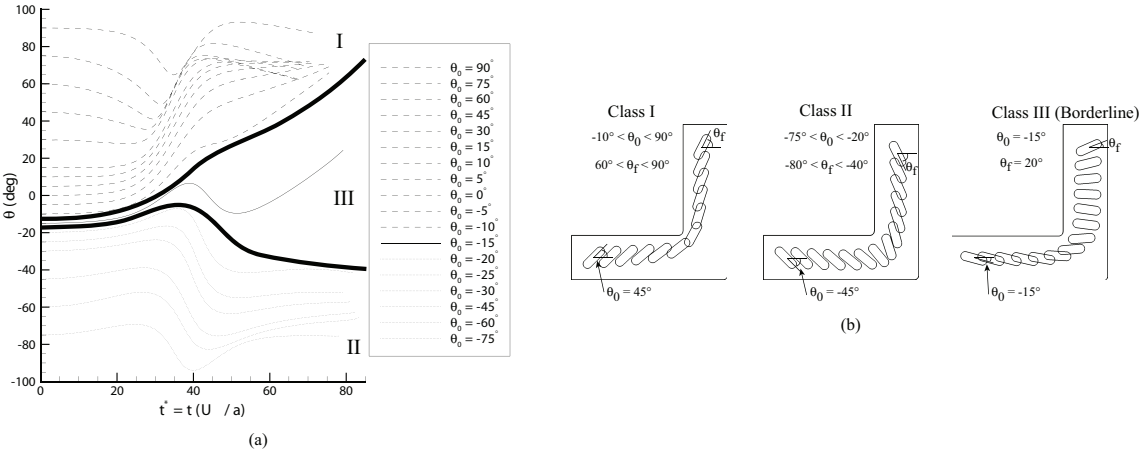

Figure 6.7: Description of the three characteristic motions of a cylindrical particle through a 90° corner. (a) Change in the angle (degrees) of the particles as a function of time. Particles with initial angles from θ_0 = -10° to 90° make up the type of motion designated as Class I. Particles with initial angles from θ_0 = -20° to -75° make up the type of motion designated as Class II. The bordering case is that of a particle with an initial angle of θ_0 = -15° and designated as Class III. (b) Representative diagrams showing the three classes of motions of a cylindrical particle as it travels around a 90° corner. The particle is initially located in the center of the channel, five nondimensional units from Γ_{out} at angles of 45°, -45°, and -15° to the horizontal. An image is presented at the initial location and then once every six nondimensional time units until the particle center reaches five nondimensional units from Γ_{in}. Data from 2D numerical models.

particle undergoing Class I motion approaches the corner, its positive angle nearly aligns the particle with the electric fields lines resulting in the entire particle being moved around the corner following the electric field lines. This is contrasted by Class II motion where the negative angle of the particle means that the trailing edge is in the higher electric field and is made to move faster than the other end, rotating the particle to nearly -90° and becoming the new leading edge. Class III motion acts similarly, where the trailing edge is accelerated through the corner, but only to the point where the particle is nearly horizontal upon exit from the

corner.

6.4.2.3 Effect of Initial Position

The initial vertical position in the channel was varied by one nondimensional unit up and down to determine the effect on the motion of a particle with an aspect ratio of $l/a = 6$, channel width of $b = 10$, zeta potential ratio of $\gamma = 0.375$, and initial angle of $\theta_0 = 0°$. The trajectory and angle plots are presented in Fig. 6.8. Due to

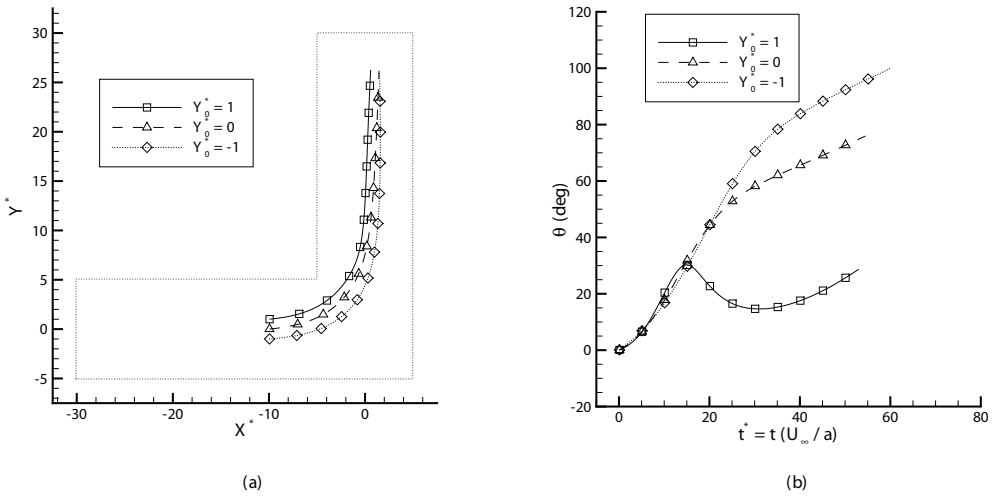

Figure 6.8: Effect of the initial position of a cylindrical particle with $l/a = 6$, $b = 10$, $\gamma = 0.375$, and $\theta_0 = 0°$. (a) Trajectories of particles with initial positions of $Y_0{}^* =$ 1, 0, and -1 units. Particles started from $X_0{}^* =$ -10 instead of $X_0{}^* =$ -25 due to increased computational difficulties with particles passing closer to the corner. The channel boundaries are included for reference. Data symbols are given for every 5 nondimensional units of time. (b) Change in the angle (degrees) of the particle as a function of time.

the added computational complexity of having a particle closer to the walls, the particles were started from a position of $X_0{}^* =$ -10 instead of $X_0{}^* =$ -25. Figure 6.8a shows the trajectories of the particles are dependent on their initial position, with the particles maintaining the same order in the channel in the vertical section as

initially present. All three cases seem to be translating a small amount in the $+X^*$ direction, as would be inferred from the positive angles of the particles, leading to a reduced horizontal separation compared to the initial vertical separation. The varying proximity to the inner corner is evident in the varied velocities through the corner. The ${Y_0}^* = +1$ case translates with the greatest velocity through the corner since it is nearest the high electric field region. Oppositely, the ${Y_0}^* = -1$ case is the furthest away and translates the slowest. The angular motion in Fig. 6.8b, demonstrates the effect of the walls on the rotation of the particles. The ${Y_0}^* = -1$ case exits the corner and is located closer to the right wall which results in greater torque on the particle and a larger angle compared to the ${Y_0}^* = 0$ case. The different shape of the ${Y_0}^* = +1$ case is a result of the interaction of the trailing edge of the particle to the high electric field region of the inner corner. Here the trailing edge is accelerated, causing the angle of the particle to decrease until the particle leaves the corner region and the boundary induces the increase in angle seen of the remainder of the angular plot.

6.5 Summary

The nonsteady motion of a cylindrical particle under electrophoresis was modeled as the particle moves through a 90° corner. One goal of the chapter was to investigate various parameters and geometries of the system to fundamentally determine the effect on the motion of a cylindrical particle. The trajectories of the particles were simulated numerically using a deformable mesh to capture the particle motion. Changing the zeta potential of the system changed the particle velocity, but did not effect the trajectory or angle of the particle. Likewise, alterations in

the channel width and particle aspect ratio had minimal effects on the trajectories of the particles. The initial angle and initial vertical position of the particle were found to have significant effects on the particle motion. The initial angle causes a variation in particle trajectory of a few particle radii, and causes three distinct Classes of angular motion through the corner region. Likewise, the initial position effects the paths of the particles and the angles of the particles as they move through the corner. It is evident that there is some potential for using a corner region as a passive control element as part of a larger microfluidic system. Particles passing through the corner with an initial distribution of angles to the vertical of 90°, exited the corner with a difference of angle of less than 30°. However, this effect is limited to the region immediately surrounding the corner suggesting that to be useful it would have to be used in close succession with other control elements.

Chapter 7

Separation Distance of a Gold Nanowire from a Glass Substrate

7.1 Introduction

In order to better interpret experimental work on the electrokinetic motion of nanowires in microfluidic channels, it is important to determine where the nanowires are located in the channel. When the nanowires are suspended in an aqueous solution in a microfluidic channel they will come to an equilibrium position with respect to the bottom wall as they are pulled downward by gravity and pushed upward from the wall by electrostatic repulsion. A previous work (46) roughly estimated this equilibrium separation distance at around 200 nm, based on the size of the electrical double layers surrounding the particle and the channel wall. In order to determine the separation distance with more accuracy a confocal microscope with a high speed videography setup was used to measure the separation distance between a suspended nanowire and the lower glass channel wall.

7.2 Data Collection

To make the measurement as precise as possible a confocal microscope system in the laboratory of Dr. James Gilchrist in the Chemical Engineering Department at Lehigh University was used for the experiments. The microscope system was chosen for its ability to rapidly take measurements and to do so at smaller increments of motion in the z-direction (the direction of gravity). The system to be measured was a suspension of gold nanowires in deionized water. The nanowires had an average length of 5.3 μm and an average diameter of 273.8 nm, as measured by electron microscopy. They were coated with a self assembled monolayer of sodium 2-mercaptoethanesulfonate (MESNA), which provides a negative surface charge to the nanowire surface. The deionized water contained a small amount of rhodamine B fluorescent dye for visualization purposes.

The desired measurement is the distance from the lower glass wall to a suspended nanowire. The key to the measurement was providing a reference point for the measurement of the nanowire since it was not readily possible to accurately measure the location of the glass surface. The reference was established by placing a drop of nanowire suspension (without the dye) on the coverslip and allowing the water to evaporate. After evaporation, the coverslip was then covered by a group of nanowires that were adhered to the glass surface, which could be located accurately by the microscopy system and provide a reference for the location of the glass surface. A drop of the nanowire suspension was placed on the cover slip for observation in the inverted microscope. The fluorescent dye was added to the measurement sample so that the fluid would be bright and the nanowires dark, improving the contrast in the captured images.

All images were captured with an Olympus IX-71 inverted microscope through a 100x/1.4 oil objective and a VisiTech "Vt-eye" (VsiTech International, ltd. Sunderland, UK) scanner. The measurements were made by focusing on a desired region of space and capturing a series of images at various points in the z-direction. A piezoelectric element precisely moved the objective in the z-direction, with a minimum motion of 0.1 μm (100 nm). Each measurement was a series of 70 512x512 pixel frames, each frame a 0.1 μm increment in the z-direction from the last. The 70 frames were captured at 80 fps, so that each individual measurement occurred quickly minimizing the effect of Brownian motion on the position of the suspended nanowire. A total of 20 such measurements was captured at each sample, 10 scans upward and 10 scans downward in the z-direction. Figure 7.1 illustrates the positions of the various elements of the measurement and the planes captured by the images.

The series of 20 measurements was repeated nine times with a different initial z plane selected by manual focus adjustment each time. This method ensured that the distance between the wires was measured by a different number of measurement planes. The distance to be measured was estimated to be as large as two or three measurement planes, so by altering the positions of the wires within those planes the average measurement should more closely approximate the actual separation. So with nine samples of 20 measurements each, a total of 180 measurements of the separation between the suspended nanowire and the nanowire fixed to the surface were captured. These measurements of the distance between nanowires can be used to determine the distance from the surface. Due to optical distortions in the system, it is not known whether the brightest plane of the nanowire is the

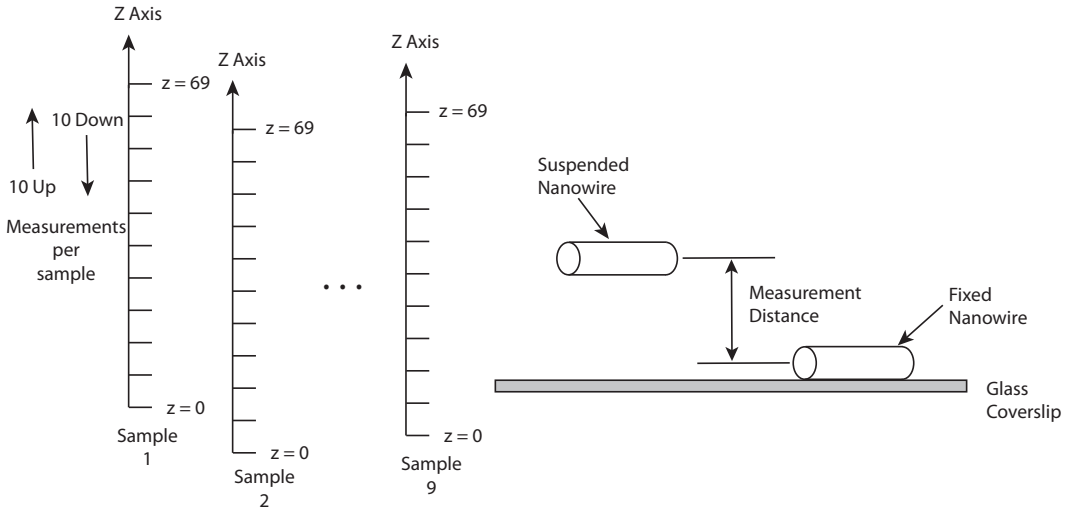

Figure 7.1: Diagram of the system for measuring the separation of the suspended nanowire from the glass substrate. A nanowire fixed to the glass serves as a reference that is visible and at a known location. The measured distance from the fixed nanowire to the suspended nanowire corresponds to the desired measurement from the glass to the suspended nanowire. An illustrative bar in the z-direction demonstrates some of the measurement planes. The location of the z=0 plane is altered for each sample to vary the locations of the planes between the nanowires. Figure is not drawn to scale.

center plane (in the z-direction), but the brightest plane of both the suspended and the fixed nanowire will be the same plane. Therefore, the measurement of the separation of the wires will correspond to the distance from the glass surface to the bottom of the suspended nanowire, which is the desired measurement.

7.3 Image Analysis

Each of the series of 70 images was captured as one tiff file for use in image analysis. A set of particle tracking macros for the IDL programming language (ITT Visual Information Services, Boulder, CO) developed by John Crocker and David

Grier (47), and maintained by Eric Weeks (48) were used to analyze the captured images. Initially, the images are inverted so that the particles appear bright on a dark background which is required by the particle tracking software. A spatial bandpass filter is used to smooth the image and change the background to black so that the particles stand out. The bandpass filter is given an estimated size of the particles of interest in the x, y, and z directions. The bandpass filtered image is then searched for particles by identifying the brightest points and examining the surrounding space within a specified size to identify the boundaries of the particle. The particles identified are then examined in all three spatial dimensions to determine the center of the particle. The software searches for particles that are spherical, but readily finds the nanowires of interest as a single line of spheres. The estimated size given to the software is determined by measuring the diameter of the nanowire in a variety of images, so that the spheres identified occupy the majority of the nanowire. The effect is similar to identifying the tube shape of a container of tennis balls by only looking at the tennis balls it contains. Once the spheres that make up both nanowires are identified the average height in the z-direction is calculated for each nanowire, as an average of the positions of the particles that make up each nanowire. The difference in height is then found and the process repeated for each of the 180 data points. Figure 7.2 illustrates the progression of steps in the image analysis procedure.

7.4 Results

The image analysis process described above was automated with a script in IDL to eliminate any human biases in examining the data. A predicted size of the imaged

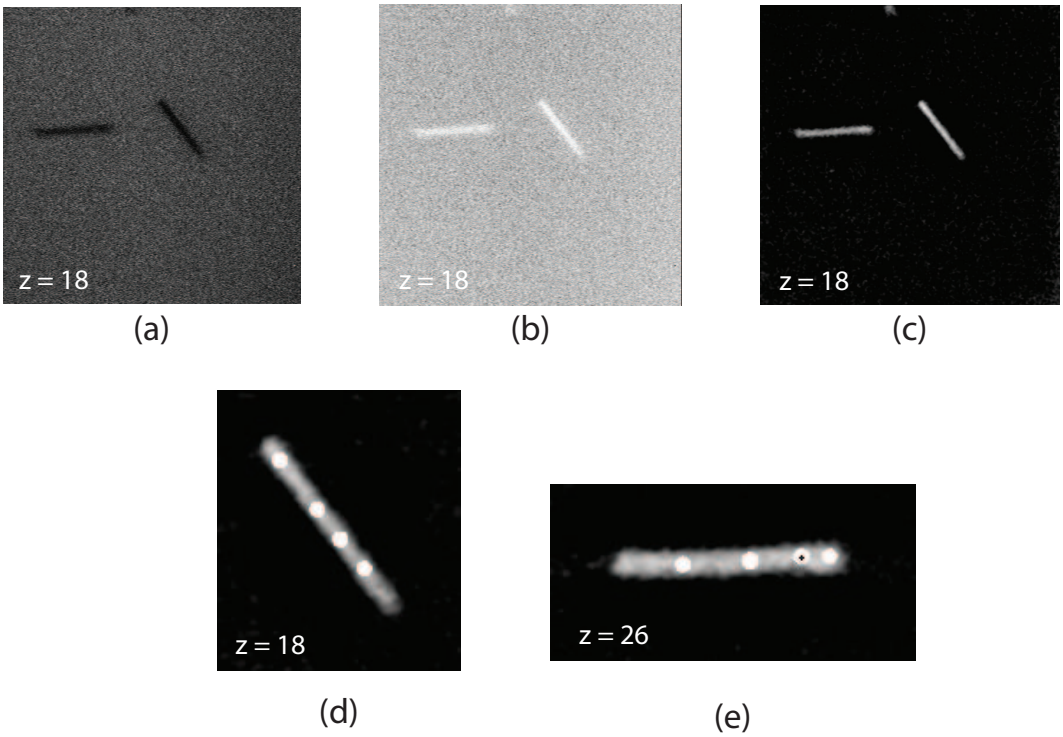

Figure 7.2: Process for analysis of the captured images. (a) A raw image captured from the microscope at the $z = 18$ plane. (b) Image after inverting so that the nanowires are bright. (c) Image after the bandpass filter has been applied. (d) Zoomed in view of the spheres identified on the reference nanowire (nanowire on the right in the original image). (e) Zoomed in view of the spheres identified on the suspended particle (nanowire on the left in the original image), note that the image is from the $z = 26$ plane.

particles was required to run the bandpass filter and the particle locating scripts. The diameter of the nanowires was measured in the x, y plane from multiple frames from throughout the data collected. The diameter of the nanowires was measured to be roughly 29 pixels. Similarly, a measurement of the diameter of the nanowires in the z-direction was taken from slices made by compilation of the series of 70 images. The typical nanowire diameter was 15 pixels in the z-direction. These conditions were used in the script to measure the separation of the reference and suspended nanowire in the 180 measurement instances. The process was repeated

twice more to determine if the particle size estimates affected the results. The script was run with an estimate of 33 pixels in the x and y directions and 17 in the z direction, as well as 25 pixels in x and y, and 13 in z. The results obtained indicated that the estimated size of the particles did not affect the resulting measurement of the separation distance, as seen in Table 7.1.

Table 7.1: Average and standard deviation for the measured distance between the nanowires for three different estimated particle sizes.

Measurement of Distance between Nanowires			
Specified Particle Size (pixels)	29,29,15	33,33,17	25,25,13
Average	7.75	7.64	7.61
Standard Deviation	2.22	2.47	2.38

The difference in the estimated distance only varies by 0.14 planes in the z-direction (7.61 to 7.75), indicating a minimal effect of varying the predicted particle size. Using the results from test with the measured size of the diameter of the nanowire, 29x29x15 pixels, the nanowires are separated by 7.75 planes in the z-direction. This distance is equal to 775 nm, which represents the average distance from the 180 measurements.

The suspended nanowire is moving due to Brownian motion so a range of values based on the measurements would better capture the true behavior of the nanowire. The 95% confidence intervals for the separation distance are 743 nm and 807 nm, which indicates, that within the data set available, the nanowire was not moving drastically in the vertical direction due to Brownian motion. The range of measured separation distances is significantly larger than previous estimates of 200 nm. However, experimental work with the nanowires has demonstrated that suspended nanowires readily travel over nanowires that are fixed to the surface

of the channel with no effects on their trajectories. Since the nanowires have an average diameter of 273.8 nm they must be separated by a distance greater than this since they are observed not to interact. The experimental observations lend credence to the measured values reported above.

7.5 Comparison to Numerical Results

An estimate of the separation distance from a suspended nanowire to the bottom channel surface provides a point of reference for comparing the numerical results to the experimental results. The nondimensional separation distance is the distance from the wall to the center of the particle divided by the particle radius. Converting the measured separation of 775 nm to the nondimensional measurement used in the numerical studies yields a separation of $h^* = h/a$ =6.7, [$h^* = (775\ nm + \frac{273.8nm}{2})/\frac{273.8nm}{2}$]. This separation distance can be compared to the bounded motion results of Chapters 4 and 5. The previous numerical work explored separations of h^*=1.1 to h^*=35, with the boundary effects becoming significant when h^* <10.

Figure 7.3 repeats the results of two numerical studies of the eccentrically positioned particle since that case more closely resembles the experimental conditions than the concentric case. The measured separation distance is indicated by a vertical line at h^*=6.7. In Fig. 7.3a the velocity of the nanowires is not largely effected by the presence of the wall at h^*=6.7. The variation from the velocity in the unbounded case at h^*=6.7 ranges from 0.01% to 0.05%. The results in Fig. 7.3b demonstrate a more significant difference as the particle angle increases, with velocity variations ranging from 0.06% to 0.20%. The predicted boundary ef-

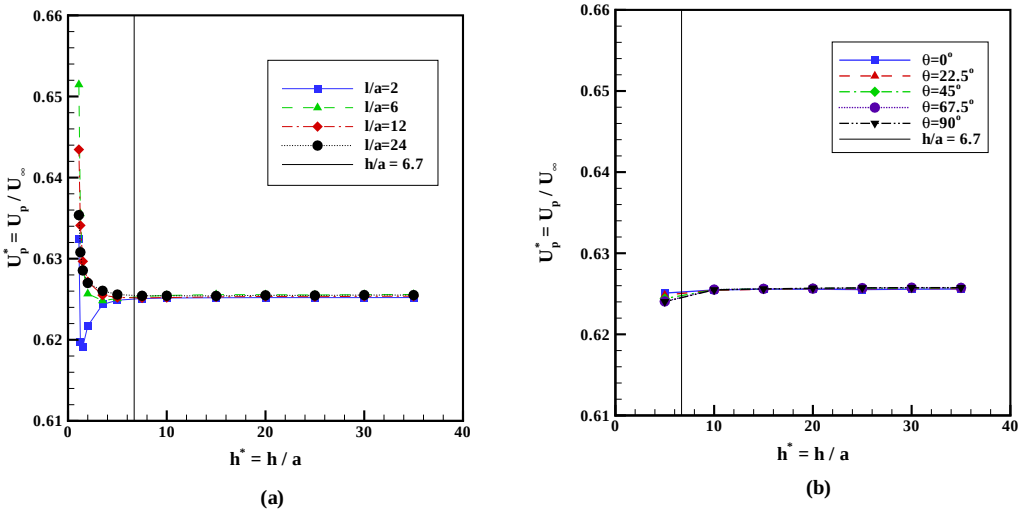

Figure 7.3: Numerical results for the effect of the boundary on the velocity of an eccentrically positioned particle, with the experimentally observed separation distance indicated by a vertical line at h^*=6.7. (a) Velocity effect as the aspect ratio of the particle is varied. (b) Velocity effect as the angle of the particle to the horizontal is varied. Data from 3D numerical models.

fects on the velocity of a nanowire at h^*=6.7 are not significant and likely will not be measurable experimentally. However, the previous nonsteady results (Sec. 5.5) indicated oscillatory motion for separations of 5< h^* <10. It is expected that the predicted oscillatory behavior will be experimentally observable.

7.6 Summary

The comparison to numerical results at the experimental separation distance reinforces the initial experimental results, in that the observed translational results matched the theoretical predictions for unbounded flow. The unsteady motion and rotation of the nanowires observed in those experiments prompted the detailed numerical studies that have now demonstrated the small velocity variation and

rotation of the nanowires. Further experimental study of these effects is included in the following chapters.

Chapter 8

Experimental Validation of Numerical Predictions

8.1 Introduction

In order to obtain the flexibility in size and geometry of the microfluidic channels necessary to compare to the numerical results, a new experimental apparatus was developed. The new channels were constructed out of PDMS (polydimethylsiloxane) and were used to measure the electrokinetic velocity of gold nanowires in smaller diameter channels (compared to Chapter 3), observe the vertical translation and rotations of nanowires numerically explored in Chapter 5, and to validate the orienting effects of 90° corners predicted in Chapter 6. To fully explore the velocities of the nanowires it was necessary to determine the zeta potential of the PDMS. Instead of using nanowires with zero zeta potential as before, commercially available fluorescent PSL (polystyrene latex) spheres with 1 μm diameter were purchased. The zeta potential of the PSL particles was measured with the ZetaPALS

instrument (Brookhaven Instruments Corporation, Holtsville, NY). Once the zeta potential of the PSL particles was known, their electrokinetic velocity was measured. The only unknown in matching the PSL velocity to theory is the zeta potential of the PDMS walls, so it can be readily calculated. This method of calculation of the wall zeta potential is advantageous over the use of zero zeta potential nanowires because the measurement techniques and theoretical calculations for spherical particles are more robust.

With the PDMS zeta potential, the only unknown in the electrokinetic velocity of the nanowires is the zeta potential of the nanowires. This quantity was measured using the ZetaPALS instrument, but was found to be more variable than measurements of other samples possibly because of their nonspherical shape. Comparisons to the measured zeta potential of the nanowires can be made by comparing theoretical values to the measured electrokinetic velocities.

8.2 Experimental Process

8.2.1 Channel Manufacture

The previous experiments used commercially available square glass channels with minimum cross sections of 80 μm x 80 μm. The numerical results most of interest occurred in channels with widths twice the length of the particles, so in this case channel diameters of 10 μm. Additionally, the results of orienting a nanowire through a 90° corner necessitated the use of channels that were not straight. To accomplish these goals the channels used in these experiments were manufactured out of PDMS. PDMS is a polymer that is optically clear, rigid enough for microflu-

idics work, and can be easily molded using microelectronic manufacturing methods. The development of the manufacturing process was carried out with staff from the Penn State Nanofabrication Laboratory. Manufacture of the channels was carried out by Shahrzd Yazdi, a member of the Microscale Flow Laboratory, in the Nanofabrication Laboratory. An overview of the process is presented below, please refer to Shahrzad Yazdi's thesis for details (49).

PDMS is formed by mixing the base polymer with a curing agent and applying heat to speed the solidifying process. Since both components are liquid it is possible to use a variety of means to mold the PDMS into desired shapes. In this case, a silicon wafer serves as the base of the mold. A photoresist, SU-8, is spun onto the disk to provide a uniform, flat coating. Additional layers of SU-8 are spun onto the wafer to slowly build up a uniform layer that is 50 μm tall. Once the desired height is reached, the SU-8 is exposed to UV light through a mask that only allows the light to hit the SU-8 where the desired channels are located. The UV light causes the SU-8 to harden, and the unexposed regions can be removed with developer solution. After washing, what remains is a negative mold of the desired channels raised in SU-8 above the silicon wafer. The wafer is then placed into a petri dish of similar diameter and the PDMS solution poured over the wafer to a depth greater then the SU-8. The PDMS is cured and then peeled off the wafer to expose the channels in the PDMS. The channels used in the experiments had a cross section 10 μm across and 50 μm deep, while the channel itself was 10 mm long. A thin, flat piece of PDMS of equal diameter was cured to act as a capping layer for the channels. A series of 3.5 mm holes was punched through the cap layer at the locations of the wells at the end of the channels, the holes

provide fluid and electrical access to the channels. The channels and capping layer are activated in an oxygen plasma chamber and brought into contact to bond. A single wafer contains up to 30 channels of various widths as well as both straight and 90° corners. Figure 8.1 contains an illustration of the structure of the channels developed.

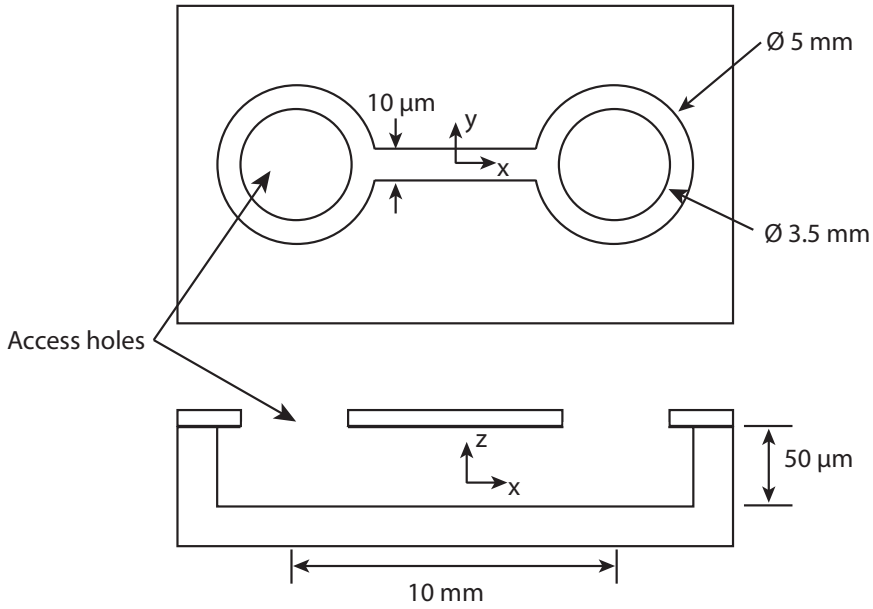

Figure 8.1: Schematic diagram of the microfluidic channels constructed in PDMS. Relevant dimensions and coordinate system are indicated.

8.2.2 Experimental Populations

The PSL control particles were purchased from Invitrogen Inc (Carlsbad, CA). They were spherical particles with a 1 μm diameter and absorbed light at 535 nm and emitted at 575 nm (nile red). The particles arrive at a concentration of 2% weight/volume (2 gm of particles suspended in 100 mL of water) and are diluted with a KCl solution to a concentration of 3.1x10^{-4}% weight/volume and ionic

concentration of 1 mM for use in the experiments.

The gold nanowires were manufactured using the same process as in Sec. 3.3 (29). The population of wires used in these experiments had an average length of 5.3 μm and an average diameter of 273.8 nm for an aspect ratio of 19.35. The initial concentration of the gold nanowires is not known, but the solution is diluted 300 times with DI water for use in the experiments. DI water was used for these experiments, but tests were conducted on nanowires samples in aqueous solutions of KCl at concentrations of 1 mM, 10 mM, and 100 mM. The nanowires remained suspended above the lower channel wall and free to move at concentrations of 1 mM and 10 mM, but were completely adhered to the channel wall at a concentration of 100 mM.

8.2.3 Data Collection

The process for collecting data is similar for all the experiments. A single channel was separated from the wafer sheet of channels for use in the experiment. It was placed under the microscope (Olympus BX51, with a 20x objective) and 15 μL drops of particle suspension simultaneously placed into the wells at each end of the channel by micropipettes. Simultaneously placing the drops into each well minimizes the pressure difference between the wells. A platinum wire was placed into each well to provide the electric field supplied by the function generator (HP 3325A). The electric field applied was a 0.1 Hz square wave at 20 V_{pp} (10 V applied across the channel at a time). Thermal flows from Joule heating are not expected to be significant due to the low frequency (50) and low voltage (51) applied in the experiments. A digital, color microscope camera captures 50 frame videos of

the particle motion at 33.33 fps. Videos of the PSL particles were captured using standard fluorescent microscopy with mercury lamp illumination and a TRITC filter cube. Videos of the gold nanowires in the straight channels and the 90° corners were captured using brightfield microscopy with a mercury lamp for better illumination than the normal halogen lamp.

The number and order of the videos collected varied depending on the experiment. The collection method used in the straight channel experiments began by collecting videos of the motion of the PSL particles. The density of PSL is similar to water so the PSL particles did not rapidly sink to the bottom of the channels. Videos of the PSL motion were taken at various depths in the channel. First, the focus was adjusted as far to the bottom of the channel as particles were in focus. This depth was termed 0 μm, representing the lowest particles, not necessarily the bottom of the channel. A video was taken at this depth, then the focus plane was raised 10 μm and another video captured. This continued upward through the channel until videos were captured at 0 μm, 10 μm, 20 μm, 30 μm, 40 μm, and 50 μm.

Initially, the pressure that exists in the channel was measured by capturing videos at each depth without the electric field. The electric field was then applied and the focus returned to 0 μm. Here two videos of the electrokinetic motion were captured, one in each direction (since the applied electric field was alternating at 0.1 Hz for pseudo-steady flow in each direction). Two movies were subsequently captured at each of the other depths up to 50 μm. The electric field was turned off and the pressure videos repeated as before. This allows for calculation of the average pressure flow present during the electrokinetic experiments since pressure

measurements were captured before and after the electrophoretic runs.

A similar process was used for capturing the videos for the motion of the nanowires. The primary difference is that the heavy gold nanowires sink to near the bottom of the channels rapidly so video was only captured at one depth. Two videos were captured of the pressure flow in the channel, then eight videos (4 in each direction, alternating) were captured of the electrokinetic motion, followed by two more videos of the pressure flow. This process was repeated for as many channels as possible before the surface activation of the PDMS fades and the channels revert to hydrophobic. PDMS is naturally hydrophobic but can be made hydrophilic by activating the surface with oxygen plasma. The change to hydrophilic surfaces is not permanent and the surfaces revert over time (observed to be around 120 minutes), limiting the experimental usefulness of a set of channels. Two complete sets of data in the straight channels were acquired (corresponding to two days of experimental acquisition). Set A consisted of one full set of PSL videos and then three channels of nanowire videos. Set B contained the channel of PSL videos and two channels of nanowire video.

The process of collecting video of the nanowires in the 90° corner was similar to the previous process except no PSL particles were used in the corner channels. Two videos of the pressure flow were collected, followed by eight videos of the electrokinetic motion (4 in each direction), followed by two more pressure videos. Three sets of corner data were collected, the first set with one channel and the second an third sets with two channels each.

8.2.4 Data Analysis

The initial phase of the data analysis process is the same whether the data are from PSL particles or nanowires. The first step is to subtract off the average background image of the video. This step removes any particles that are not moving during the movie from the images to make it easier to see the particles that are moving. To do this the movie file is opened in the program ImageJ (NIH, Washington, DC) where it is converted into grayscale. The image frames are averaged and a new image is created of the average. The average frame is subtracted from every frame of the movie to eliminate the static background. This works because any particle (or noise) that is not moving will show up bright on the average frame and be removed when subtracted.

Particle tracking techniques were used to analyze the motion of the particle, however the methods depended on the type of particle. For the PSL particles, the particle tracking process was largely automated using the particle tracking macros developed by John Crocker and David Grier (47), and maintained by Eric Weeks (48) for the IDL programming language (ITT Visual Information Services, Boulder, CO). The particle tracking process used was similar to the 3D particle tracking described in Sec. 7.3 and illustrated in Fig. 7.2. Here, spherical particles are tracked as circles in 2D images. The automated process began by applying a spatial bandpass filter to each image in the movie with a diameter about equal to the size of the particle in the image. This helped the particles stand out more from the background. The program then went through and identified each of the particles in the image. A minimum brightness was set so that any dim, out-of-focus particles were rejected. At this point the locations of the particles were

compared between frames in order to determine their trajectories. The program used a supplied maximum displacement value and correlation statistics to track the particles. Any particle that was not tracked through at least 10 of the 50 frames was rejected, as were particles that came in and out of focus. The end result of the tracking macros was an array containing the x and y coordinates of each particle, the current frame, and a particle number. The array was arranged by particle number, so a simple IDL macro was written to take each results array and calculate the average x-velocity and y-position in the channel for each particle tracked. In the analysis of these movies, the x-direction is along the channel parallel to the applied electric field. The y-direction is perpendicular to the electric field, the narrow dimension of the channel, 10 μm across. For clarity on the coordinate system, refer back to Fig. 8.1.

The analysis of the nanowire videos followed a similar process except it was carried out manually because the particles were not spherical. After the movies had the background subtracted off, each frame was saved as an individual image file for analysis in Photoshop (Adobe Systems Inc, San Jose, CA). Every other frame from a movie was opened in Photoshop. A frame was skipped because the motion evident in one frame difference was often not significant (time between frames was 0.03 s). In Photoshop, each image was passed through a threshold filter which creates a black an white image from the original grayscale at a specified value. This creates an image of white nanowires on a black background for easy identification. The x and y coordinates of the leading and trailing tips of each wire were recorded for each wire that was present for a majority of the frames. This filtering and recording of coordinates was repeated for the remainder of the

frames. The nanowire image analysis process is shown in Fig. 8.2

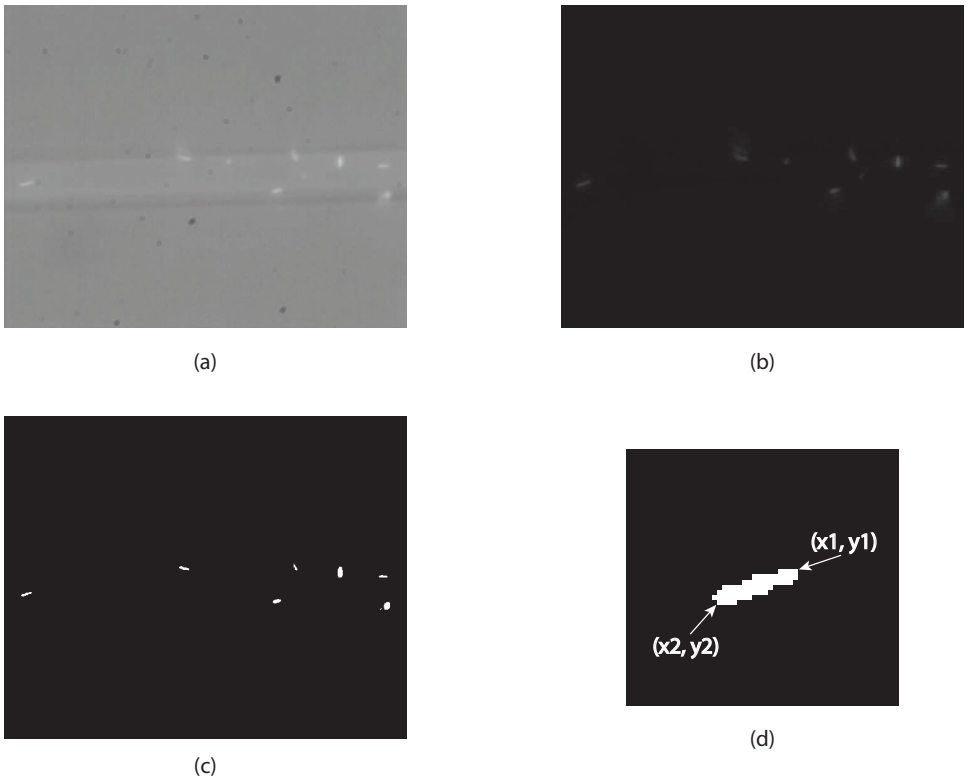

Figure 8.2: Sequence of analysis of nanowire images. (a) Raw image captured from the camera. Channel walls visible for calculation of pixel to micrometer conversion. (b) Image after the average background was subtracted. (c) Image after applying a threshold filter. (d) Zoomed image of a single nanowire with pixels on each tip identified. The location of each tip is used to calculate the location of the particle center and it's angle.

An Excel (Microsoft Corp, Redmond, WA) worksheet was used to calculate the center of each particle and subsequently the velocities in the x and y directions of the center of the particle. The Excel worksheet also calculated the angle of the nanowire as well as its postition in the channel. The pixel and frame information was converted to μm and s for ease of comparison. As before, the average y-position, angle, x-velocity, and y-velocity of the nanowire were calculated and used for analysis. The average quantities were used because the trajectory that

was tracked within one movie was small and the change in the quantities of interest minimal. The trajectories that were tracked within 50 frames only represent a maximum of 35 non-dimensional seconds, which represents a small segment of the trajectories from Sec. 5.5 which have periods of 300 non-dimensional seconds.

8.2.5 Verification of Assumption of an Open System

Previously, the experimental system was was assumed to be open (or reasonably close to an open system) because no return flow was observed in the channels. Return flow is pressure driven flow caused by a buildup of fluid in one reservoir as the electroosmotic flow moves fluid in one direction. In order to provide an estimate of the expected return flow during these experiments the following model was used. Simplifying the PDMS channels slightly, assume a channel with a cross section of 10 μm x 50 μm, which is 10 mm long connecting cylindrical reservoirs that are 5 mm in diameter.

First calculate the volume of fluid that would move from one reservoir to the other during a 10 s period of electroosmotic flow (AC field of 0.1 Hz). Use the measured velocity of 30 μm/s, the above cross section, and time yields the volume of fluid moved:

$$V = uAt \tag{8.1}$$

$$V = (30x10^{-6}m/s)(10x10^{-6}m)(50x10^{-6}m)(10s) \tag{8.2}$$

$$V = 1.5x10^{-13}m^3. \tag{8.3}$$

Next calculate the change in fluid height in the reservoirs caused by this volume

of fluid.

$$h = \frac{V}{A} = \frac{1.5x10^{-13}m^3}{\pi(2.5x10^{-6}m)^2} = 7.6x10^{-9}m \tag{8.4}$$

One reservoir increases by 7.6 nm and the other decreases by the same amount. That creates a height difference between the wells of 15.3 nm. A pressure difference due to this height difference is easily calculated:

$$\Delta p = \rho g \Delta h \tag{8.5}$$

$$\Delta p = (1000kg/m^3)(9.8m/s^2)(15.3x10^{-9}m) \tag{8.6}$$

$$\Delta p = 1.5x10^{-5}N/m^2. \tag{8.7}$$

Finally, calculate the maximum velocity caused by this pressure difference. For simplicity, use the theory for flow between flat plates since the channel is five times deeper than wide. Using the expression for laminar flow between plates from Fox and McDonald (52) the max velocity is:

$$u_{max} = \frac{3(\Delta p)a^2}{24\mu\Delta x} \tag{8.8}$$

$$u_{max} = 1.9x10^{-10}m/s \tag{8.9}$$

where a is the channel width, 10 μm, and Δx is the channel length, 10 mm.

The analysis above helps to demonstrate why closed system recirculation is not observed in the experiments conducted. The size of the fluid reservoirs used in the PDMS channels is large relative to the channel size. Therefore, the pressure flow that develops due to the electroosmotic movement of fluid from one reservoir to the other is four orders of magnitude smaller than the observed electrokinetic

velocity. This analysis validates the previous assumption of an open system over the experimental time scales.

8.3 Electrophoresis Results in a Straight Channel

The results of the experiments conducted in the straight channels can be separated into two sections; the first the average bulk velocity of the nanowires and a comparison to theoretical predictions, the second is an analysis of the rotation and vertical translation to determine if the nanowires move in an oscillatory motion as numerically predicted.

8.3.1 Average Bulk Nanowire Velocity

In order to determine the average velocity of the nanowires, the velocity of the PSL particles is calculated to determine the zeta potential of the PDMS channel walls. The raw data captured from the experiments results in average velocities and channel positions for each particle tracked. The average velocity reported contains the influence of the pressure flow that exists in the channel. To remove the presence of the pressure flow on the velocity measurements, the average velocity of each particle tracked in the before and after pressure videos is plotted and a parabolic trendline fitted. The equation of the trendline provides a means for calculating the effect of the pressure velocity on the measurements of the electrokinetic velocity. Each electrokinetic velocity is altered the appropriate amount by calculating the pressure velocity at that point in the channel with the trendline

equation. Repeating this with every particle that is tracked results in data that represents the observed sum of the electroosmotic velocity and the electrophoretic velocities. Table 8.1 summarizes the observed electrokinetic velocities for the data sets.

Table 8.1: Observed electrokinetic velocities for the PSL experiments.

	Set A	Set B
Channel Depth (μm)	Avg x-Vel (μm/s)	Avg x-Vel (μm/s)
0 (bottom)	21.2	19.4
10	19.2	25.6
20	18.4	26.6
30	21.2	32.9
40	14.9	26.3
50 (top)	16.0	24.9
Average	18.9	25.3

The overall averages reported were calculated based on all the measured particles, 126 in Set A and 146 in Set B, not from the averages of each channel height. The average values of the two data sets differ slightly, 18.9 μm/s vs. 25.3 μm/s, likely due to slight differences in the oxygen plasma activation process on the differing days of the experiments. As such, a value of the PDMS zeta potential is calculated for each data set independently and then used in the subsequent nanowire calculations to properly account for this difference. In order to calculate the PDMS zeta potential, the zeta potential of the PSL particles is needed and was measured using the ZetaPALS instrument. The measured value was corrected to reflect the EDL thickness in these experiments (21), and was found to be -26.0 mV. The particle zeta potential was used to calculate the theoretical electrophoretic velocity, U_{ep}, which can be inserted into the superposition equation (Eqn. 2.19), where pressure is already accounted for and Brownian motion is again

neglected leaving

$$U_{obs} = U_{eo} + U_{ep}. \tag{8.10}$$

The PDMS zeta potential is varied until the sum of the theoretical electroosmotic velocity and electrophoretic velocity equals the electrokinetic velocity observed experimentally. The calculated value for PDMS zeta potential for Set A is -42.8 mV and for Set B is -50.8 mV.

Values of the zeta potential of PDMS in contact with 1 mM KCl solutions are available in the literature and reported as -87.0 mV (53) and -83.3 mV (54). These values are significantly different than the values obtained experimentally, however the preparation of the PDMS channels in the literature differs from the case presented herein. In both experiments in the literature, the PDMS channels are molded, bonded to form a channel, and then filled with solution and aged for various lengths of time. Due to the current constraints in location of PDMS manufacturing versus the experimental apparatus, the PDMS channels created for these experiments spend a period of time exposed to air which likely alters the surface properties of the channels. Differences in surface treatment of PDMS greatly affect its bonding properties and hydrophilic state, so it is expected that the differences in measured zeta potential versus those reported in the literature are a result of differences in manufacturing.

The values of the PDMS zeta potential are carried over to the calculations of the nanowire velocity. The only quantity unknown in the theoretical equations for the nanowires is the nanowire zeta potential. In Chapter 3, a value of -27 mV was used for the nanowire zeta potential. This value was the average of a limited number of measurements taken using the ZetaPALS instrument. Since those

tests, an additional 19 measurements have been taken with an average nanowire zeta potential of -35.0 mV. This compares favorably with the previous value, however the variability of the measurements lends credence to the assumption that the ZetaPALS measurement may not be ideally suited to non-spherical particles. The range of measurements obtained was from -9 mV to -64 mV, indicating that the average value obtained may have little basis in truth, as such the value of the nanowire zeta potential is calculated based upon the observed nanowire velocities. This situation is less than ideal as there is no true theoretical value for comparison of the experimental results. However, the two sets of data were captured using channels with differing wall zeta potentials, but the nanowires used in the experiments were the same. A reasonable check on the theoretical validity of the experiments is to determine if a single nanowire zeta potential satisfies the experimental observations of the two experiments.

The velocity data from the nanowire experiments was prepared similarly to the PSL data above. The pressure velocity measurements from before and after each electrokinetic run were plotted to develop a parabolic trendline. The average electrokinetic velocities were corrected for pressure according to their positions in the channel. The measured pressure flow accounted for 3.7% to 12.7% of the observed electrokinetic velocity. The average x-velocities for each nanowire measured were collected and are plotted in Fig. 8.3 against the nanowires' position in the channel. The plotted velocities exhibit randomness that is expected in experimental data, however the variations in measured velocities do not follow any expected patterns. The velocities are not higher in the center of the channel, indicating that the effects of the pressure flows have been appropriately subtracted from the measured

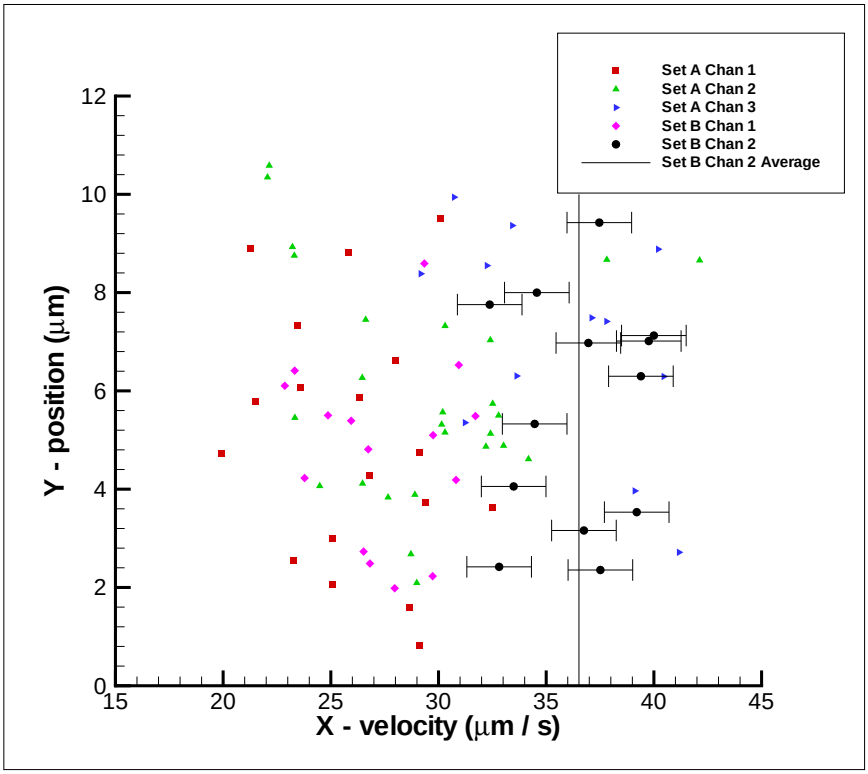

Figure 8.3: Nanowire velocity in the x-direction plotted against the position of the nanowire in the channel (direction perpendicular to the applied electric field). The nanowire velocities vary randomly across the width of the channel indicating pressure influences have been removed and that the nanowire motion is nearly plug flow as expected in electrokinetic motion. The average velocity for Set B Chan 2 is included as a vertical line with error bars on the data points representing estimated experimental uncertainty as an illustration of plug flow.

velocities. The range of x-direction velocities within each channel data set appear to be relatively flat resembling plug flow expected from electrokinetic flow in an open system.

The average x-direction velocity for each set of data was calculated yielding 29.1 μm/s for Set A (56 nanowire trajectories) and 32.2 μm/s for Set B (29 nanowire trajectories). These values were plugged into Eqn. 8.10, simplified to such for the same reasons as above, where the only unknown is the nanowire zeta

potential used to calculate U_{ep}. Equation 3.1 is used to calculate U_{ep} for non-spherical particles, the value of g_{av} appropriate for the experimental conditions comes from Stigter (28). The value of nanowire zeta potential that produces the best agreement between theory and experiment is -11.5 mV. Using this value, the predicted electrokinetic velocity for Set A is 27.5 μm/s compared to the experimentally observed velocity of 29.1 μm/s, a difference of 5.58%. The predicted velocity value for Set B is 34.0 μm/s compared to 32.2 μm/s, a difference of -5.60%.

The experimental observations compare favorably with the theoretical constructs in both data sets indicating that the simple theory used is appropriate to the experimental conditions. However, the usefulness of the theory depends on the value of the nanowire zeta potential. In this case, a value of -11.5 mV provided good agreement with the experimental observations. This value of nanowire zeta potential is within the wide range of measurements taken, however it does not contribute to establishing a true, consistent value, since it has yet to be determined if the wide range of values is measurement error due to particle shape or a variable in the manufacturing process.

8.3.2 Nanowire Trajectory in a Straight Channel

The experimental observations of the nanowire motion in straight channels included measurements of the nanowires' angles as well as their velocities in the x- and y-directions. Refer to Fig. 8.1 for coordinate systems, the x-direction is along the channel and the y-direction is across the narrow width. The angle is defined, as in Fig. 5.1, where positive is counter clockwise from the horizontal. From these data it is possible to explore the trajectories of the nanowires and compare them

to the numerical trajectories derived in Chapter 5 and displayed in Fig. 5.3. It is not possible to construct a similar trajectory image from the experimental data due to the limited amount of time the wires are located in the camera window. As mentioned earlier, the length of time a nanowire is visible is a maximum of 35 non-dimensional seconds, but the trajectories depicted in Fig. 5.3 occur over 300 non-dimensional seconds. Instead the y-velocities and the angles that the particles are moving with can be examined to determine if their trajectories resemble the numerical predictions.

The motion of the nanowires can be influenced by Brownian motion, a pressure induced flow due to uneven drops of fluid being added to the reservoirs, and electrokinetic flows. Determining the relative impact of the three components is difficult, but it is possible to separate the effects to some degree. Video data was acquired in two scenarios; with the electric field on and off. With the electric field off the nanowire motion is only influenced by random thermal motion and induced pressure flow. Turning the electric field on adds the electrokinetic effects to the system. Figure 8.4 compares the oscillatory behavior of the nanowires with the electric field off and on against the numerical predictions. Plotting the angle of the nanowire against the velocity in the y-direction (perpendicular to the center of the channel) provides a means of examining the oscillatory behavior of the nanowires. The numerical model of the nanowires motion did not account for Brownian motion or pressure flow, so the behavior shown in Fig. 8.4c is the result of purely electrokinetic effects. The nanowire motion in Fig. 8.4a, when the electric field is off, is the result of Brownian motion and pressure induced flow in the channel. The angles of the nanowires and the vertical translation rates are randomly distributed;

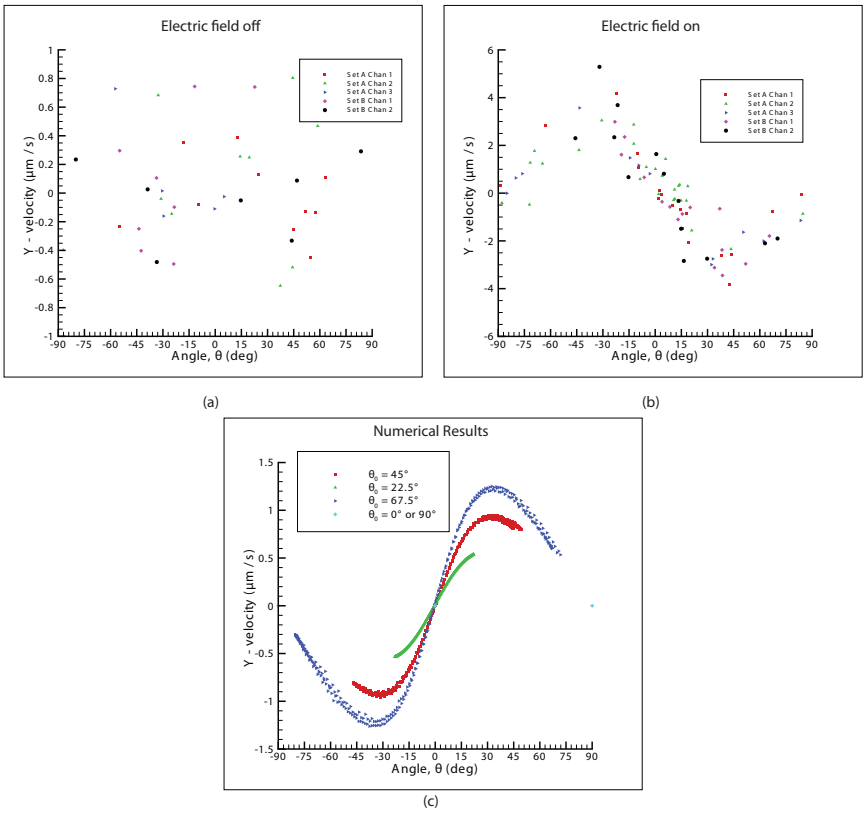

Figure 8.4: Oscillatory behavior of the nanowires. (a) Electric field turned off, only Brownian motion and pressure induced flow present. (b) Electric field turned on adding electrokinetic motion to Brownian motion and pressure induced flow. (c) Numerical results of the nanowires motion where Brownian motion and pressure flows are excluded.

the motion does not exhibit any characteristics of the numerically predicted oscillatory behavior. With the electric field on, the nanowire motion in Fig. 8.4b exhibits the same trends in the relationship between angle and vertical velocity as in the numerical case. In the experiments, the addition of the electrokinetic flows is necessary for the system to exhibit the oscillatory behavior predicted numerically. While pressure induced flow and Brownian motion are present in the experiment and contribute to the experimental error observed, they do not appear to contribute to the oscillatory behavior observed.

One variation from the numerical predictions can be noted from Fig. 8.4b and c. The angle of the nanowires moving vertically through the channel is opposite of that predicted numerically. In the numerical models, the nanowires moved vertically through the channel leading with the forward tip of the nanowire, Fig. 8.5a. This motion would correlate to a negative y-velocity at $\theta = -45°$ and oppositely a positive y-velocity at $\theta = 45°$. The experimentally observed nanowires move in the opposite fashion, leading with the broad side of the nanowire as the trailing tip rotates in the direction of travel. Figure 8.5 contains an illustration of the nanowire trajectories in the numerical and experimental cases.

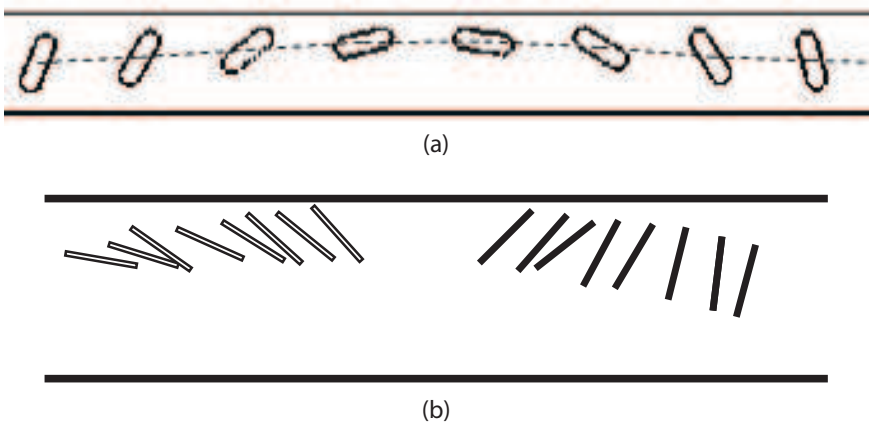

Figure 8.5: Comparison of the numerical and experimental nanowire trajectories. (a) Trajectory predicted by 2D numerical models of Sec. 5.5. (b) Trajectory observed in the experiments. Illustration recreated from data on the nanowire positions. Two different wire trajectories were used, indicated by the change in fill of the rectangles. An arbitrary distance was placed in between the trajectories near the wall.

A hydrodynamic analysis of the motion of an angled needle-like ellipsoid translating through fluid, adapted from Happel and Brenner (7), agrees with the direction and angle of the trajectory predicted numerically. The interaction of the ellipsoid with the fluid results in a translation at an angle to the horizontal toward

the tip of the ellipsoid. The details of the calculation are included in Appendix D. The presence of the lower wall in the experiments may explain the unexpected rotational behavior in the experiments as the added viscous and electric interactions impact the trajectory of the nanowire. This illustrates a limitation of the 2D nonsteady models, as a 3D effect likely causes rotation in the opposite direction.

8.4 Nanowire motion through a 90° Corner

The observations of nanowires in a corner were carried out in the same manner as in the straight channels. The x and y coordinates of the nanowires tips were recorded to monitor the velocities and angle of the nanowire. For comparison to the numerical model the angles are of primary concern. The measured angles, θ, measured with respect to the horizontal, were converted to θ' ($\theta' = 90° - |\theta|$) as in Sec. 6.4.2.1. Similarly, the time was calculated from the frame numbers and then converted to non-dimensional time t^* ($t^* = t(U_\infty/a)$). The frame where the nanowire was located in the center of the corner was designated as $t^* = 40$ to match up with the numerical data that ran from $t^* = 0$ to $t^* = 80$. Figure 8.6a contains the numerical results of θ' vs. t^* and Fig. 8.6b contains the experimental results for comparison. The experimental values for the angle through the corner appear to match the numerical data. In the numerical case, all the models ended with a value of $\theta' < 33°$ which agrees closely with the experimental case where all nanowires ended with $\theta' < 37°$. The experimental results strengthen the conclusion drawn from the numerical models that the 90° corner acts as an alignment aid. In the experimental case the initial condition was not controlled, the nanowires were initially located throughout the channel width and at many different angles yet

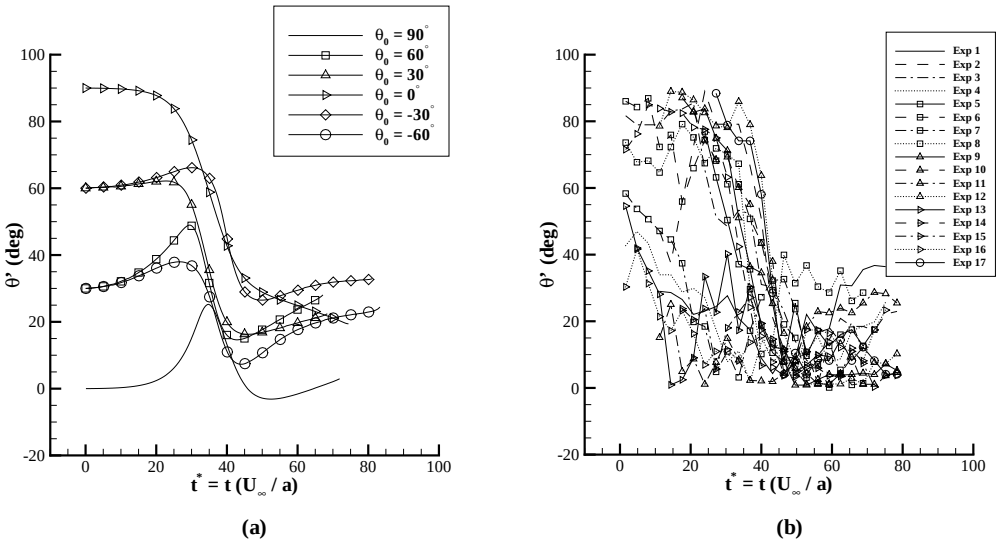

Figure 8.6: Difference in angle from the vertical direction, θ', vs non-dimensional time, t^*. (a) Results from the numerical study, repeated from Chapter 6. (b) Results from experiments with nanowires in a channel with a 90° corner.

the improvement in alignment was nearly identical. The observed results validate the numerical model of the system and demonstrate the usefulness of a corner as a passive alignment aid.

8.5 Uncertainty Analysis

The experimental process contains multiple sources of possible uncertainty in the results. Possible sources identified in these experiments are particle tracking techniques, non-uniformity of the applied electric field, and Brownian motion.

The PSL particles were tracked automatically using a widely used set of tracking macros, however the results are dependent on optimal selection of parameters. For each set of data analyzed the processing parameters were reexamined resulting in an estimated error of ±2%. The nanowires velocities were determined using

manual particle tracking techniques, so as reported in Sec. 3.5, the estimated error is ±4%.

The channel design used in the experiments aided in reducing the pressure variability in the channels, but reintroduced an error in the applied electric field due to non-fixed electrodes. The placement of the wires was fixed throughout collection of each data set (each channel), but could vary between data sets. The error introduced into the magnitude of the electric field due to variances in electrode placement is estimated to be ±4%.

Random thermal motion of the particles in the system is termed Brownian motion. Previously, the linear component was computed. It is repeated here for completeness and comparison to the rotational analysis. Values used in the calculation of Brownian motion are included in Table 8.2.

Table 8.2: Values used for Brownian motion calculations.

Boltzmann constat	k	1.38x10^{-23} kg m^2/s^2 K
Temperature	T	298 K
Viscosity	μ	1x10^{-3} kg/m s
Particle dimension	a	1x10^{-6} m
Time	t	0.06 s
Electrophoretic velocity	u	30x10^{-6} m/s

To calculate the linear Brownian motion, first calculate the translational diffusion coefficient:

$$D_{trans} = \frac{kT}{6\pi\mu a} = 2.18x10^{-13}m^2/s. \tag{8.11}$$

Next, calculate the average displacement squared (squared since the average displacement is zero):

$$< x^2 >= 6D_{trans}t = 7.85x10^{-14}m^2. \tag{8.12}$$

Finally, compute the Peclet number that compares electrophoretic velocity to translational Brownian motion:

$$Pe_{trans} = \frac{au}{D_{trans}} = 160. \tag{8.13}$$

The translational Brownian motion is 160 times smaller than the observed electrophoretic motion, so assuming translational Brownian motion is zero is reasonable.

To calculate the rotational Brownian motion, first calculate the rotational diffusion coefficient (for a long cylinder):

$$D_{rot} = \frac{3kT\ln(L/D)}{\pi\mu L^3} = 0.0881/s. \tag{8.14}$$

Next, compute the average rotation squared:

$$< s^2 >= 4D_{rot}t = 0.021 rad^2. \tag{8.15}$$

Finally, estimate the rotation:

$$< s^2 >^{1/2} = 0.146 rad = 8.3^\circ. \tag{8.16}$$

The estimated Brownian rotation over the time period between measurement frames is significant; it is of similar order to the measured changes in angle of the particles. Brownian rotation is random so the observed thermal rotation would not be 8.3 in practice, since the random rotation would occur equally in all directions. Brownian rotation does represent a significant source of error in the measured

motion of the particles because of its estimated magnitude.

8.6 Summary

Experimental observations of the motion of nanowires in PDMS channels that were smaller in size than the initial experiments of Ch. 3 and contained corner geometries were conducted. The use of commercially-purchased PSL fluorescent particles enabled accurate measurement of the zeta potential of the PDMS channel. The average bulk nanowire velocities observed agreed with theoretical predictions within 5.6%. The nanowires were observed to be rotating and translating across the channel as predicted numerically. The angle of the nanowires as they translated was found to be of opposite phase from the numerical predictions. It is theorized that this difference is a limitation of the 2D models. Although regardless of the phase of rotation, the primary result derived is the same the nanowires do not come to a steady state motion or location in the channel. The motion of nanowires through a 90° corner observed in these experiments exhibited the same alignment effect as present in the numerical models. The combined weight of these experimental measurements serve to verify the predictions made in the numerical models, thereby helping to assert that the numerical models are useful in predicting nanowire motion under electrokinetic forces.

Chapter 9

Induced Charge Electro-Osmosis (ICEO) for Particle Control

9.1 Introduction

The previous chapters have examined the physics governing the electrokinetic motion of non-spherical particles in microfluidic channels. Comparisons have been made to theoretical predictions in Chapters 3 and 8, the effects of the channels walls on the translational and rotational velocities were determined numerically in Chapters 4 and 5, and geometric channel elements examined as a means of impacting particle trajectory in Chapter 6. A next step for developing a microfluidic-based system for manipulating non-spherical particles is to exert control over the particle motion. DC electrokinetics has great potential as a means of bulk transport of nanowires, but has the drawback of acting on the bulk system. Induced-charge electroosmosis (ICEO) is examined here as a flexible means of exerting control over the motion of a particle or smaller groups of particles.

A key component for microfluidic-based particle manipulation is the ability to focus the particle into a desired region of the channel. A variety of means exist to accomplish this depending on the requirements of the system. Some methods such as hydrodynamic focusing (55), microvortex manipulation (56), or entropic separations (57) are effective in simple focusing of particles. These methods rely on fixed channel characteristics or flow conditions that limit their flexibility and consequently the range of particles or applications in which the focusing is effective. External forces can be used to aid in focusing including magnetic fields (58), acoustics (59), electric fields (60; 61) or optical forces (62; 63). A controllable external force can lead to a greater range of focusing functions, as well as allowing intermittent application.

In this chapter, induced-charge electroosmosis (ICEO) is investigated as a means of particle/flow focusing. ICEO is aptly named because the fluid motion is caused by the action of the electric field on the induced electrical double layer (EDL) surrounding a polarizable object. The phenomenon was originally termed ICEO by Bazant and Squires (64; 65) and is the generalization to any polarizable surface of "AC electroosmosis" which was observed at electrode surfaces in AC electric fields by Ramos et al. (50; 66) and Ajdari (67). Typically, ICEO results in recirculation regions surrounding a polarizable object. ICEO, and the resulting flow fields, have been proposed as a means of manipulating fluid flows in a corner, selecting flows in a T-junction, or as a means of fluid mixing (64). Here, ICEO is applied as a means of manipulating a flow in a microdevice for a specific purpose, such as focusing particles into a desired region of the channel. Multiple fixed conducting objects are precisely positioned in the microchannel so that the on/off

switchable ICEO flow field can be combined with a background pressure or DC electroosmotic flow to enable particle manipulation. Flexibility is a key component of this strategy, as the design of the conducting objects can be changed to produce devices with different levels of manipulation or different functions. The presence of the ICEO flow can be switched on and off rapidly because of its dependence on an applied AC electric field providing highly-controllable, intermittent particle manipulation.

9.2 Numerical Study

9.2.1 Theoretical Background

To illustrate ICEO fluid flow, consider the case of an electrically isolated, fixed metallic post in a fluid-filled microchannel. When an electric field is applied across the metallic post, the electrons within the post rearrange so that it is polarized. The accumulations of charges at the ends of the post attract oppositely charged ions in the surrounding fluid, which accumulate at the ends forming induced electrical double layers of opposite charges. The electric field acts on the induced EDL according to the same principles as DC electroosmosis, in that the ions in the diffuse part of the EDL move toward the oppositely charged electrode. However, in ICEO, the charges that are moving at each end of the post are doing so in opposite directions creating a flow pattern where the flow is directed toward the ends of the post and away from the post at its equator. The steady flow field that develops around an isolated post is a quadrapole arrangement of recirculation regions (65). An example flow field around an isolated post in shown in Fig. 9.1.

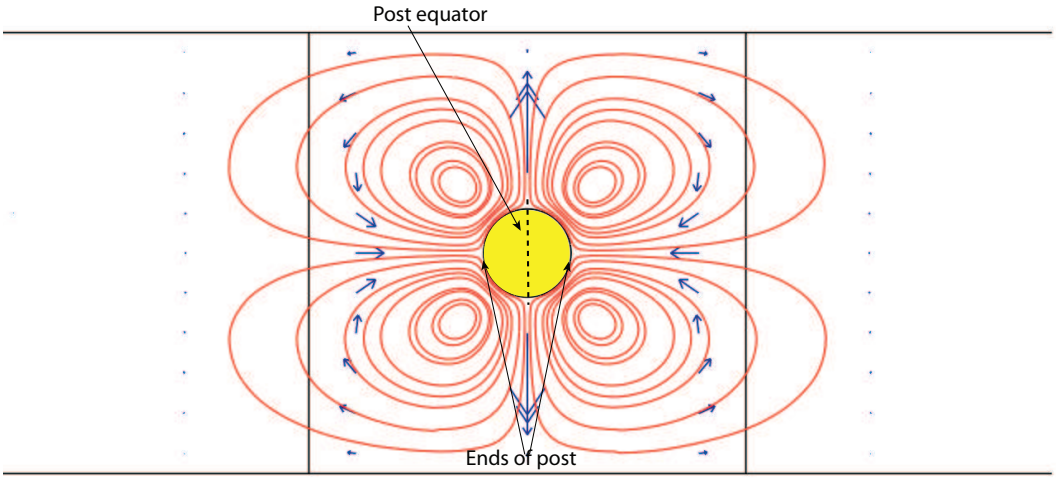

Figure 9.1: Fluid streamlines demonstrating the quadrapole arrangement of recirculation regions constituting ICEO flow around a conducting post under the action of an AC electric field.

When the electric field is reversed, such as the case of an applied AC signal, the polarization and consequently the EDLs that are induced will be oppositely charged. But since the electric field is also reversed, the ICEO flow pattern remains unchanged. In an AC electric field, the ICEO flow does not have to compete with standard DC electrokinetic motions, as they are suppressed in AC fields. Flexibility in flow patterns is achieved by combining regional AC-induced ICEO flow with a bulk background flow (driven by pressure or DC electroosmosis).

The mathematical model of the ICEO flow in Fig. 9.1 follows that presented in Levitan et al. (68) and is briefly summarized here. The assumption of thin electrical double layers simplifies the system, and is reasonable within the current physical system (EDL thickness of 10 nm around a post with a diameter of 100 μm. Thus the EDL is modeled as a thin capacitor in the electrical problem (68) and Laplace's equation can be solved for the electrical potential in the bulk outside the

EDL, ϕ,

$$\nabla^2\phi = 0. \tag{9.1}$$

The channel walls are non-polarizable and insulating so the boundary condition is zero normal current,

$$\mathbf{n} \cdot \nabla\phi = 0 \tag{9.2}$$

where $\mathbf{n}$ is the unit normal to the surface. The capacitive model of the EDL on the polarizable surface consists of two capacitors in series, a linear surface capacitor, C_s, based on Stern's model of the EDL and then a diffuse layer capacitor, C_d, from Gouy's EDL model (68). The effect of each capacitor is controlled by their ratio, $\delta = C_d/C_s$, which allows altering the model of the EDL from a diffuse Gouy-Chapman model to a surface Helmholtz model. This paramenter, δ, can also serve as a fitting parameter for matching the numerical models to experimental data in order to account for other factors (68; 69).

More complicated, nonlinear models for the induced EDLs exist, and can provide improved accuracy but are significantly more computationally intensive (70). Herein, the numerical models were used primarily to motivate and predict flows in actual devices, so the simpler more efficient model was utilized. The surface electrical boundary condition relates the bulk current to the capacitive charging of the EDL,

$$\sigma\mathbf{n} \cdot \nabla\phi = C_d\frac{\mathrm{d}\zeta}{\mathrm{d}t}. \tag{9.3}$$

The bulk conductivity, $\sigma = \varepsilon D/\lambda^2$, is determined by the permittivity of the solution, ε, diffusion constant, D, and the EDL thickness, λ. The diffuse capacitance is the ratio of the permittivity to the EDL thickness, $C_d = \varepsilon/\lambda$. The final component

of the boundary condition is the zeta potential, ζ, where unlike the DC case, is induced by the applied field and varies in space and time. The value of the induced zeta potential is determined by the voltage across the EDL,

$$\zeta = \frac{\phi_0 - \phi}{1 + \delta} \tag{9.4}$$

where ϕ is the potential in the bulk at the boundary with the EDL and ϕ_0 is the potential of the wire. In this case, the plain metallic wire has no native charge and it is not connected to any applied potential, therefore the post potential, ϕ_0, is the floating potential obtained based on the position of the post in the applied AC electric field.

Similarly, the fluid mechanics problem reduces to a matter of determining the impact of the induced flow at the surface on the bulk motion. The thin EDL approximation confines the induced electrokinetic motion to the EDL which represents a boundary condition to the bulk flow. Stokes equations govern the bulk fluid motion, $\mathbf{u}$, due to the low Reynolds number,

$$\nabla \cdot \mathbf{u} = 0 \tag{9.5}$$

$$\mu \nabla^2 \mathbf{u} = \nabla p \tag{9.6}$$

where η is the fluid viscosity and p is the pressure. The velocity boundary condition is the same as for DC electrokinetics,

$$u_{\|} = \frac{\varepsilon \zeta}{\mu} \nabla_{\|} \phi, \tag{9.7}$$

which defines the tangential fluid velocity at the surface given the fluid properties, zeta potential, and electric field. As opposed to DC electrokinetics, in ICEO flow the zeta potential is induced by and is a function of the applied electric field, creating a boundary condition that is second order in electrical potential, ϕ.

The ICEO flows under investigation are induced by AC electric fields and so the flow fields that develop vary with time. The desired frequency range of the AC electric fields is determined by examining the charging time of the EDLs in the system (68; 70). The charging time can be determined using characteristic distances that the ions travel to form the EDLs (λ, the EDL thickness and a, the characteristic length of the conducting post) and the rate at which ions move in the aqueous solution (D, the diffusion coefficient of the ions in solution): $\tau = \frac{\lambda a}{D}$. For the system under investigation, this results in a charging time of $\tau = 0.5$ ms. This charging time corresponds to a frequency of $\omega = (2\pi\tau)^{-1} = 318$ Hz. Applying an AC electric field with a frequency no higher than this value yields the optimal ICEO flow, as the EDLs have time to become fully charged resulting in the highest induced zeta potential. If the AC field is applied at a higher frequency, the ions do not have time to form the EDLs at the surface of the post, resulting in reduced fluid motion.

It is also possible to institute a lower limit to the applied frequency. Although ICEO flow is present in DC electric fields it can be of a reduced magnitude compared to the DC effects so applying a frequency that minimizes standard DC electrokinetics is beneficial. In the physical systems included here that can be accomplished with an AC electric field on the order of 50 Hz. This limit is derived from experimental observations of the motion of suspended particles which cease

reacting to the field at frequencies above 30 Hz. At frequencies above this point the fluid and particles in the channel do not have time to reach steady state velocities, which can be observed as the frequency where the particles stop vibrating and revert to random thermal motion. This establishes a set of bounds on the frequency of the applied AC electric field to be used in both the numerical and experimental investigations of 50-300 Hz. It has been theorized (71) and observed (72) that ICEO velocities decrease as the AC frequency is increased due to an increase in viscosity in the EDLs from a large concentration of ions. Therefore, the numerical and experimental tests were conducted with an AC frequency of 50 Hz.

9.2.2 Numerical Model

The basic microfluidic system under investigation, both numerically and experimentally, is presented schematically in Fig. 9.2. This represents a 2D slice out of

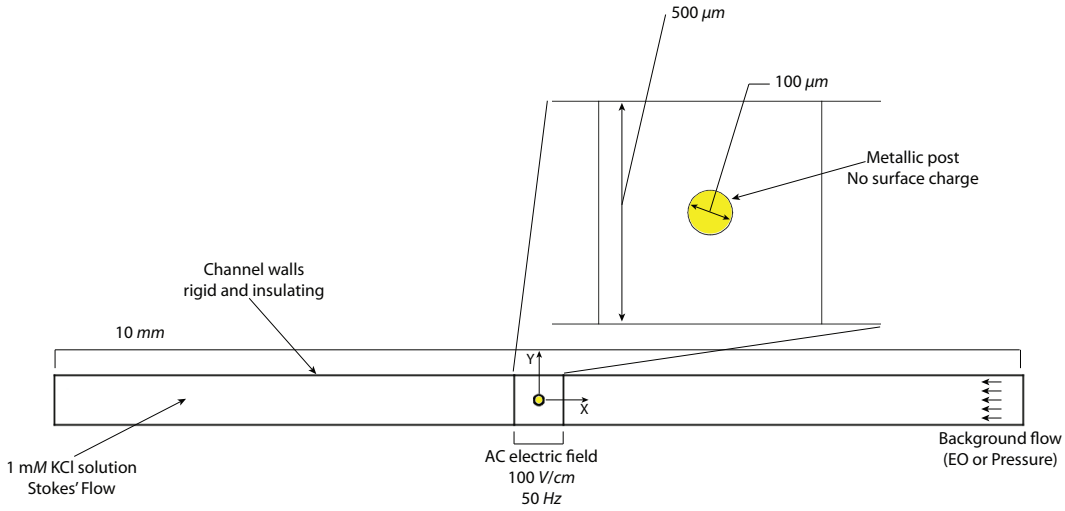

Figure 9.2: Schematic of a 2D slice out of the microfluidic channel used for ICEO flow. Relevant dimensions and system parameters indicated.

the center of the microfluidic channel so that the computational load is reduced.

The conducting post is located in the center of the channel. The two vertical lines near the post represent the electrodes which supply the AC electric field. A DC electric field is applied at the ends of the channel to produce a bulk flow. A pressure difference between the inlet and outlet would likewise create a bulk background flow in the system. The walls of the channel are assumed to be insulating and to carry a uniform negative zeta potential. The basic design of the device is for bulk fluid motion in the channel to move past a region of ICEO flow that acts on particles suspended in the bulk fluid. The number and positioning of the conducting posts in the channel determine the overall ICEO flow pattern, while the strength of the AC electric field determines the magnitude of the ICEO effect. The goal of the numerical investigation was to identify potential arrangements of posts for use in the experimental devices.

The system of equations has been successfully implemented to solve for time averaged ICEO flow using a commercial finite-element package, Comsol Multiphysics (Comsol AB, Burlington, MA). Application of an AC electric field creates a model that varies in time so the numerical model is solved transiently and the average velocity calculated directly. The model is set to run through at least 10 periods of the applied AC electric field, with a minimum of seven velocity measurements taken per period to eliminate aliasing. The mesh has a high density in the region of the conducting posts and expands to a lower density in the regions of the channel with unaffected background flow. The result of the model is the average fluid velocity field in the channel. It is possible to use a Fourier transformation to remove the need to solve the problem transiently and calculate the average flow (68). However, doing so necessitates the application of a sinusoidal electric field. The

current model allows for detailed analysis of the ICEO flow at all points in the applied AC electric field, as well as flexibility to explore additional waveforms that may emphasize particular transient behaviors. The additional flexibility of the current model comes with a manageable increase in computational expense.

9.2.3 Numerical Results

The average flow field for a microchannel with one post is shown in Fig. 9.3a. The majority of the channel illustrates bulk electroosmosis flow. This flow field demonstrates that a local ICEO region, and its associated AC electric field, does not affect the bulk flow in the system. This opens the possibility of integrating ICEO sections into existing microfluidic devices without interruption of the existing flow characteristics.

The details of the ICEO region around a single post are shown in Fig. 9.3b. The quadrapole pattern seen in the quiescent system is reduced to two recirculation regions on the trailing side of the post. The leading recirculation regions are largely acting in the direction of the oncoming bulk flow and so are absent. The recirculation region behind the post creates a space devoid of particles carried upstream after the ICEO region is created. This could be used to hold certain particles for a desired period of time for optical investigation or to release them at a later time for interaction with different particle carried by the bulk flow.

Potentially more interesting flow fields can be created with additional posts in the flow. Figure 9.3c contains the average flow field around a series of three conducting posts. With multiple posts in close proximity the ICEO flows that develop interact with those of other posts. The combined flow field indicated

here illustrates a potential flow focusing scenario. The incoming streamlines, from throughout the upstream channel, pass around the leading post and are compressed to pass between the remaining posts.

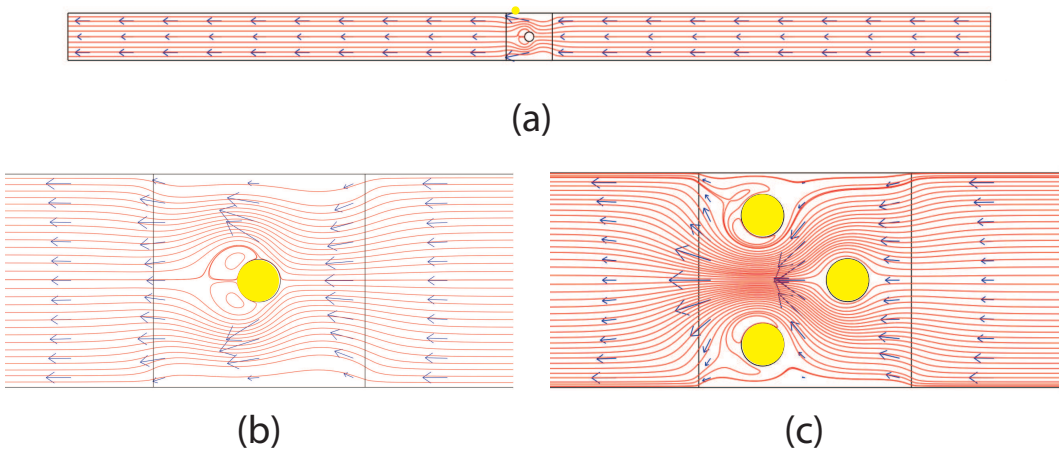

Figure 9.3: ICEO flow in a microfluidic channel. (a) Fluid streamlines detailing the fluid motion throughout the entire channel, demonstrating the ICEO flow region around the post does not impact the bulk fluid motion in the channel. (b) Fluid streamlines in the vicinity of the conducting post demonstrating the combination of ICEO flow and a background bulk flow. (c) A combination of conducting posts with interacting ICEO flows can create a flow field useful for flow focusing as illustrated by the fluid streamlines. Data from 2D numerical models.

9.3 Materials and Methods

9.3.1 Device Fabrication

A microchannel device containing conductive posts was fabricated in order to demonstrate the use of on-off switchable localized flow control. The fabrication process is shown in Fig. 9.4. A silicon wafer served as the base for the process, upon which a photolithographic pattern of microchannels containing fluid wells

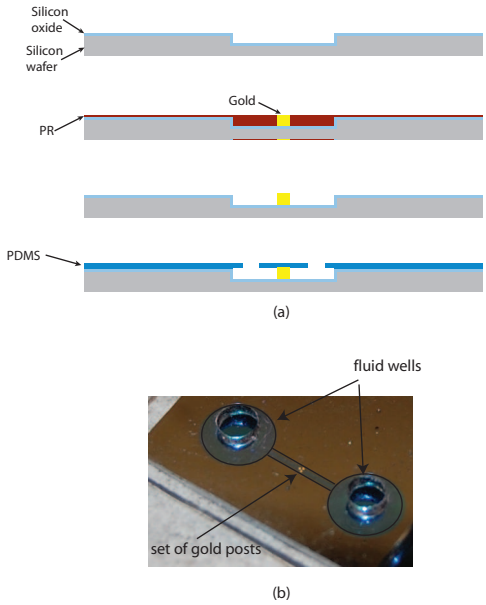

Figure 9.4: (a) Process flow diagram for the manufacture of a microfluidic channel containing gold posts. The gold posts are electrodeposited onto a silicon wafer through a photoresist mask. PDMS is used to cap the channels. (b) Image of the completed channel containing three gold posts. The fluid wells are located on either end of the channel and provide access for the fluid and application of the electrical field.

was applied using photoresist. A typical channel was 10 mm long with a width of 500 μm and a depth of 10 μm. The desired channels and wells were etched into the silicon wafer to a depth of 10 μm by deep reactive ion etching (DRIE). A layer of silicon dioxide was grown by thermal oxidation on the surface of the wafer to produce a similar surface to laboratory glass. A 50 nm layer of chrome and then 100 nm layer of gold were sputtered on the wafer to create a conductive seed layer. The seed layer provides the necessary conductive layer on the outside of the wafer for electrodeposition. Another layer of photoresist was applied and patterned everywhere except in the target post region. Electrodeposition was then used to grow the gold posts in their position. During electrodeposition a pro-

filometer was used frequently to ensure that the gold pillar structures do not exceed desired height. After the deposition process, the remaining gold and chrome seed layers were removed using gold and chrome etchant solvents, respectively, leaving a silicon dioxide channel structure containing gold posts. The wafer containing the channels and conductive post, was then capped by a PDMS sheet with access holes to allow addition of fluid to the wells. Utilizing this process, channels containing precisely sized and located conducting posts have been created (Fig. 9.5).

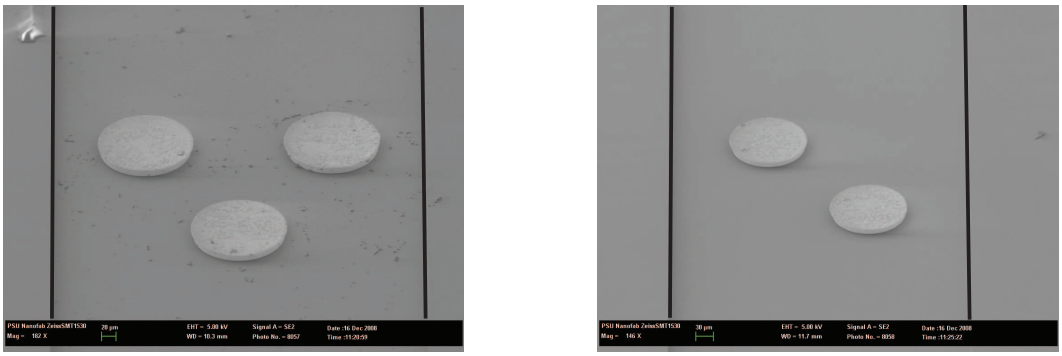

(a) (b)

Figure 9.5: SEM images of the microfluidic channels and the gold posts. (a) Image of a channel containing three posts. (b) Image of a channel containing two posts.

9.3.2 Experimental Setup

The working fluid for the experiments was a 1 mM KCl solution (140 μS/cm). The fluid was seeded with 1 μm fluorescent polystyrene particles (Invitrogen Corp., Carlsbad, CA.) to allow for visualization of the flow. The concentration of particles in the fluid was 0.02% by volume (0.02 gm particles in 100 mL solution). A function generator created a 10 V_{pp} sinusoidal signal at 50 Hz which was passed through an amplifier with a gain of 9x to increase its magnitude. The AC field was applied across the microchannel through platinum wires inserted into the fluid

wells. A small pressure difference existed between the two fluid wells creating a bulk pressure driven flow through the microchannel. A standard video microscopy system was used to record a series of images of the flow field for analysis. The images were captured at 33.33 frames per second (fps), where each image was 640 x 512 pixels, for 200-300 images.

The posts in the channel cause the electric field to be nonuniform, which could result in dielectrophoretic forces on the particles. The magnitude of dielectrophoretic velocity is $\frac{\varepsilon}{6\eta} r^2 \nabla |E|^2$ (73), where r is the particle radius (r = 0.5 μm). The magnitude of ICEO velocity is $\frac{\varepsilon}{\eta} E^2 a$, where a is the post radius (a = 50 μm). The ratio of dielectrophoresis to ICEO, $U_{DEP}/U_{ICEO} = r^2/a^2 = 10^{-4}$, is small so dielectrophoresis is negligible. The posts are larger than the particles so the nonuniformities in the electric field are small at the size scale of the particles.

9.3.3 Image Analysis

The captured images were analyzed using particle tracking software written in the IDL programming language (47). The initial step in analysis was to remove the background from the captured images. This process was carried out to remove the image of any particle that had adhered to the top or bottom surfaces. The pixel by pixel average image was computed for each group of captured images, which contained bright spots for the adhered particles since they did not move during the image capture. This average frame was subtracted from each frame in the stack to give images of only the particles that moved. Each frame was passed through a bandpass filter to highlight the particle images and the location of each particle identified. The locations of the particles in each successive frame was correlated,

and the paths of the particles tracked across the images to create streamlines. A series of images in Fig. 9.6 illustrate the basic analysis steps.

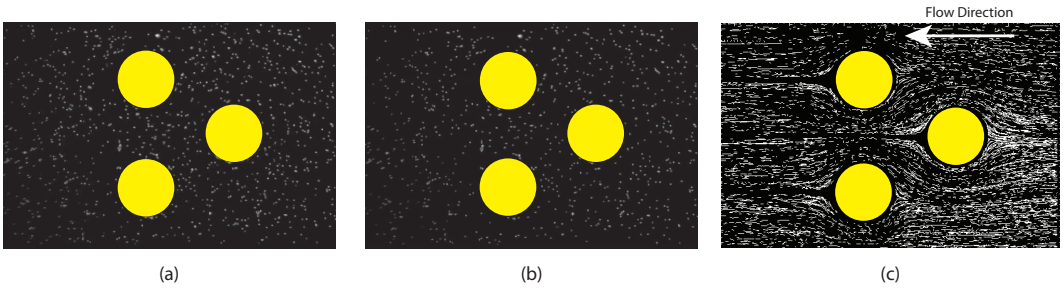

Figure 9.6: Series of images detailing the image analysis process. (a) Original image as captured by the camera. (b) Image after the background has been subtracted off to remove adhered particles. (c) Streamlines describing the fluid flow found by tracking the locations of the particles through the captured images.

9.4 Experimental Results

The streamlines observed for flow around the posts confirmed the presence of ICEO flow in the near post region. A comparison of the streamlines in the absence and presence of the AC electric field is presented in Fig. 9.7. The image of streamlines without the AC field (Fig. 9.7a) indicates Stokes' flow around the post. When the AC field is applied, the ICEO flow that develops around the post creates a recirculation region on the trailing side of the post that is indicated by a lack of streamlines (Fig. 9.7b). It is hypothesized that the streamlines are absent because the particles that are trapped in the recirculation region are brought close to the trailing edge of the post and held fixed, thus they are averaged out. Furthermore, the recirculation regions appear to be closed as no additional particles become entrapped in the region over the course of the experiment. This preliminary example indicates that ICEO flows may be capable of acting as particle traps.

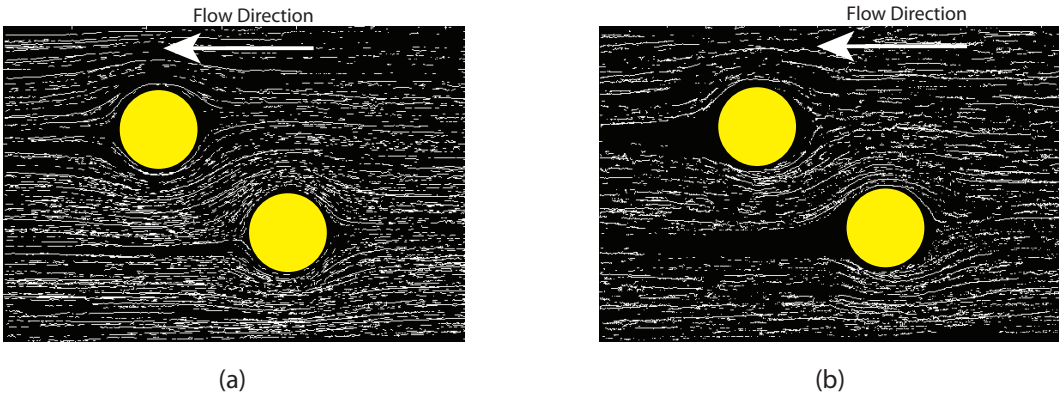

Figure 9.7: Streamline plots of flow around conducting posts. (a) Flow that exists when no AC electric field is applied. Stokes' flow is apparent. (b) Flow that exists in the presence of an AC electric field. Regions on the downstream side of the posts that are devoid of particles illustrate the effect of the ICEO flow generated around the posts.

A direct comparison of the numerical models to the experimental case is provided in Fig. 9.8. The numerical models cover both cases of applied background

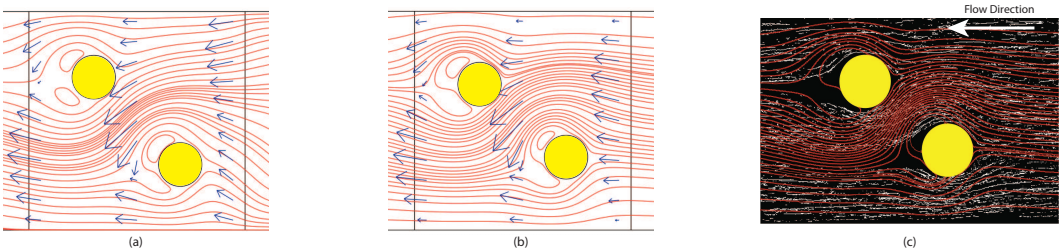

Figure 9.8: Comparison of the numerical models to the experimental results. (a) Fluid streamlines with DC electroosmosis for the bulk background flow. (b) Fluid streamlines with a pressure difference providing the background flow. (c) Fluid streamlines from the numerical model in b overlaid on the experimentally observed streamlines.

flow, a DC electroosomosis flow in Fig. 9.8a and a pressure driven flow in Fig. 9.8b. The fluid streamlines in the ICEO region illustrate a similar localized flow field regardless of the type of background flow. This result emphasizes that the type of background flow can be tailored to the specific microfluidic application without a

significant change to the ICEO-induced flow pattern.

The numerical fluid streamlines predict the presence of recirculation regions on the downstream side of the particle, while the upstream recirculation regions are absent. This appears to match the experimental results shown in Fig. 9.8c, where the numerical streamlines are superimposed on the experimental image. One aspect that is not represented in either of the numerical results is the void region that develops in the wake of the posts. The numerical models indicate that the recirculation regions are not completely closed, and so the immediate wake of the posts contains fluid streamlines from the upstream region. The wake region of the upper post in Fig. 9.8a contains closed recirculation regions and a small region void of upstream fluid lines. The present numerical models are matched, as precisely as possible, to the experimental results.

9.5 Next Steps

Over the course of conducting the ICEO experiments it became clear that the experimental apparatus and process were not optimized for best results. To that end, further development has begun seeking to improve the ability to exhibit, capture, and analyze ICEO flow data. The areas under improvement are the plumbing system for introducing the liquid into the channels, the particles present in the flow for visualization, the application of the electrical field, and the video capture method.

The method of manufacturing the channels containing conducting posts was successful in producing accurately placed posts of desired shape and size so no modifications have been made to that process. The means for introducing the

particle suspension into the channel and applying a bulk flow velocity to the liquid was improved. Previously, large wells were drilled through the capping layer to allow a large drop of suspension to be placed at each end of the channel. A difference in the volume of the drops produced a pressure difference leading to bulk flow past the conducting posts. In order to have more control over the bulk flow, the capping layer now contains two precision drilled holes over the wells at each end of the channel. One hole at each end receives a platinum wire for application of the electric field. The other hole at each end mates with a small tube which makes a pressure fit connection for introduction of the particle suspension. The edges of both holes are sealed with small amounts of epoxy to provide a pressure tight channel. The particle suspension is introduced to the channel by injecting fluid along the tube at one end from a syringe. A syringe pump in push/pull configuration (two syringes are moved by the pump in opposite directions, one pushing fluid in one end and the other pulling from the other end) serves to control the flow of particles in the channel. In this way, the bulk flow of particles can start and stop at the desired times, and proceed at a programmed velocity.

The previous experiments use PSL fluorescent particle with 1 μm diameter that were previously available in the lab. In order to be certain that the particles are acting truly as tracers of the fluid flow, additional particles were obtained with diameters larger and smaller that 1 μm for comparison. Likewise, thought was given to the concentration of particles used in the experiment. Previous study of particulate flow in this document focused more on the motion of individual particles so the concentration was low. However, in examining ICEO flow, the average flow present is of interest so a higher concentration of particles is needed

to help visualize the components of the flow. Consequently, the concentration of particles to be used in the revised experiments is twice that of previous work.

A large limitation of the previous ICEO experiments was an inability to apply an electric voltage higher than 90 V_{pp} to the channel. This limitation existed because of the amplifier available. A new amplifier has be acquired with the capability to increase the applied voltage to 500 V_{pp}. This improvement allows the exploration of the whole range of voltages possible in the experiments because electrolysis of the water occurs before the limit of the amplifier.

The final means of improving the experimental apparatus lies in the video capture system. The camera was able to adequately capture bright images of the particles at frame rates exceeding 30 fps so no change was made. However, the computer used to collect the video data as replaced with a newer more capable model. The change in computers allows for capturing longer segments of experimental data due to its increased processing and memory capabilities. With the older computer, capturing longer video streams, than the standard 50 frames, resulted in dropped frames and consequently holes in the video and an uncertainty of the true time events occurred. The new system allows capture of up to 500 frames, though 200-300 frames is more efficient because of the increasing time it takes to write the finished capture to disk. A longer video of the particle motion allows for more accurate study of the average flow pattern present in the channel. Additionally, the faster video capture allows for rapid start and stop of the video capture so it is easier to record transients in the flow as the electric field is started or stopped.

The improvements to the ICEO system have been implemented and the process

is being refined to enable more detailed study of the ICEO system. These new ICEO experiments will be reported by Shahrzad Yazdi in her subsequent degree documents and publications (49).

9.6 Summary

ICEO flows near conducting structures provide an on/off switchable means of manipulating fluid flow and particles in a microfluidic device. The applications to lab-on-a-chip technologies are many, including biological particle manipulation, the creation of materials, or fabrication. The method offers a variety of designs in setting up the desired flow field through different size, shapes, numbers, and locations of the conducting posts. The lithographic process used herein for creation of the posts has been developed and proven for fabricating devices capable of ICEO flow. Furthermore, the method contains the flexibility and precision to enable a wide range of design possibilities. The use of ICEO flow for particle manipulation provides additional flexibility in that it can be readily integrated into fluidic devices driven by pressure or DC electroosmosis. ICEO flows are driven by the application of an AC electric field and so can provide intermittent focusing effects or a varied strength of effect by cycling the field or altering its magnitude. The effective numerical models and successful observation demonstrate the promising nature of ICEO for particle manipulation.

Chapter 10

Summary and Implications

The goals of the current work were, first, to understand the electrokinetic motion of nanowires in microfluidic channels. Progress continued by attempting to calculate and predict the velocities in varying conditions. Finally, it was desired to be able to exert some measure of control over the velocities or positions of the nanowires within the microfluidic channels. The series of experimental and numerical studies conducted as part of this investigation were used to address and answer these goals.

10.1 Preliminary Experiments

The initial experiments intended to examine the electrokinetic velocities of nanowires in microfluidic channels. The experimental setup was refined during the process and provided improved results that agreed with theoretical predictions. However, the primary result of these experiments was the identification of key variables for further study.

10.2 Channel Wall Boundary Effects

Detailed investigations into the behavior of nanowires moving under electrokinetic forces were carried out both numerically and experimentally. Initially, numerical studies were constructed to investigate the effects of altering key parameters of interest. Nanowires are obviously non-spherical, so the angle of the nanowire with respect to the electric field was a key parameter and a difference from previous studies in the area. The angle of the nanowire to the electric field influenced the velocity with which it translated along the channel, as the velocity was reduced as the angle (from aligned) was increased. Similarly, the position of the particle within the microfluidic channel was found to have an impact on its velocity. As the size of the channel was reduced, the nanowire velocity decreased. However, if the channel was large and the nanowire was close to one wall its velocity could increase from the increase in electric field strength between the nanowire and the wall. The numerical studies also demonstrated that the path of the nanowire was not straight or fixed as it progresses through the channel. As the nanowire translates along the channel, its angle was changing as it translated in the perpendicular direction to the flow. The trajectories of the nanowires continued to oscillate without decaying to any steady-state path, negating the possibility of alignment through prolonged electrokinetic translation.

The exploration of the nanowire motion through straight channels continued into revised and improved experiments in an attempt to verify the numerical predictions. Experimental observations of the effect of one near wall were not possible because the nanowires do not approach a wall close enough for the effect to be significant. This was determined through a confocal microscopy study that deter-

mined the equilibrium point, between gravity and electrostatic repulsion, in the channel where the particles reside. Experimental observations did demonstrate that the nanowires rotate and translate through the width of the channel while translating along its width. The angle of the nanowires appears to be different than indicated numerically, but the result reinforces the notion that the nanowires do not reach a steady state translation. The agreement between the numerical and experimental results indicates that the numerical models do have predictive capabilities within a reasonable set of system parameters. Future exploration in these topics could focus on accurate determination of the zeta potential of the gold nanowires, which would improve the accuracy of the numerical models. It would also be interesting to design systems with different combinations of wall and particle zeta potentials for further control of the translational velocity of the nanowires.

10.3 Control Implications of a 90° Corner

Studies were conducted that looked at the behavior of nanowires when passing through geometries common in microfluidic structures. Interesting results were obtained when nanowires were moved through a 90° corner. The non-uniform electric and fluid fields present in the corner caused the nanowires that passed through the corner to exit at an angle close to parallel with the channel direction. A corner structure in a microfluidic system could act as a passive control element by assisting in aligning nanowires that travel through. The results of experimental studies of motion in a 90° corner agree closely with the numerical predictions verifying the alignment aid provided by the corner. The results are tempered by

the fact that the alignment effect is limited to a small region near the corner, as the nanowire will continue to rotate and translate once it is traveling along the straight channel after the corner.

10.4 Use of Induced-Charge Electroosmosis

The combination of numerical and experimental studies helped to develop an understanding of the electrokinetic system and provided theoretical and numerical models for predicting nanowire motion in microfluidic channels. ICEO was examined as a means to exert an element of control on the motion of the nanowires in the channel. Numerical models were used to explore the parameter space and test out designs for the control elements located in the flow. Results of initial experiments indicate that ICEO can occur in the systems of interest, but that the process still needs optimization. A revised and improved experimental apparatus is currently testing, with the hope of enabling the control elements demonstrated numerically. Possible uses for ICEO flows are diverse, but a primary goal is flow focusing. The ability to have on/off control of flow patterns that can focus streams of particles into selected locations is a desirable goal and useful in many micro/nanoparticle manufacturing systems or bio-particle identification schemes.

Appendix A

Electrorotation

A.1 Experimental Setup

The rotation of populations of nanowires, suspended in an aqueous solution, was examined in this series of experiments. The populations of nanowires were manufactured in the same manner as in Sec. 3.3, with lengths of 5 to 8 μm and no surface coating. The rotating electric field was applied through two pairs of electrodes set up at the edges of a square experimental window. The electrode design is shown in Fig. A.1. The electrodes were gold deposited onto a glass microscope slide. The edges of the of the electrodes are 0.5 mm apart and are flat at a right angle to the experimental space. This arrangement can lead to an uneven electric field which is much stronger in the region near the corners of the electrodes due to closer spacing. This can be countered with more complicated electrode design such as rounded electrode tips (74; 75) or a 'bone' design (76). The lack of advanced electrode design limited the valid experimental results to a small region in the center of the electrode pattern.

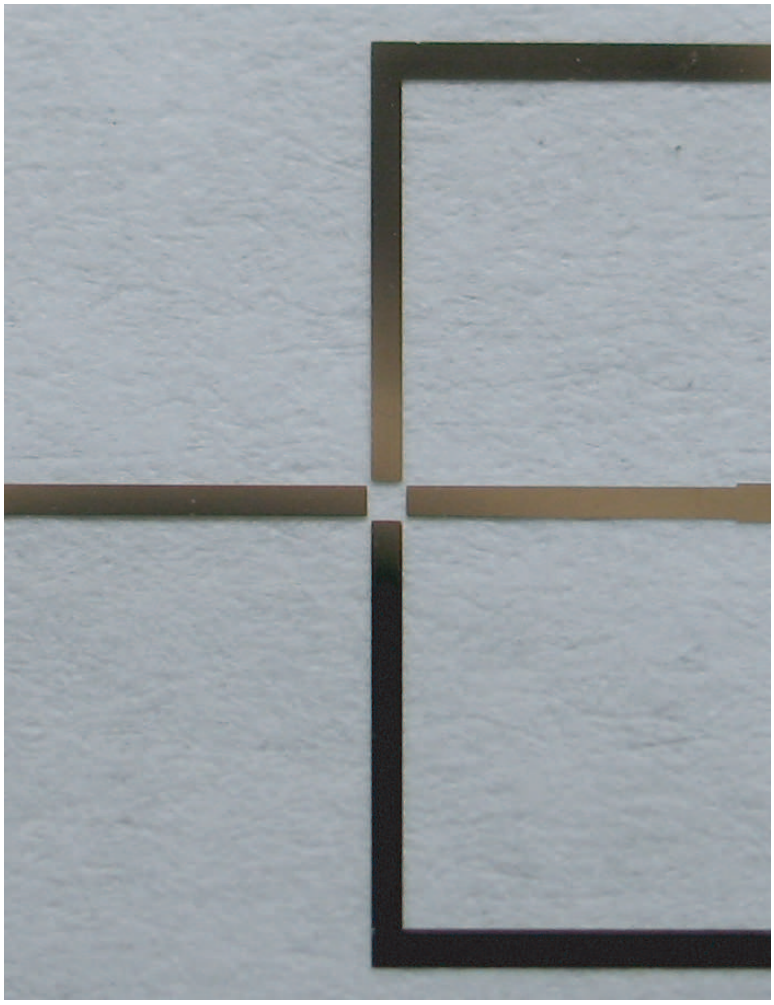

Figure A.1: Quadrature electrode design for application of a rotating electric field.

The electric field applied to cause rotation consisted of two sine waves at the same frequency with a phase difference of 90°. Each sine wave was generated by an independent function generator. The two function generators were linked to ensure the phase difference was precisely maintained. The amplitude of the applied sine waves was 10 Vpp and the applied frequency was varied from 300 to 17,500 Hz. Video movies of the nanowire rotation were collected at each applied frequency at 15 frames/s, which was an order of magnitude faster than rotation rates observed

using dark field microscopy. The videos were analyzed by hand to determine the rotation rate at each applied frequency by taking an average of the rotations of multiple wires in the center of the field.

A.2 Results and Discussion

The experimental results are presented in Table A.1 for the range of frequencies at which rotation was observed. The sign convention for the direction of nanowire rotation is positive for counter-clockwise rotation and negative for clockwise rotation. The qualitative behavior of the electrorotation results is in agreement with

Table A.1: Effect of applied frequency on rate and direction of nanowire rotation.

Applied Frequency (Hz)	Nanowire Rotation (Hz)
300	0.127
500	0.139
750	-0.364
1,000	-0.417
2,500	0.539
5,000	0.404
7,500	0.722
10,000	0.537
12,500	-0.345
15,000	-1.062
17,500	-0.987

published results (76; 77), in that the direction of rotation can change and that the rate of rotation increases with frequency. A precise theoretical model was not developed for this case due to lack of complex permittivities for a conducting particle, in this case a gold nanowire. Discussions with Prof. Boris Khusid from

the New Jersey Institute of Technology have indicated it might be possible, with some difficulty, to modify the dielectric relaxation spectroscopy (DRS) method to determine the complex permittivity of the gold nanowires.

Appendix B

Model of Steady State Motion using Comsol

The Comsol model below calculates the steady state velocity of a cylindrical particle in a cylindrical channel in three dimensions. An iterative method is used to calculate the particle velocity where the sum of the forces in the x-direction (direction along the channel) goes to zero. The angle of the particle and its position in the channel are variables that can be altered. This code was used to produce the steady state results in Chapter 4.

```
% Steady Electrokinetic motion of a non-spherical particle in a fluid
% filled channel.

% Author:  Scott M Davison 2009
% Dr. Kendra Sharp
% Microscale Flow Laboratory
% Dept of Mechanical and Nuclear Engineering
% Penn State University

% Purpose:  This script computes the steady state velocity of a
% non-spherical particle undergoing electrokinetic motion.  The
% motion of the particle is transferred to the walls, so the particle
% is held fixed.  The script iteratively solves for zero force in
```

```
% the x-direction signifing steady state.

% Output:  The program solves for the final steady state velocity
% in the x-direction as well as the sum of the forces and torques
% on the particle in all three directions.

% COMSOL Multiphysics Model M-file
% Generated by COMSOL 3.2a (COMSOL 3.2.0.300,
% $Date: 2005/12/20 19:02:30 $)

% This script was written in version 3.2, but has been tested on
% versions 3.3 and 3.4.  It is not compatible with version 3.5.


flclear fem
close all
clear all

% Start Clock to measure solution time
t1 = clock;

% COMSOL version
clear vrsn
vrsn.name = 'COMSOL 3.2';
vrsn.ext = 'a';
vrsn.major = 0;
vrsn.build = 300;
vrsn.rcs = '$Name:  $';
vrsn.date = '$Date: 2005/12/20 19:02:30 $';
fem.version = vrsn;

% Constants
% The constants are non-dimensionalized in this solution
% The constants are included before the geometry since so variables
%   for the particle angle and position can be set
% ep : permittivity of the solution
% zetP: zeta potential of the particle
% zetW: zeta potential of the channel walls
% V1: voltage applied to the channel, divided by phi for non-dim
% V2: voltage at other end of the channel, zero in most cases
% rho: density of the solution
% eta: viscosity of the solution
% k1: conductivity of the solution
% Uin: velocity in the channel in the z-direction
% rt: angle (in deg) of the particle from the z-direction
```

```
% rad: angle rt in radians
% radc: offset distance for placing the spheres on the cylinder
% rads: offset distance for placing the spheres on the cylinder
% L: characteristic length of the problem
% Ex: characterisitic electric field
% phi: characteristic voltage
% Uinf: characteristic velocity of the problem, represents the
%   velocity of the particle in an unbounded environment
% Re: Reynolds number
% Offset: non-dim distance from the center of the channel where
%   the particle is located.
% Gamma: ratio of the zeta potentials needed for the non-dim equations
fem.const = {'ep','80*8.854e-12', ...
   'zetP','-80e-3', ...
   'zetW','-30e-3', ...
   'V1','.0525/phi', ...
   'V2','0/phi', ...
   'rho','1000', ...
   'eta','1.003e-3', ...
   'k1','0.01', ...
   'Uin','.625', ...
   'rt','45', ...
   'rad','rt*pi/180', ...
   'radc','6e-6*cos(rad)', ...
   'rads','6e-6*sin(rad)', ...
   'L','1.5e-6', ...
   'Ex','500', ...
   'phi','Ex*L', ...
   'Uinf','-ep*(zetP)*Ex/eta', ...
   'Re','rho*Uinf*L/eta', ...
   'Offset','25', ...
   'Gamma','zetW/zetP'};

% Geometry
% A long cylinder represents the channel.  The particle is made up
% of a small cylinder with spheres on each end to remove sharp
% corners.
g4=cylinder3('35','70','pos',{'-35','0','0'},'axis',{'1','0','0'}, ...
     'rot','0','const',fem.const);
g9=cylinder3('1','4','pos',{'(-radc/2)/L','-Offset+(-rads/2)/L', ...
     '0'},'axis',{'radc','rads','0'},'rot','0','const',fem.const);
g1=sphere3('(1.5e-6)/L','pos',{'(-radc/2)/L','-Offset+(-rads/2)/L', ...
     '0'},'axis',{'radc','rads','0'},'rot','0','const',fem.const);
g2=sphere3('(1.5e-6)/L','pos',{'(radc/2)/L','-Offset+(rads/2)/L', ...
     '0'},'axis',{'radc','rads','0'},'rot','0','const',fem.const);
```

```
g3=geomcomp({g9,g1,g2},'ns',{'g9','g1','g2'},'sf','g9+g1+g2', ...
    'face','none','edge','all');
g5=geomdel(g3);
g6=geomcomp({g4,g5},'ns',{'g4','g5'},'sf','g4-g5','face','none', ...
    'edge','all');
clear s
s.objs={g6};
s.name={'CO1'};
s.tags={'g6'};

fem.draw=struct('s',s);
fem.geom=geomcsg(fem);

% Initialize mesh
fem.mesh=meshinit(fem, ...
                  'hmaxfact',1.5, ...
                  'hcurve',0.7, ...
                  'hgrad',1.2, ...
                  'hcutoff',0.04, ...
                  'hnarrow',2, ...
                  'hpnt',50, ...
                  'hmaxfac',[6,.4,7,.4,8,.4,9,.4,10,.4,11,.4,12, ...
                  .4,13,.4,14,.4,15,.4,16,.4,17,.4]);

% Initialize Loop Variables
% Sumx goes to zero when steady state is reached.  Governing equations
%   are linear so two values of u are tried, and the final valued
%   determined by interpolating.
Sumx = [1,1,1];
u(1) = .25;
u(2) = .55;
u(3) = 1;

% Loop to solve all three times
for i = 1:3

% Find final velocity
if i ==3
    u(i) = u(1)-Sumx(1)*(u(2)-u(1))/(Sumx(2)-Sumx(1));
end

% Constants are repeated since the value of Uin needs to change
fem.const = {'ep','80*8.854e-12', ...
  'zetP','-80e-3', ...
  'zetW','-30e-3', ...
```

```
    'V1','.0525/phi', ...
    'V2','0/phi', ...
    'rho','1000', ...
    'eta','1.003e-3', ...
    'k1','0.01', ...
    'Uin',u(i), ...
    'rt','45', ...
    'rad','rt*pi/180', ...
    'radc','6e-6*cos(rad)', ...
    'rads','6e-6*sin(rad)', ...
    'L','1.5e-6', ...
    'Ex','500', ...
    'phi','Ex*L', ...
    'Uinf','-ep*(zetP)*Ex/eta', ...
    'Re','rho*Uinf*L/eta', ...
    'Offset','25', ...
    'Gamma','zetW/zetP'};

% Application mode 1
% Stokes' equations used to solve for the fluid motion
clear appl
appl.mode.class = 'FlNavierStokes';
appl.shape = {'shlag(2,''lm1'')','shlag(2,''lm2'')', ...
    'shlag(2,''lm3'')','shlag(2,''u'')','shlag(2,''v'')', ...
    'shlag(2,''w'')','shlag(1,''p'')'};
appl.gporder = {4,2};
appl.cporder = {2,1};
appl.assignsuffix = '_ns';
clear prop
prop.analysis='static';
clear weakconstr
weakconstr.value = 'non-ideal';
weakconstr.dim = {'lm1','lm2','lm3'};
prop.weakconstr = weakconstr;
appl.prop = prop;
clear bnd
bnd.u0 = {'WallUx',0,0,'PartUx'};
bnd.type = {'uv','neutral','out','uv'};
bnd.wcgporder = 1;
bnd.w0 = {'WallUz',0,0,'PartUz'};
bnd.wcshape = [1;2;3];
bnd.v0 = {'WallUy',0,0,'PartUy'};
bnd.ind = [2,1,1,1,1,4,4,4,4,4,4,4,4,4,4,4,3];
appl.bnd = bnd;
clear equ
```

```
equ.shape = [4;5;6;7];
equ.rho = '0';
equ.eta = '1';
equ.cporder = {{1;1;1;2}};
equ.gporder = {{1;1;1;2}};
equ.ind = [1];
appl.equ = equ;
fem.appl{1} = appl;

% Application mode 2
% Computes the electric field in the channel
clear appl
appl.mode.class = 'ConductiveMediaDC';
appl.assignsuffix = '_dc';
clear prop
clear weakconstr
weakconstr.value = 'off';
weakconstr.dim = {'lm4'};
prop.weakconstr = weakconstr;
appl.prop = prop;
clear bnd
bnd.V0 = {0,'V1','V2'};
bnd.type = {'nJ0','V','V'};
bnd.ind = [2,1,1,1,1,1,1,1,1,1,1,1,1,1,1,1,3];
appl.bnd = bnd;
clear equ
equ.sigma = 'k1';
equ.ind = [1];
appl.equ = equ;
fem.appl{2} = appl;
fem.frame = {'ref'};
fem.border = 1;
fem.outform = 'weak';

% Scalar expressions
% Expressions for the X, Y, and Z direction velocities of the particle
% and the channel walls
fem.expr = {'PartUx','tEx_dc', ...
  'PartUy','tEy_dc', ...
  'PartUz','tEz_dc', ...
  'WallUx','Uin+Gamma*tEx_dc', ...
  'WallUy','Gamma*tEy_dc', ...
  'WallUz','Gamma*tEz_dc'};

% Coupling variable elements
```

```
clear elemcpl
% Integration coupling variables
% Boundary coupling variables to calculate the torque and force on the
% particle.
clear elem
elem.elem = 'elcplscalar';
elem.g = {'1'};
src = cell(1,1);
clear bnd
bnd.expr = {{{},'-lm1'},{{},'-lm2'},{{},'-lm3'},{{}, ...
    'y*(-lm3)-z*(-lm2)'},{{},'z*(-lm1)-x*(-lm3)'},{{}, ...
    'x*(-lm2)-y*(-lm1)'}};
bnd.ipoints = {{{},'4'},{{},'4'},{{},'4'},{{},'4'},{{},'4'},{{},'4'}};
bnd.frame = {{{},'ref'},{{},'ref'},{{},'ref'},{{},'ref'}, ...
    {{},'ref'},{{},'ref'}};
bnd.ind = {{'1','2','3','4','5','18'},{'6','7','8','9','10', ...
    '11','12','13','14','15','16','17'}};
src{1} = {{},{},bnd,{}};
elem.src = src;
geomdim = cell(1,1);
geomdim{1} = {};
elem.geomdim = geomdim;
elem.var = {'Sumx','Sumy','Sumz','Torx','Tory','Torz'};
elem.global = {'1','2','3','4','5','6'};
elemcpl{1} = elem;
fem.elemcpl = elemcpl;

% Multiphysics
fem=multiphysics(fem);

% Extend mesh
fem.xmesh=meshextend(fem);

% Solve problem
% The electrical problem decouples from the fluid problem so it is
% solved first to speed the solution
fem.sol=femnlin(fem, ...
                'solcomp',{'V'}, ...
                'outcomp',{'V'}, ...
                'linsolver','gmres', ...
                'prepar',{'droptol',0.1}, ...
                'uscale','none');
fem0=fem;

fem.sol=femnlin(fem, ...
```

```
                    'init',fem0.sol, ...
                    'solcomp',{'w','lm3','u','p','lm2','lm1','v'}, ...
                    'outcomp',{'w','lm3','u','lm2','p','lm1','v','V'}, ...
                    'hnlin','on', ...
                    'linsolver','gmres', ...
                    'prepar',{'droptol',0.05}, ...
                    'uscale','none');
fem1=fem;

% Get Values of Sumx from solution
Sumx(i) = postinterp(fem,'Sumx',[-20;0;0]);


end  % Convergence Loop

% Save fem to file
flsave Asym10 fem


% Test for equilibrium
% This section computes the x-direction force on each surface of
% the particle and totals the number of faces with positive and
% negative forces.  It is not strictly necessary, but can be a
% useful check on the results.
Npos = 0;
Nneg = 0;

I1=postint(fem,'-lm1', ...
             'dl',[6], ...
             'edim',2);
if I1 > 0
    Npos = Npos + 1;
else
    Nneg = Nneg + 1;
end

I2=postint(fem,'-lm1', ...
             'dl',[7], ...
             'edim',2);
if I2 > 0
    Npos = Npos + 1;
else
    Nneg = Nneg + 1;
end
```

```
I3=postint(fem,'-lm1', ...
                'dl',[8], ...
                'edim',2);
if I3 > 0
    Npos = Npos + 1;
else
    Nneg = Nneg + 1;
end

I4=postint(fem,'-lm1', ...
                'dl',[9], ...
                'edim',2);
if I4 > 0
    Npos = Npos + 1;
else
    Nneg = Nneg + 1;
end

I5=postint(fem,'-lm1', ...
                'dl',[10], ...
                'edim',2);
if I5 > 0
    Npos = Npos + 1;
else
    Nneg = Nneg + 1;
end

I6=postint(fem,'-lm1', ...
                'dl',[11], ...
                'edim',2);
if I6 > 0
    Npos = Npos + 1;
else
    Nneg = Nneg + 1;
end

I7=postint(fem,'-lm1', ...
                'dl',[12], ...
                'edim',2);
if I7 > 0
    Npos = Npos + 1;
else
    Nneg = Nneg + 1;
end
```

```
I8=postint(fem,'-lm1', ...
              'dl',[13], ...
              'edim',2);
if I8 > 0
    Npos = Npos + 1;
else
    Nneg = Nneg + 1;
end

I9=postint(fem,'-lm1', ...
              'dl',[14], ...
              'edim',2);
if I9 > 0
    Npos = Npos + 1;
else
    Nneg = Nneg + 1;
end

I10=postint(fem,'-lm1', ...
              'dl',[15], ...
              'edim',2);
if I10 > 0
    Npos = Npos + 1;
else
    Nneg = Nneg + 1;
end

I11=postint(fem,'-lm1', ...
              'dl',[16], ...
              'edim',2);
if I11 > 0
    Npos = Npos + 1;
else
    Nneg = Nneg + 1;
end

I12=postint(fem,'-lm1', ...
              'dl',[17], ...
              'edim',2);
if I12 > 0
    Npos = Npos + 1;
else
    Nneg = Nneg + 1;
end
```

```
% Stop Clock
t2 = etime(clock, t1);

% Get values of all quantities
Sumx = postinterp(fem,'Sumx',[-20;0;0]);
Sumy = postinterp(fem,'Sumy',[-20;0;0]);
Sumz = postinterp(fem,'Sumz',[-20;0;0]);
Torx = postinterp(fem,'Torx',[-20;0;0]);
Tory = postinterp(fem,'Tory',[-20;0;0]);
Torz = postinterp(fem,'Torz',[-20;0;0]);


% Open file
fid = fopen('Asym10out','w+');

% Print results to data file
fprintf(fid,'\nuf = %+10.8e\n',u(3));
fprintf(fid,'Npos = %2g\n',Npos);
fprintf(fid,'Nneg = %2g\n',Nneg);
fprintf(fid,'Elapsed Time = %8.5f\n\n',t2);
fprintf(fid,'Sumx = %+10.8e\n',Sumx);
fprintf(fid,'Sumy = %+10.8e\n',Sumy);
fprintf(fid,'Sumz = %+10.8e\n',Sumz);
fprintf(fid,'Torx = %+10.8e\n',Torx);
fprintf(fid,'Tory = %+10.8e\n',Tory);
fprintf(fid,'Torz = %+10.8e\n',Torz);

% Close file
fclose(fid);
```

Appendix C

Model of Nonsteady Motion using Comsol

The Comsol model below calculates the motion of a cylindrical particle moving electrokinetically along a channel. A moving mesh is used to model the motion. The initial angle of the particle is a variable to be altered. The solution geometry is two dimension due to the computational resources required for model a long, nonsteady process. This code was used to produce the nonsteady results in Chapters 5 and 6.

```
% Electrokinetic motion of a non-spherical particle in a fluid filled
% channel.

% Author:  Scott M Davison 2009
% Dr. Kendra Sharp
% Microscale Flow Laboratory
% Dept of Mechanical and Nuclear Engineering
% Penn State University

% Purpose:  This script computes the electrokinetic motion of a
% non-spherical particle as it moves along a fluid filled
% microchannel.  An electric field is applied along the length of the
% channel causing the particle to move by electrophoresis and the
```

```
% aqueous, suspending fluid to move by electroosmosis.

% Output:  As the particle moves its velocities and displacements are
% recorded to text files.  A workspace variable is also saved which
% contains the variable "solution" a structure containing all the fem
% structures from the model.  The solution variable can be used to
% produce a movie of the motion of the particle, or to load individual
% fem structures for indepth post processing.

flclear fem
clear

% COMSOL Multiphysics Model M-file
% Generated by COMSOL 3.2b (COMSOL 3.2.0.304,
% Date: 2006/04/04 14:56:13 )

% This script was written in version 3.2, but has been tested on
% versions 3.3 and 3.4.  It is not compatible with version 3.5.

% Geometry
% A long rectangle represents the microchannel
% Circles are added to the ends of a small rectangle to represent the
% particle.  This eases the computational load due to the absence of
% sharp corners.
g2=rect2('210','10','base','center','pos',{'0','0'},'rot','0');
g4=rect2('4','2','base','center','pos',{'-90','0'},'rot','45');
g5=circ2('1','base','center','pos',{'-90+2*cos(45*pi/180)', ...
    '2*sin(45*pi/180)'},'rot','45');
g6=circ2('1','base','center','pos',{'-90-2*cos(45*pi/180)', ...
    '-2*sin(45*pi/180)'},'rot','45');
g7=geomcomp({g4,g5,g6},'ns',{'g4','g5','g6'},'sf','g4+g5+g6', ...
    'edge','none');
g8=geomcomp({g2,g7},'ns',{'g2','g7'},'sf','g2-g7','edge','none');
clear s
s.objs={g8};
s.name={'CO2'};
s.tags={'g8'};
fem.draw=struct('s',s);
fem.geom=geomcsg(fem);

% Constants
% The constants are nondimensionalized in this solution
% ep : permittivity of the solution
% zetW: zeta potential of the channel walls
% zetP: zeta potential of the particle
```

```
% V1: voltage applied to the channel, divided by phi for non-dim
% V2: voltage at other end of the channel, zero in most cases
% rho: density of the solution
% eta: viscosity of the solution
% k1: conductivity of the solution
% L: characteristic length of the problem
% Ex: characterisitic electric field
% phi: characteristic voltage
% Uinf: characteristic velocity of the problem, represents the
%   velocity of the particle in an unbounded environment
% Re: Reynolds number
% Vol: volume of the particle
% rhoP: density of the particle
% mass: mass of the particle
% m: non-dim mass of the particle
% Inertia: moment of inertia of the particle
% I: non-dim moment of inertia of the particle
% Xoffset: starting location in the X-direction of the particle,
%   used to calculate the displacement starting from zero
% Yoffset: starting location in the Y-direction of the particle,
%   used to calculate the displacement starting from zero
fem.const = {'ep','80*8.854e-12', ...
   'zetW','-30e-3', ...
   'zetP','-80e-3', ...
   'V1','.1575/phi', ...
   'V2','0/phi', ...
   'rho','1000', ...
   'eta','1.003e-3', ...
   'k1','0.01', ...
   'L','1.5e-6', ...
   'Ex','500', ...
   'phi','Ex*L', ...
   'Uinf','-ep*zetP*Ex/eta', ...
   'Re','rho*Uinf*L/eta', ...
   'Vol','pi*L^2*4*L+4/3*pi*L^3', ...
   'rhoP','2330', ...
   'mass','rhoP*Vol', ...
   'm','mass*Uinf/(eta*L^2)', ...
   'Inertia','1/4*mass*L^2+1/12*mass*(4*L)^2', ...
   'I','Inertia*Uinf/(eta*L^4)', ...
   'Xoffset','-90', ...
   'Yoffset','0'};

% Initialize mesh
fem.mesh=meshinit(fem, ...
```

```
                    'hnarrow',3, ...
                    'hpnt',20, ...
                    'hmaxedg', [4,.15,5,.15,7,.15,8,.15,9,.15,10,.15]);

% Application mode 1
% Calculates the motion of the particle based on its velocity
clear appl
appl.mode.class = 'MovingMesh';
appl.sdim = {'Xm','Ym','Zm'};
appl.shape = {'shlag(2,''lm1'')','shlag(2,''lm2'')', ...
    'shlag(2,''x'')','shlag(2,''y'')'};
appl.gporder = 4;
appl.cporder = 2;
appl.assignsuffix = '_ale';
clear prop
prop.smoothing='winslow';
prop.analysis='transient';
prop.allowremesh='on';
prop.origrefframe='ref';
appl.prop = prop;
clear bnd
bnd.defflag = {{1;1},{0;0}};
bnd.type = {'def','vel'};
bnd.veldefflag = {{0;0},{1;1}};
bnd.wcshape = [1;2];
bnd.veldeform = {{0;0},{'Up-omega*(y-Yoffset-dyp)'; ...
    'Vp+omega*(x-Xoffset-dxp)'}};
bnd.ind = [1,1,1,2,2,1,2,2,2,2];
appl.bnd = bnd;
clear equ
equ.shape = [3;4];
equ.ind = [1];
appl.equ = equ;
fem.appl{1} = appl;

% Application mode 2
% Governs the fluid motion in the channel
clear appl
appl.mode.class = 'FlNavierStokes';
appl.shape = {'shlag(2,''lm3'')','shlag(2,''lm4'')', ...
    'shlag(2,''u'')','shlag(2,''v'')','shlag(1,''p'')'};
appl.gporder = {4,2};
appl.cporder = {2,1};
appl.assignsuffix = '_ns';
clear prop
```

```
clear weakconstr
weakconstr.value = 'non-ideal';
weakconstr.dim = {'lm3','lm4','lm5'};
prop.weakconstr = weakconstr;
appl.prop = prop;
clear bnd
bnd.u0 = {0,'WallUx','PartUx',0};
bnd.type = {'out','uv','uv','neutral'};
bnd.wcgporder = 1;
bnd.wcshape = [1;2];
bnd.v0 = {0,'WallUy','PartUy',0};
bnd.ind = [1,2,2,3,3,4,3,3,3,3];
appl.bnd = bnd;
clear equ
equ.shape = [3;4;5];
equ.rho = 0;
equ.cporder = {{1;1;2}};
equ.gporder = {{1;1;2}};
equ.ind = [1];
appl.equ = equ;
fem.appl{2} = appl;

% Application mode 3
% Governs the electrical field in the channel
clear appl
appl.mode.class = 'ConductiveMediaDC';
appl.assignsuffix = '_dc';
clear prop
clear weakconstr
weakconstr.value = 'off';
weakconstr.dim = {'lm6'};
prop.weakconstr = weakconstr;
appl.prop = prop;
clear bnd
bnd.V0 = {0,'V1','V2'};
bnd.type = {'nJ0','V','V'};
bnd.ind = [3,1,1,1,1,2,1,1,1,1];
appl.bnd = bnd;
clear equ
equ.sigma = 'k1';
equ.ind = [1];
appl.equ = equ;
fem.appl{3} = appl;
fem.sdim = {{'Xm','Ym'},{'X','Y'},{'x','y'}};
fem.frame = {'mesh','ref','ale'};
```

```
fem.border = 1;
fem.units = 'SI';


% Scalar expressions
% Expressions for the X and Y direction velocities of the particle
% and the channel walls
fem.expr = {'PartUx','tEx_dc+Up-omega*(y-Yoffset-dyp)', ...
  'PartUy','tEy_dc+Vp+omega*(x-Xoffset-dxp)', ...
  'WallUx','zetW/zetP*tEx_dc', ...
  'WallUy','zetW/zetP*tEy_dc'};

% Coupling variable elements
clear elemcpl
% Integration coupling variables
% Boundary coupling variables to calculate the torque and force on the
% particle.
clear elem
elem.elem = 'elcplscalar';
elem.g = {'1'};
src = cell(1,1);
clear bnd
bnd.expr = {{{},'(x-Xoffset-dxp)*(-lm4)-(y-Yoffset-dyp)*(-lm3)'}, ...
    {{},'-lm3'},{{},'-lm4'}};
bnd.ipoints = {{{},'4'},{{},'4'},{{},'4'}};
bnd.frame = {{'mesh','mesh'},{'mesh','mesh'},{'mesh','mesh'}};
bnd.ind = {{'1','2','3','6'},{'4','5','7','8','9','10'}};
src{1} = {{},bnd,{}};
elem.src = src;
geomdim = cell(1,1);
geomdim{1} = {};
elem.geomdim = geomdim;
elem.var = {'Torz','Sumx','Sumy'};
elem.global = {'1','2','3'};
elem.maxvars = {};
elemcpl{1} = elem;
fem.elemcpl = elemcpl;

% ODE Settings
% ODEs used to solve Newton's second law to determine the velocity and
% subsequent displacements of the particle
clear ode
ode.dim={'Up','Vp','omega','dxp','dyp','dop'};
ode.f={'Sumx-m*Upt','Sumy-m*Vpt','Torz-I*omegat','Up-dxpt', ...
    'Vp-dypt','omega-dopt'};
```

```
ode.init={'0','0','0','0','0','0'};
ode.dinit={'0','0','0','0','0','0'};
fem.ode=ode;

% Multiphysics
fem=multiphysics(fem);

% Create Data files of velocities and displacments
fidUp = fopen('Up.txt','w+');
fidVp = fopen('Vp.txt','w+');
fidOm = fopen('Om.txt','w+');
fiddxp = fopen('dxp.txt','w+');
fiddyp = fopen('dyp.txt','w+');
fiddop = fopen('dop.txt','w+');

% Loop variables
% t_st: the time the previous mesh deformation stopped, so the files
%   are continuous in time
% dxp: displacement in the X-direction, used as a stop condition for
%   the loop
% i: counter variable
t_st = 0;
dxp = 0;
i = 1;

% Loop control (limit horizontal displacement)
while dxp < 180


% Extend mesh
fem.xmesh=meshextend(fem);

if i > 1
% Mapping current solution to extended mesh
init = asseminit(fem,'init',fem0.sol,'xmesh',fem0.xmesh, ...
    'framesrc','ale','domwise','on');
end

% Solve problem
if i == 1
fem.sol=femtime(fem, ...
                'symmetric','off', ...
                'solcomp',{'Up','p','lm1','V','lm4','v','dyp', ...
                'dxp','dop','omega','lm3','u','y','lm2','x','Vp'}, ...
                'outcomp',{'Up','p','lm1','V','lm4','v','dyp', ...
```

```
                'dxp','dop','omega','lm3','u','Y','y','lm2','x', ...
                'X','Vp'}, ...
                'tlist',[t_st:0.1:350], ...
                'tout','tlist', ...
                'tsteps','intermediate', ...
                'stopcond','minqual1_ale-0.1');
else
fem.sol=femtime(fem, ...
                'init',init, ...
                'symmetric','off', ...
                'solcomp',{'Up','p','lm1','V','lm4','v','dyp', ...
                'dxp','dop','omega','lm3','u','y','lm2','x','Vp'}, ...
                'outcomp',{'Up','p','lm1','V','lm4','v','dyp', ...
                'dxp','dop','omega','lm3','u','Y','y','lm2','x', ...
                'X','Vp'}, ...
                'tlist',[t_st:0.1:350], ...
                'tout','tlist', ...
                'tsteps','intermediate', ...
                'stopcond','minqual1_ale-0.1');
end

% Save current fem structure for restart purposes
fem0=fem;

% Save current fem for postprocessing purposes
solution{i}=fem;

% Get final time from solution
% Use a point where the particle can be located at any time point
% Here a position behind where the particle starts
t_st=postinterp(fem,'t',[-104;4]);

% Get velocities and displacments for all time values
data = postglobaleval(fem);

% Write velocities and displacments to file
leng = length(data.x);
for j = 2:leng
  fprintf(fidUp,'%15.5f %15.5f \n',data.x(j),data.y(j,1));
  fprintf(fidVp,'%15.5f %15.5f \n',data.x(j),data.y(j,2));
  fprintf(fidOm,'%15.5f %15.5f \n',data.x(j),data.y(j,3));
  fprintf(fiddxp,'%15.5f %15.5f \n',data.x(j),data.y(j,4));
  fprintf(fiddyp,'%15.5f %15.5f \n',data.x(j),data.y(j,5));
  fprintf(fiddop,'%15.5f %15.5f \n',data.x(j),data.y(j,6));
end
```

```
% Generate geom from mesh
fem = mesh2geom(fem, ...
                'srcdata','deformed', ...
                'frame','ale', ...
                'destfield',{'geom','mesh'}, ...
                'srcfem',1, ...
                'destfem',1, ...
                'srctags',{'g1','m1'});

% Initialize mesh
fem.mesh=meshinit(fem, ...
                  'hnarrow',3, ...
                  'hpnt',20, ...
                  'hmaxedg', [4,.15,5,.15,7,.15,8,.15,9,.15,10,.15]);

% Increment loop variable
dxp = data.y(leng,4);
i = i + 1;

% End loop
end

% Close data files
fclose(fidUp);
fclose(fidVp);
fclose(fidOm);
fclose(fiddxp);
fclose(fiddyp);
fclose(fiddop);
fclose('all');

% Save data for later use
save('Output.ws')

% Create movie from solution
%postmovie(solution,'Fps',50,'filename','MovieOut.avi','tridata', ...
% {'normE_dc','cont','internal'},'trimap','hot(1024)','geom', ...
% 'off','axis',[-35,10,-10,35,-1,1]);

close('all')
```

Appendix D

Hydrodynamic Analysis of a Needle-like Ellipsoid

The numerical simulations and the experimental results of the motion of a non-spherical particle in a long channel differ in the rotation of the particle as it translates. One means of reconciling the difference is to examine the purely hydrodynamic motion of a needle-shaped ellipsoid. The velocity and angle of motion of the ellipsoid can be calculated following the method in Sec. 5.7 and 5.9 of Happel and Brenner (7). The problem examined in the text is the steady state settling of a needle-shaped ellipsoid in quiescent fluid under the action of gravity. It is possible to frame the electrokinetic problem in such a way that it resembles the settling case. Since electroosmotic flow resembles plug flow, changing the reference frame for the electrokinetic problem to be moving with the fluid provides a frame where the fluid appears to be still with a particle moving through it. In this way, it is possible to provide a reasonable match between the purely hydrodynamic problem and the electrokinetic observations. A schematic diagram of the hydrodynamic

problem is included in Fig. D.1.

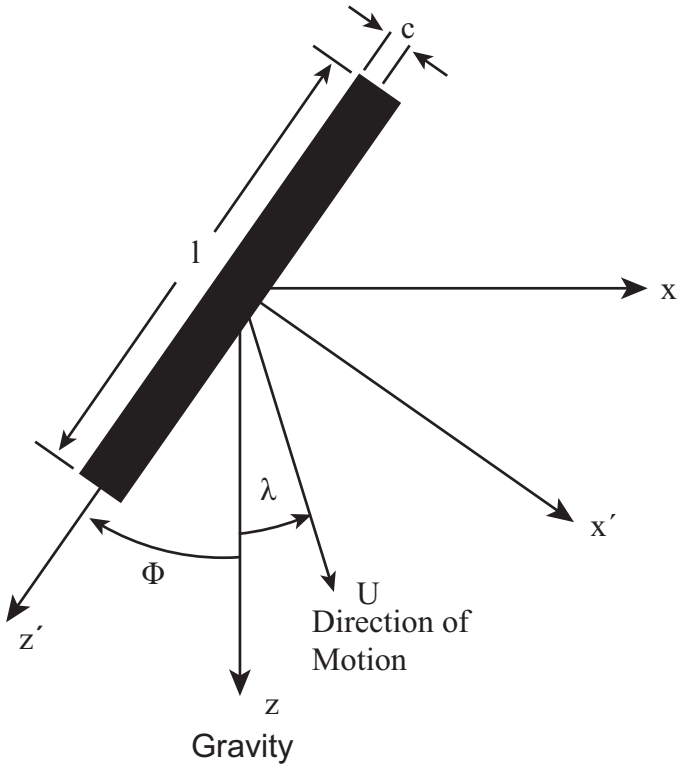

Figure D.1: Schematic diagram of a needle-shaped ellipsoid settling under the action of gravity. Diagram adapted from Happel and Brenner (7).

Using the coordinate system above, the direction cosines and principal translational resistance tensors for the geometry are derived. These terms can be substituted into the general equations, given as Eqn. 5-7.35 in Happel and Brenner (7). Simplified, the equations to solve for the motion of the particle are

$$(U_x)_\infty = \left(\frac{3}{2} - ln\frac{l}{c}\right)\frac{gc^2\Delta\rho}{8\mu}sin2\Phi \tag{D.1}$$

$$(U_y)_\infty = 0 \tag{D.2}$$

$$(U_z)_\infty = -\left(\frac{3}{2} - ln\frac{l}{c}\right)\frac{gc^2\Delta\rho}{8\mu}\left[\frac{(1/2) - 3ln(l/c)}{(3/2) - ln(l/c)} + cos2\Phi\right], \tag{D.3}$$

where l is the particle length, c is the particle radius, g is gravity, $\Delta\rho$ is the difference in density between the particle and the fluid, and μ is the fluid viscosity. Once the velocities in the x and z directions are known it is possible to calculate the direction of motion relative to the gravity vector

$$\lambda = tan^{-1}\left(\frac{(U_x)_\infty}{(U_z)_\infty}\right). \tag{D.4}$$

Using values from the experiments, l=5 μm, c=150 nm, g=9.8 m/s^2, $\Delta\rho$=18320 kg/m^3, and μ=1x10^{-3} Pa·s, the values for the velocities and directions were tabulated in Table D for selected angles.

Table D.1: Calculated values for the velocity in each direction and angle of motion for various angles

Φ	$(U_x)_\infty$	$(U_z)_\infty$	λ
deg	m/s x 10^{-6}	m/s x 10^{-6}	deg
0	0	6.07	0
15	-0.51	5.94	-4.88
30	-0.88	5.57	-8.96
45	-1.01	5.06	-11.3
60	-0.88	4.55	-10.9
75	-0.51	4.18	-6.92
90	0	4.05	0

The computed values of λ are zero or negative meaning that the particle in Fig. D.1 is moving down and to the left. Motion in this direction qualitatively matches the direction of the nanowire movement predicted numerically, the nanowires translate toward the leading tip. The experimental results demonstration motion toward the broad side of the nanowires, a direction that would correspond to a positive value of λ in this example. Since the hydrodynamic analysis

agrees with the numerical predictions, the interaction with the wall may be the cause of the motion towards the broad side of the nanowire in the experimental case.

Bibliography

[1] Probstein, R. (2003) *Physicochemical Hydrodynamics*, 2nd ed., Wiley Interscience, Hoboken, New Jersey.

[2] Shaw, D. J. (1980) *Introduction to Colloid and Surface Chemistry*, 3rd ed., Butterworths, London.

[3] Ye, C., X. Xuan, and D. Li (2005) "Eccentric Electrophoretic Motion of a Sphere in Circular Cylindrical Microchannels," *Microfluid. Nanofluid.*, **1**, pp. 234–241.

[4] Ye, C., D. Sinton, D. Erickson, and D. Li (2002) "Electrophoretic Motion of a Circular Cylindrical Particle in a Circular Cylindrical Microchannel," *Langmuir*, **18**, pp. 9095–9101.

[5] Liu, H., H. Bau, and H. Hu (2004) "Electrophoresis of Concentrically and Eccentrically Positioned Cylindrical Particles in a Long Tube," *Langmuir*, **20**, pp. 2628–2639.

[6] Keh, H. and J. Anderson (1985) "Boundary Effects on Electrophoretic Motion of Colloidal Spheres," *J. Fluid Mech.*, **153**, pp. 417–439.

[7] Happel, J. and H. Brenner (1983) *Low Reynolds Number Hydrodynamics*, Martinus Nijhoff Publishers, The Hague, The Netherlands.

[8] Hunter, R. (1981) *Zeta Potential in Colloid Science*, Academic Press, New York.

[9] Chen, L. J. (2007) "Silicon nanowires: the key building block for future electronic devices," *J. Mater. Chem.*, **17**, pp. 4639–4643.

[10] Lee, S., A. Umar, D. Suh, J. Park, Y. Hahn, J. Ahn, and S. Lee (2008) "The synthesis of ZnO nanowires and their subsequent use in high-current field-effect transistors formed by dieletrophoresis alignment," *Physica E*, **40**, pp. 866–872.

[11] Appell, D. (2002) "Nanotechnology: Wired for Success," *Nature*, **419**, pp. 553–555.

[12] Sadeghian, R. B. and M. Kahrizi (2007) "A novel miniature gas ionization sensor base on freestanding gold nanowires," *Sensor. Actuat. A-Phys*, **137**, pp. 248–255.

[13] Dai, D. and S. He (2008) "Ultrasmall integrated devices based on silicon nanowires for optical communications," *J. Nanophotonics*, **2**, p. 021780.

[14] Greytak, A., C. Barrelet, Y. Li, and C. Lieber (2005) "Semiconductor Nanowire Laser and Nanowire Waveguide Electro-optic Modulators," *Appl. Phys. Lett.*, **87**, p. 151103.

[15] Lee, S., M. Jeong, J. Myoung, G. Chae, and I. Chung (2007) "Magnetic alignment of ZnO nanowires for optoelectronic device applications," *Appl. Phys. Lett.*, **90**, p. 133115.

[16] Klemic, J., E. Stern, and M. Reed (2001) "Hotwiring Biosensors," *Nat. Biotechnol.*, **19**, pp. 924–925.

[17] Lee, J., K. Moon, M. Ham, and J. Myoung (2008) "Dielectrophoretic assembly of GaN nanowires for UV sensor applications," *Solid State Commun.*, **148**, pp. 194–198.

[18] Peng, K., J. Jie, W. Zhang, and S. Lee (2008) "Silicon nanowires for rechargeable lithium-ion battery anodes," *Appl. Phys. Lett.*, **93**, p. 033105.

[19] McQuarrie, D. (2000) *Statistical Mechanics*, University Science Books, Sausalito, CA.

[20] Minor, M., A. van der Linde, J. van Leeuwen, and J. Lyklema (1997) "Dynamic Aspects of Electrophoresis and Electroosmosis: A new Fast Method for Measuring Particle Mobilities," *J. Colloid Interface Sci.*, **189**, pp. 370–375.

[21] Henry, D. (1931) "The Cataphoresis of Suspended Particles. Part I: The Equation of Cataphoresis," *Proc. Roy. Soc.*, **A133**, pp. 106–129.

[22] Booth, F. (1948) "Surface conductance and cataphoresis," *T. Faraday Soc.*, **44**, pp. 955–959.

[23] Henry, D. (1948) "The electrophoresis of suspended particles. IV." *T. Faraday Soc.*, **44**, pp. 1021–1026.

[24] Russel, W. B., D. A. Saville, and W. R. Schowalter (1989) *Colloidal Dispersions*, Cambridge University Press, Cambridge.

[25] Wiersema, P., A. L. Loeb, and J. T. G. Overbeek (1966) "Calculation of the electrophoretic mobility of spherical colloid particle," *J. Colloid Interface Sci.*, **22**, pp. 78–99.

[26] Sharp, K., R. Adrian, J. Santiago, and J. Molho (2001) *CRC Handbook on MEMS*, CRC, Boca Raton, FL, pp. 6–17 – 6–32.

[27] Devasenathipathy, S., J. Santiago, and K. Takehara (2002) "Particle Tracking Techniques for Electrokinetic Microchannel Flows," *Anal. Chem.*, **74**, pp. 3704–3713.

[28] Stigter, D. (1978) "Electrophoresis of Highly Charged Colloidal Cylinders in Univalent Salt Solutions. 2. Random Orientation in External Field and Application to Polyelectrolytes," *J. Phys. Chem.*, **82**, pp. 1424–1429.

[29] Martin, C. (1996) "Membrane-Based Synthesis of Nanomaterials," *Chem. Mater.*, **8**, pp. 1739–1746.

[30] Sanders, R., R. Chow, and J. Masliyah (1995) "Deposition of Bitumen and Asphaltene-Stabilized Emulsions in an Impinging Jet Cell," *J. Colloid Interface Sci.*, **174**, pp. 230–245.

[31] Gu, Y. and D. Li (2000) "The Zeta Potential of Glass Surface in Contact with Aqueous Solutions," *J. Colloid Interface Sci.*, **226**, pp. 328–339.

[32] Zydney, A. (1995) "Boundary Effects on the Electrophoretic Motion of a Charged Particle in a Spherical Cavity," *J. Colloid Interface Sci.*, **169**, pp. 476–485.

[33] Ennis, J. and J. Anderson (1997) "Boundary Effects on Electrophoretic Motion of Spherical Particles for Thick Double Layers and Low Zeta Potential," *J. Colloid Interface Sci.*, **185**, pp. 497–514.

[34] Shugai, A. and S. Carnie (1999) "Electrophoretic Motion of a Spherical Particle with a Thick Double layer in Bounded Flows," *J. Colloid Interface Sci.*, **213**, pp. 298–315.

[35] Hsu, J., S. Hung, and C. Kao (2002) "Electrophoresis of a Sphere at an Arbitrary Position in a Spherical Cavity," *Langmuir*, **18**, pp. 8897–8901.

[36] ——— (2003) "Electrophoresis of a Spheroid along the Axis of a Cylindrical Pore," *Chem. Eng. Sci.*, **58**, pp. 5339–5347.

[37] Hsu, J. and C. Kao (2002) "Electrophoresis of a Finite Cylinder along the Axis of a Cylindrical Pore," *J. Phys. Chem. B*, **106**, pp. 10605–10609.

[38] Hsu, J. and M. Ku (2005) "Boundary Effect on Electrophoresis: Finite Cylinder in a Cylindrical Pore," *J. Colloid Interface Sci.*, **283**, pp. 592–600.

[39] Yariv, E. and H. Brenner (2002) "The Electrophoretic Mobility of an Eccentrically Positioned Spherical Particle in a Cylindrical Pore," *Phys. Fluids*, **14**(9), pp. 3354–3357.

[40] ——— (2003) "The Electrophoretic Mobility of a Closely Fitting Sphere in a Cylindrical Pore," *SIAM J. Appl. Math*, **64**(2), pp. 423–441.

[41] Ye, C. and D. Li (2004) "3-D Transient Electrophoretic Motion of a Spherical Particle in a T-Shaped Rectangular Microchannel," *J. Colloid Interface Sci.*, **272**, pp. 480–488.

[42] Slentz, B. E., N. A. Penner, and F. Regnier (2002) "Sampling BIAS at channel junctions in gated flow injection on chips," *Anal. Chem.*, **74**, pp. 4835–4840.

[43] Zimmerman, W. B., J. M. Rees, and T. J. Craven (2006) "Rheometry of non-Newtonian electrokinetic flow in a microchannel T-junction," *Microfluid. Nanofluid.*, **2**, pp. 481–492.

[44] Thamida, S. K. and H. Chang (2002) "Nonlinear electrokinetic ejection and entrainment due to polarization at nearly insulated wedges," *Phys. Fluids*, **14**(12), pp. 4315–4328.

[45] Wilson, H. J., L. A. Pietraszewski, and R. H. Davis (2000) "Aggregation of charged particles under electrophoresis or gravity at arbitrary Peclet numbers," *J. Colloid Interface Sci.*, **221**, pp. 87–103.

[46] Edwards, B., T. Mayer, and R. Bhiladvala (2006) "Synchronous electrorotation of nanowires in fluid," *Nano Letters*, **6**(4), pp. 626–632.

[47] Crocker, J. and D. Grier (1996) "Methods of digital video microscopy for colloidal studies," *J. Colloid Interface Sci.*, **179**, p. 198.

[48] Crocker, J. and E. Weeks (2008), "Particle Tracking using IDL," http://www.physics.emory.edu/,weeks/idl/.

[49] Yazdi, S. *Dissertation In Preparation*, Ph.D. thesis, Pennsylvania State University.

[50] Ramos, A., H. Morgan, N. G. Green, and A. Castellanos (1998) "AC electrokinetics: a review of forces in microelectrode structures," *J. Phys. D*, **31**(18), pp. 2338–2353.

[51] Tang, G. Y., D. G. Yan, C. Yang, H. Q. Gong, C. J. Chai, and Y. C. Lam (2006) "Joule heating and its effects on electroosmotic flow in microfluidic channels," *J. Phys. Conf. Ser.*, **34**, pp. 925–930.

[52] Fox, R. and A. McDonald (1998) *Introduction to Fluid Mechanics*, 5 ed., John Wiley and Sons.

[53] Venditti, R., X. Xuan, and D. Li (2006) "Experimental characterization of the temperature dependence of zeta potential and its effect on electroosmotic flow velocity in microchannels," *Microfluid. Nanofluid.*, **2**, pp. 493–499.

[54] Almutairi, Z. A., T. Glawdel, C. L. Ren, and D. A. Johnson (2009) "A Y-channel design for improving zeta potential and surface conductivity measurements using the current monitoring method," *Microfluid. Nanofluid.*, **6**, pp. 241–251.

[55] Mao, X., J. Waldeisen, and T. Huang (2007) ""Microfluidic drifting"-implementing three-dimensional hydrodynamic focusing with a single-layer planar microfluidic device," *Lab Chip*, **7**, pp. 1260–1262.

[56] Hsu, C., D. Carlo, D. Chen, C.and Irimia, and M. Toner (2008) "Microvortex for focusing, guiding and sorting of particles," *Lab Chip*, **8**, pp. 2128–2134.

[57] Dinsmore, A., A. Yodh, and P. D.J. (1996) "Entropic control of particle motion using passive surface microstructures," *Nature*, **383**, pp. 239–242.

[58] Desai, J., A. Pillarisetti, and A. Brooks (2007) "Engineering approaches to biomanipulation," *Annu. Rev. Biomed. Eng.*, **9**, pp. 35–53.

[59] Shi, J., X. Mao, D. Ahmed, A. Colletti, and T. Huang (2008) "Focusing microparticles in a microfluidic channel with standing surface acoustic waves (SSAW)," *Lab Chip*, **8**, pp. 221–223.

[60] Wong, P., C. Chen, T. Wang, and C. Ho (2004) "Electrokinetic bioprocessor for concentrating cells and molecules," *Anal. Chem.*, **76**, pp. 6908–6914.

[61] Demierre, N., T. Braschler, P. Linderholm, U. Seger, H. van Lintel, and P. Renaud (2007) "Characterization and optimization of liquid electrodes for lateral dielectrophoresis," *Lab Chip*, **7**, pp. 355–365.

[62] Chiou, P., A. Ohta, and M. Wu (2005) "Massively parallel manipulation of single cells and microparticles using optical images," *Nature*, **436**, pp. 370–372.

[63] Appleyard, D. and M. Lang (2007) "Active particle control through silicon using conventional optical trapping techniques," *Lab Chip*, **7**, pp. 1837–1840.

[64] Bazant, M. Z. and T. M. Squires (2004) "Induced-Charge Electrokinetic Phenomena: Theory and Microfluidic Applications," *Phys. Rev. Lett.*, **92**(6), pp. 066101–1 – 4.

[65] Squires, T. M. and M. Z. Bazant (2004) "Induced-charge electro-osmosis," *J. Fluid Mech.*, **509**, pp. 217–252.

[66] Ramos, A., H. Morgan, N. G. Green, and A. Castellanos (1999) "AC Electric-Field-Induced Fluid Flow in Microelectrodes," *J. Colloid Interface Sci.*, **217**(2), pp. 420–422.

[67] Ajdari, A. (2000) "Pumping liquids using asymmetric electrode arrays," *Phys. Rev. E*, **61**(1), pp. R45–R48.

[68] Levitan, J. A., S. Devasenathipathy, V. Studer, Y. Ben, T. Thorsen, T. M. Squires, and M. Z. Bazant (2005) "Experimental observation of induced-charge electro-osmosis around a metal wire in a microchannel," *Colloid. Surface. A*, **267**, pp. 122–132.

[69] Soni, G., T. M. Squires, and C. D. Meinhar (2007) "Nonlinear Phenoma in Induced Charge Electroosmosis," No. IMECE2007-41468 in 2007 ASME International Mechanical Engineering Congress and Exposition, Seattle, WA.

[70] Bazant, M. Z., K. Thornton, and A. Ajdari (2004) "Diffuse-charge dynamics in electrochemical systems," *Phys. Rev. E*, **70**, p. 021506.

[71] Storey, L., B.D. Edwards and M. Kilic, M.S.and Bazant (2008) "Steric effects on ac electro-osmosis in dilute electrolytes," *Phys. Rev. E*, **77**(3).

[72] Harnett, C., J. Templeton, K. Dunphy-Guzman, Y. Senousy, and M. Kanouff (2008) "Model based design of a microfluidic mixer driven by induced charge electroosmosis," *Lab Chip*, **8**, pp. 565–572.

[73] Morgan, H. and N. Green (2003) *AC Electrokinetics: Colloids and Nanoparticles*, Research Studies Press Ltd.

[74] Holzel, R. (1993) "Electric Field Calculations for Electrorotation Electrodes," *J. Phys. D*, **26**, pp. 2112–2116.

[75] Hughes, M., X.-B. Wang, F. Becker, P. Gascoyne, and R. Pethig (1994) "Computer-aided Analyses of Electric Fields used in Electrorotation Studies," *J. Phys. D*, (1564-1570).

[76] Dalton, C., A. Goater, J. Drysdale, and R. Pethig (2001) "Parasite Viability by Electrorotation," *Colloid. Surface. A*, (263-268).

[77] Zimmerman, V., V. Shilov, J. Lopez-Garcia, and C. Grosse (2002) "Numerical Calculation of the Electrorotation Velocity of Latex-Type Particles," *J. Phys. Chem. B*, **106**, pp. 13384–13392.

Vita

Scott M Davison

Scott M Davison was born on October 24, 1979 in Warsaw, IN. He graduated from Warsaw Community High School in June 1998. In the fall of 1998 he entered the mechanical engineering program at Purdue University. While at Purdue University, Scott spent five semesters as a Co-op engineer at Procter & Gamble in the Corporate Prototyping and Package Development division in northern Cincinnati, OH. After graduating, with highest honors, from Purdue University in May 2003 he began graduate studies at Penn State University in the department of Mechanical and Nuclear Engineering. Scott earned a Master of Science degree in May 2005. During his PhD studies, Scott has co-authored several journal and conference publications on the electrokinetic motion and control of non-spherical particles in microfluidic channels. He is an active member of the American Society of Mechanical Engineers (ASME) and the American Physical Society (APS).

Selected Publications:

- Davison, S.M. and K.V. Sharp. "Transient Simulations of the Motion of Cylindrical Particles through a 90° Corner." Microfluidics and Nanofluidics. 2008. **4**(5):409-418.
- Davison, S.M. and K.V. Sharp. "Transient Electrophoretic Motion of Cylindrical Particles in Capillaries." Nanoscale and Microscale Thermophysical Engineering. 2007. **11**:71-83.
- Davison, S.M. and K.V. Sharp. "Boundary Effects on the Electrophoretic Motion of Cylindrical Particles: Concentrically and Eccentrically Positioned Particles in a Capillary." Journal of Colloid and Interface Science. 2006. **303**(1):288-297.